Chapter 1

Introduction

1.1 Overview

A number of attempts to perform a numerical analysis of the ground motion produced in a three-dimensional continuum by a rupture propagating along a pre-existing discontinuity surface, i.e. a fault in Seismology and Earthquake Engineering, have been described in the literature in the last few years. The numerical simulation of ground motion based in the dynamic of the spontaneous rupture propagation of the fault (dynamic models) needs to solve the elastodynamic equation of motion of the continuum coupled to frictional sliding (Mode II and III in fracture mechanics) on a prescribed crack plane. In the present thesis, the attractive feature in the problem under consideration is the possibility of introducing internal cracks (mode I) that propagates under tensile stress as a consequence of the dynamic process of the shear slip propagation. In this context, the numerical simulation of the dynamic rupture process of an earthquake involving the three basic modes (Mode I, II and III) is considered. Since we accept that the rupture process of an earthquake is a fracture mechanics problem, the superposition of the three basic modes (Mode I, II and III) is sufficient to describe the most general case of the dynamic crack propagation of an earthquake. In the present formulation four aspects of the problem deserve independent consideration:

(a) Modeling of the solid continuum and seismic wave propagation.

(b) Artificial boundaries of the modeled volume to represent the (semi) infinite extent of the continuum.

(c) Definition of the stress change on the fault surface during shear rupture, or, alternatively, specification of so-called fault constitutive laws in conjunction with an initial stress state, in which case the variation of slip and velocity of rupture propagation along the fault are determined in the analysis.

(d) Definition of the constitutive relation to open tensile cracks as a consequence of the shear slipping.

The problem is resolved modeling the first item, by way of introduction to the more complex topics included in (b), (c) and (d).

The simplest assumption concerning the mechanical behaviour of the material is to admit linear elasticity, jointly with linear viscous damping. Those hypotheses appear to be sufficient to account for the response of sound rock to seismic excitation and are common to most procedures proposed in the literature. For analysis of general problems, four schemes may be mentioned as the best developed alternatives: (1) the finite-element method (FEM), (2) the boundary-element method (BEM), (3) the so-called staggered-grid Finite-Difference Method (FDM) and (4) the discrete-element method (DEM). The FEM and BEM have been applied to solve problems in various fields of science and technology. In fact, extensive use of the former may be found in the study of soil-structure interaction effects in seismic analysis, as described, for instance, by Wolf (1997) and in dynamic rupture process of earthquakes (e.g. Fukuyama and Madariaga, 1998). The FDM is widely used in seismology to the ground motion simulation and shear rupture propagation (see, for example, Madariaga, 1976, Graves 1996, Olsen et al.1997, Inoue and Miyatake 1998, Madariaga et al., 1998, Pitarka 1999). The DEM is widely employed in engineering to designate lumped mass models in a truss arrangement, as opposed to FEM (Finite Element) models that may also consist of lumped masses, but normally require to mount a full stiffness matrix for response determination. The application of the DEM to the ground motion and dynamic rupture simulation is new, it was introduced by Dalguer (2000), Dalguer et al (2001 a,b) using a 2D model. The 3D model is used for the first time in the present thesis, being one of the objective of this work, that is, introduce the DEM in 3D in the scientific community of Sismology and earthquake Engineering.

Various algorithms have been developed to implement all these techniques mentioned above, the question of which one is the best technique remains, this subject is always a debate because each method has its merits and pitfalls. But for the problem solved in the present thesis, certainly the advantage of the DEM compared to the others methods (FEM, BEM, FDM) is the facility of introducing internal tensile cracks with little computational effort and without increasing the number of degrees of freedom of the system.

The study of the dynamic rupture process is very important for the simulation of the ground motion. Several attempts to perform numerical analyses of the dynamic rupture processes of a fault have been described in the literature. The pioneering work of Kostrov (1966) simulated the spontaneous propagation of an anti-plane shear crack. Das and Aki (1977) and Andrews (1976), using the slip weakening model as a friction law of the fault, simulated spontaneous rupture propagation of an in-plane shear crack. Subsequently, the rupture process of the fault was simulated with more sophisticated models (e.g., Mikumo and Miyatake, 1978; Virieux and Madariaga, 1982; Day, 1982a,b; Cochard and Madariaga, 1994, Fukuyama and Madariaga, 1998; Madariaga et al., 1998; Inoue and Miyatake, 1998). Dynamic models are frequently used to study the physics of earthquakes, as related to the rupture process of the fault. Although few efforts were devoted to the simulation of ground motion based on dynamic models, some recent contributions should be cited. Olsen et al., (1997) simulated the rupture process and near field ground motion of the 1992 Landers (California) earthquake using a finite difference method in the frequency range. Inoue and Miyatake (1998) simulated theoretical strong ground motion generated from the rupture process on a shallow strike-slip fault using a 3D finite-difference method, Dalguer et al (2001 a,b), using a simplified 2D model, simulated the 1999 Chi-Chi earthquake and near source ground motion.
On the other hand, in the study of the seismic wave propagation in 3D elastodynamic problem with a pre-existing fault, the slip on the fault surface usually are specified as a function or it is represented by the moment-tensor source formulation that uses stress components (e.g., Frankel, 1993; Coutant et al., 1995; Olsen et al., 1995; Graves 1996; Pitarka 1999). The moment-tensor source formulation uses equivalent body forces that are appropriately added at each point corresponding to the source location. Because the motion on the fault surface is specified, these methods are called kinematic models. For the simulation of strong ground motion using these kinematic models, the 3D FDM is widely used (e.g., Frankel and Vidade, 1992; Yomigida and Etgen, 1993; Pitarka and Irikura, 1996; Pitarka et al., 1998; Graves, 1998). But the inconvenient of these models is that the slip function on the fault is specified, it means that they do not take in to consideration the physic of the rupture process, that is, the frictional level of the surface is neglected, violating the natural development of the spontaneous rupture propagation that strongly depend of the initial stress level distribution and the law constitutive relation along the fault.

In the present thesis the numerical solution is obtained solving the elastodynamic motion coupled to frictional sliding on a prescribed fault plane. With this procedure, the dynamic rupture propagation of the fault is simulated as well as the wave radiated from fault, making possible the simulation of the ground motion based in a dynamic model. The attractive feature in the problem under consideration is the possibility of introducing internal new cracks that propagates under tensile stress as a consequence of the dynamic process of the shear slip propagation. For the shear rupture propagation the simple slip-weakening model is used as a friction law on the pre-existing. And for the new tensile cracks, the fracture will occur, following the classical Griffith theory, when the critical value of tensile fracture surface energy has been reached. The firs step in the problem is the estimation of the geometry of the pre-existing fault and the dynamic parameters, such us stress drop, strength excess and critical slip. For a real earthquake, these parameters could be recovered from the results of waveform inversion, it will be explained later. In the second step a shear dynamic rupture process is simulated assuming that the shear slip take place only on the pre-existing and the tensile stress concentrations resulting from shear slip will cause the new cracks that will propagates away from the pre-existing fault. As knowledge by the author, the present work shows the first numerical simulation in 3D of the generation of tensile cracks during the shear dynamic rupture process of a pre-existing fault. Tentative simulations in 2D were presented by Yamashita (2000) using a dynamic model and Vermilye and Scholz (1998) and Reches and Lockner (1994) using a quasi-static analysis.

The study of wave propagation and strong-ground motion simulation based in dynamic rupture process is more realistic and contributes to a better understanding of the physics of earthquakes and the effects of the dynamic process on the ground motion. In the recent earthquakes of Kobe 1995, Kocaeli 1999, Chi-chi 1999, that caused big damage in urban centers, was observed complicated damage pattern and near source ground motion distribution that could be due to the characteristics of the dynamic rupture process of the fault. In the recent work of Dalguer et al (2001a,b), in which they used a simplified 2D model to simulate the 1999 Chi-Chi earthquake, was showed that the ground motion near the fault of the Chi-Chi earthquake could been strongly affected mainly by dynamic source parameters. In this context, the study of the dynamic rupture process and its effect on the ground motion are the fundamental importance for the assesment of seismic hazard and disaster prevention purpose.

1.2 Objective of the thesis

-Develop a dynamic model to simulate the rupture process of the fault and near source ground motion.

-Investigate numerically the formation of new cracks during an earthquake.

-Introduce the 3D DEM in the scientific community of Sismology and earthquake Engineering

-Applied the model for the simulation of real earthquakes in order to try to explain some of the characteristics of the fault rupture, crack formation, near source ground motion and damage pattern caused by real earthquakes.

1.3 Organization of the thesis

In chapet 1, an over view of the problem of dynamic rupture and ground motion simulation in seismology, the general characteristics of the formulation proposed and the objective of the thesis are presented. In chapter 2, the application and formulation of the Discrete Element Method (DEM), numerical technique used in the thesis, is described. In chapter 3, the definition of the problem is set, that is, the boundary conditions along the pre-existing fault as well as the artifitial boundaries needed for the discretization of the (semi) infinite of the continuum are specified. The constitutive relation that governs the shear dynamic rupture and tensile cracks propagation are also formulated. In chapter 4, the validity of the DEM in 2D and 3D for the simulation of shear dynamic rupture process is presented, for this purpose, theoretical problems of shear cracks propagation are solved and compared with numerical results presented in the specialized literature. In Chapter 5, the methodology used for the estimation of the dynamic parameters needed for the 3D dynamic shear rupture propagation of a real earthquake is formulated. These parameters are the stress drop, strength excess and critical slip distribution along the fault. The formulation is applied to the 2000 Tottori earthquake. The results, the stress changes distribution on the fault, are associated to the aftershock and foreshock distribution of the Tottori earthquake. In chapter 6 and 7, theoretical problems of shear dynamic rupture and tensile cracks propagation for the 2D and 3D model respectively are simulated. For the 2D problems, the analysis is concentrated in the investigation of the effects of the dynamic parameters (strength excess and critical slip) on the near source ground motion of dipping faults that breaks the free-surface. For the 3D problems, the effects of the tensile cracks generation on the near source ground motion and rupture process is analyzed. In Chapter 8, the formulation proposed is applied to the 2000 Tottori earthquake. The ground motion simulation as well as the cracks originated during the shear slipping are analyzed and compared with observations. Finally, in Chapter 9, the main conclusions of the current study are summarized.

Chapter 2

The Discrete Element Method (DEM)

2.1 Introduction

The DEM is widely employed in engineering to designate lumped mass models in a truss arrangement, as opposed to FEM (Finite Element) models that may also consist of lumped masses, but normally require to mount a full stiffness matrix for response determination. The term has also been used for models of solids consisting of assemblies of discrete elements, such as spheres in elastic contact, employed in the analysis of perforation or penetration of concrete or rock. It should be noted that the designation Lattice Models, common in Physics, may be more adequate, although it omits reference to a fundamental property of the approach, which is the lumped-mass representation. In the present DEM formulation, orthotropic solids are represented by a three dimensional periodic truss-like structure using cubic elements as shown in Figure 2.1. This model is based on earlier developments in aeronautical engineering in which, for purposes of structural analysis it is often necessary to establish the equivalence between truss-like structural systems and a continuous medium. Nayfeh and Hefsy (1978) generated equivalent continuum elastic properties for the three-dimensional truss-like structures using an arrangement of two kinds of models, the octaetruss and cubic elements. On the other hand, Hayashi (1982), using the same formulation, developed the study in opposite direction, that is, generate the equivalent three-dimensional truss-like structures for a real continuum using cubic elements. This method leads to results that converge to solutions for a linear elastic continuum in dynamic problems. Riera and Rocha (1991) used the approach in fracture studies, Doz and Riera (1995) employed the method to model the stick-and-slip motion along friction surfaces, Dalguer et al. (1999) evaluated the foreshock and periodicity of earthquakes and Dalguer et al (2001 a,b), using a simplified 2D approach, modeled a fault dynamic rupture using the slip weakening friction model to simulate the rupture process of the 1999 Chi-Chi (Taiwan) earthquake. A more extensive application of the DEM in 2D, for seismology purpose, could be found in Dalguer (2000). Also Mora and Place (1994), Shi et al. (1998), Morgan (1999), Morgan and Boettcher (1999) and Rimal (1992) used a 2D lattice model, also called Distinct Element Method similar to the DEM, to simulate dynamic rupture of earthquake faulting.

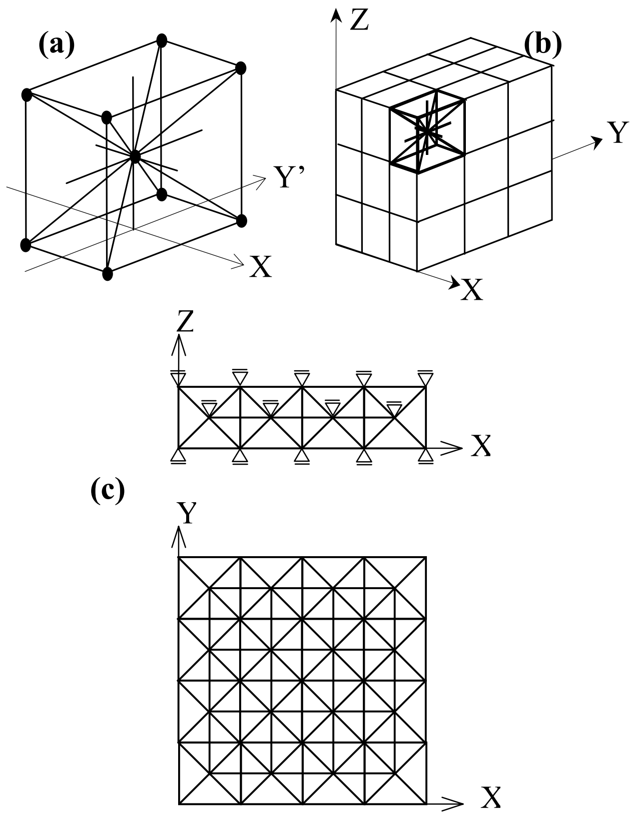

Figure 2.1. Numerical model used for the dynamic simulation (DEM): (a) Basic cubic module, (b) generation of prismatic body for 3D model and (c) representation of a plane strain state (no z displacements) for 2D model.

2.2 Formulation of the present DEM

The Discrete Element Method (DEM) models any orthotropic elastic solid. It is constructed by a three dimensional periodic truss-like structures using cubic elements as shown in Figure 2.1. Nayfeh and Hefsy (1978) established the equivalence requirements between the cubic arrangement shown in Figure 2.1 and an orthotropic elastic medium. In case of an isotropic elastic material, the cross-sectional axial stiffness of the longitudinal bars in the equivalent discrete model is given by (Riera and Rocha,1991):

$$AE_n = \phi E \Delta x^2 \quad \text{(bar length = } \Delta x\text{)} \tag{2.1}$$

while for the diagonal bars

$$AE_d = 2\delta\phi E \frac{\Delta x^2}{\sqrt{3}} \quad \text{(bar length = } \sqrt{3}\frac{\Delta x}{2}\text{)} \tag{2.2}$$

where for approximately isotropic solids, i.e. solids with equal stiffness in the three orthogonal directions, ϕ=(9+8δ)/(18+24δ), δ=9ν/(4-8ν), ν is the Poisson's ratio and E is the Young's modules of the material. For other situations, for example layered (orthotropic) rocks, the above constants take on other values (See Nayfeh and Hefsy, 1978). It should be stressed that no lattice or truss-like model can exactly represent a locally isotropic continuum, and for that matter it can also be argued that no locally isotropic continuum exists. Isotropy in solids is a bulk property that reflects the random distribution of the orientation of constituent elements. Details of the calculation of the equivalent cross-sectional axial stiffness of the normal (AE_n) and diagonal (AE_d) elements for a cubic lattice array given by equation (2.1) and (2.2) respectively are presented in Appendix .

In the discrete dynamic model, masses are concentrated at nodal points. As shown in Figure 2.1a, solids are represented as an array of normal and diagonal bars linking lumped nodal masses.

The uniaxial elastic forces, Fe, acting along the bars, are computed using the cross-sectional axial stiffness given by Equation (2.1) or (2.2)

$$Fe_j = AE_j \varepsilon_j \tag{2.3}$$

where ε is the axial deformation of the bar j (j=n or d, normal or diagonal bar respectively). The representation of the elastic forces in the form given by Equation (2.3) is very convenient to simulate tensile cracks, as will later be explained in chapter 3, item 3.5. The dynamic analysis is performed using explicit numerical integration in the time domain. At each step of integration a nodal equilibrium represented by equation (2.4) is solved by the central finite differences scheme.

$$m\ddot{u}_i + c\dot{u}_i = f_i \tag{2.4}$$

where m denotes the nodal mass, c the damping constant, $\dot{u}_i$, $\ddot{u}_i$ a component, velocity and acceleration respectively of the nodal coordinates vector, and f_i a component of the resultant forces at one nodal point including elastic, external and frictional forces in direction i of the motion. In the current model, for the simulation of the dynamic rupture process of a pre-existing fault, only the nodal points that coincide with the pre-existing fault, once it breaks, are under frictional force governed by any predefined friction law. The damping constant c was assumed to be proportional to the rigidity (k) of the bars of every cubic element, that is $c= d_f k,$ where d_f was assumed to be 0.005. It is approximately a critical damping ratio (ξ) less or equal to 0.045.

Equation (2.4) represents the equation of motion of a discrete point in the continuum. When this point is on the pre-existing fault, the fault parallel component of the resultant force (f_i) is governed by the constitutive relation on the fault.

Chapter 3

Definition of the Problem

3.1 Introduction

Dynamic simulation of rupture processes during earthquakes is usually performed under the assumption that only shear slip (Mode II and/or III) occurs (e.g., Andrews, 1976; Day, 1982; Olsen et al., 1997; Fukuyama and Madariaga, 1998; Harris and Day, 1999). This is widely accepted in the study of earthquakes because this phenomenon may be considered to be a dynamically running shear crack (e.g., Scholz, 1990). However, it is well known that the rupture process of an earthquake involves the superposition of the three basic modes (Mode I, II and III) recognized in dynamic fracture mechanics (e.g., Atkinson, 1987). In fact, laboratory observations suggest that a large number of tensile (mode I) microcracks are generated during shear slipping (e.g., Cox and Scholz, 1988; Moore and Lockner, 1995; Anders and Wiltschko, 1994; Petit and Barquins, 1988). Numerical and field investigation of brittle faults carried out by Vermilye and Scholz (1998) show that the tensile microcracks zone occurs within a volume of rock surrounding the fault tip. This zone may form before, during, or after growth of the shear plane. These observations of experiment inducing shear fractures (e.g., Cox and Scholz, 1988) as well as field investigations (e.g., Vermilye and Scholz, 1998) also suggest that unlike tensile fractures, low-pressure shear fracture does not grow by simple propagation within their own plane. Instead, they propagate by a complex breakdown process involving the interaction and coalescence of mode I microfractures. This idea come since Scholz, (1968) and Lajtai, (1971), in which they conclude that the shear cracks develop as a plane of shear failure only after a long history of tensile microfracturing. Steps include the formation of individual tensile microcracks, propagation and merge of these cracks and finally larger scale shear failure. It suggests that a shear rupture will propagate only along a weakness plane such as a preexisting fault (Scholz, 1990)

In this context, considering the laboratory and field observations mentioned above, the numerical simulation of a dynamic rupture process of an earthquake involving the three basic modes (Mode I, II and III), imply the assumption of a pre-existing fault for developing of the shear crack, and the tensile stress concentrations resulting from slip on the pre-existing fault will cause the mode I cracks that will propagates away from the pre-existing fault. A few numerical simulations were developed introducing the tensile crack during the dynamic shear rupture, one example is the work of Yamashita (2000), this author investigated numerically the generation of tensile microcracks by dynamic shear rupture using a 2D Finite Difference formulation. In this model the microcracks are always separated by a fixed distance and are locally parallel, i.e., the simulation consist of a concentration of a swarm of cracks, these assumptions do not allow the linking between the cracks in order to form a new surface of crack. Vermilye and Scholz (1998) and Reches and Lockner (1994) studied the generation of microcracks based in a quasi-static analysis, they inferred only the orientation of the microcracks from the analysis of quasi-static tensile stresses.

In the present thesis we employ a 3D numerical model to simulate the shear dynamic rupture process of an earthquake; and additionally, the possibility to simulate the propagation of new tensile cracks as a consequence of a spontaneous shear dynamic rupture process of a pre-existing fault is also formulated. For the shear rupture propagation the simple slip weakening model is used as a friction law on the pre-existing fault, while for the new tensile cracks, the fracture will occur, following the classical Linear Elastic Fracture Mechanics (LEFM) theory (Griffith, 1920), when the critical value of tensile fracture surface energy is reached

To perform the numerical model proposed above, that is, for the analysis of the motion produced in a three-dimensional continuum by a rupture propagating along a pre-existing fault and the generation of new cracks, four aspects of the problem deserve take in consideration:

(a) Modeling of the solid continuum and seismic wave radiated from the fault.

(b) Artificial boundaries of the modeled volume to represent the (semi) infinite extent of the continuum.

(c) Modeling of the dynamic rupture propagation on the fault. This imply the definition of the friction law that govern the shear slipping and the boundary conditions on the pre-existing fault.

(d) Definition of the constitutive relation to open tensile cracks as a consequence of the shear slipping.

The problem mainly consist in the modeling of the first item by way of introduction to the more complex topics included in (b), (c) and (d). A schematic representation of the problem is shown in fig.3.1, a layer with a pre-existing fault is considered. To facilitate a numerical solution the area is limited by the broken line that become artifitial boundaries. This boundary around the model should be defined in order to simulate the (semi) infinite extent of the continuum. The Wave propagation occurs in a simulated earthquake due to a spontaneous slippage along the pre-existing fault surface, which should be nonreflecting in the artificial boundary. The pre-existing fault inside the surface S includes two adjacent surfaces pressed against each other. These surfaces are normal to the layer middle plane S.

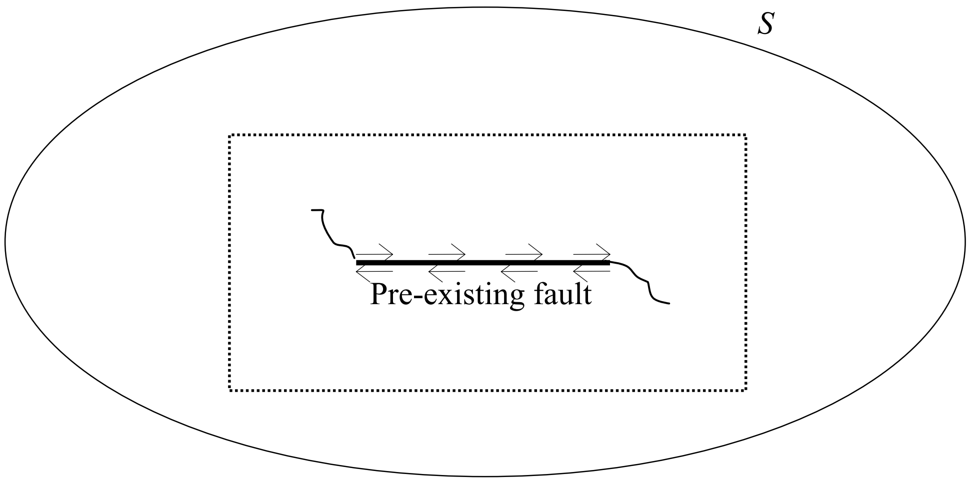

Figure 3.1. Schematic representation of the problem: Finite elastic layer with surface *S* and a pre-existing fault. The area limited by the broken line represents the region to be modeled. Furthermore. The arrows show the orientation of shear slip along the pre-existing fault. And the irregular lines are the tensile cracks originated by the shear slipping of the pre-existing fault.

The simplest assumption concerning the mechanical behaviour of the material is to admit linear elasticity, jointly with linear viscous damping. Those hypotheses appear to be sufficient to account for the response of sound rock to seismic excitation and are common to most procedures proposed in the literature.

3.2 Local Absorbing Boundary used in the DEM

During the formulation of the model an important problem is confronted, that is, how the artificial boundary conditions around the model should be defined in order to simulate the infinite extent of the continuous medium and allow energy to propagate only from the interior to the exterior region. In other words, the wave propagation process originated at a point on the fault surface due to the dynamic rupture has to be non-reflected at the artificial boundary. Several schemes have been developed to formulate highly absorbing local approximations to the perfectly absorbing boundary. In this work the one-dimensional wave propagation solution using the semi-infinite prismatic rod as a simplest case is adopted (Wolf, 1988), due to the simplicity of this formulation and to the characteristics of the discrete element method.

The one-dimensional wave propagation, which by definition is local in space, can be used to develop the basis for frequency-independent transmitting boundaries, which are local in time. The semi-infinite prismatic rod is the simplest case. Radial effects are disregarded.

The prismatic rod with area A, modulo of elasticity E, and mass density ρ extending to infinity is shown in fig. 3.2a. N represents the axial force and u the axial displacement. Formulating equilibrium of the infinitesimal element (fig. 3.2b)

$$N_{,x}dx - \rho A dx \ddot{u} = 0 \tag{3.1}$$

and substituting the force-displacement relationship

$$N = EAu_{,x} \tag{3.2}$$

leads to the equation of motion

$$u_{,xx} - \ddot{u}/c_l^2 = 0 \tag{3.3}$$

where c_l denotes the rod velocity

$$c_l = (E/\rho)^{1/2} \tag{3.4}$$

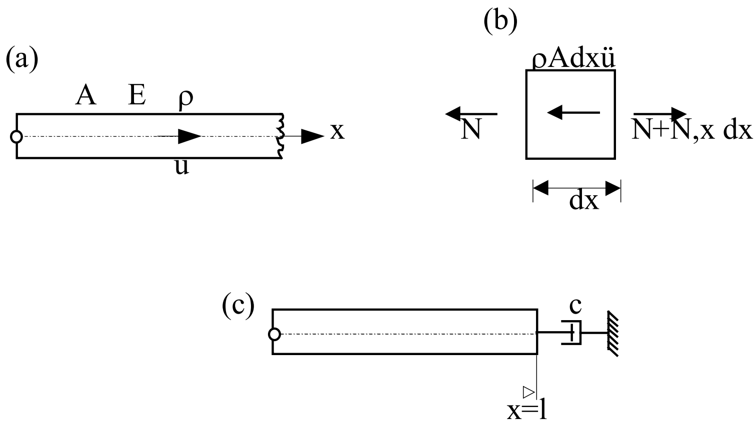

Figure 3.2 (a) Semi-infinite prismatic rod; (b) Equilibrium of infinitesimal element; (c) Viscous damper modeling truncated rod

Solving the Equation (3.3), and considering the property of a transmitting boundary located on the artificial boundary at $x=l$ (fig. 3.2c), the wave encounters the artificial boundary, this wave must pass through it without any modification so it can continue propagating towards $x=+\infty$. Considering this fact, the physical interpretation of the boundary condition at x=l becomes apparent by (Wolf, 1988)

$$EAu_{,x} + EAu/c_l = 0 \tag{3.5a}$$

or, after substituting Equation (3.2) and (3.4)

$$N + cu = 0 \tag{3.5b}$$

results with

$$c = A\rho c_l \tag{3.6}$$

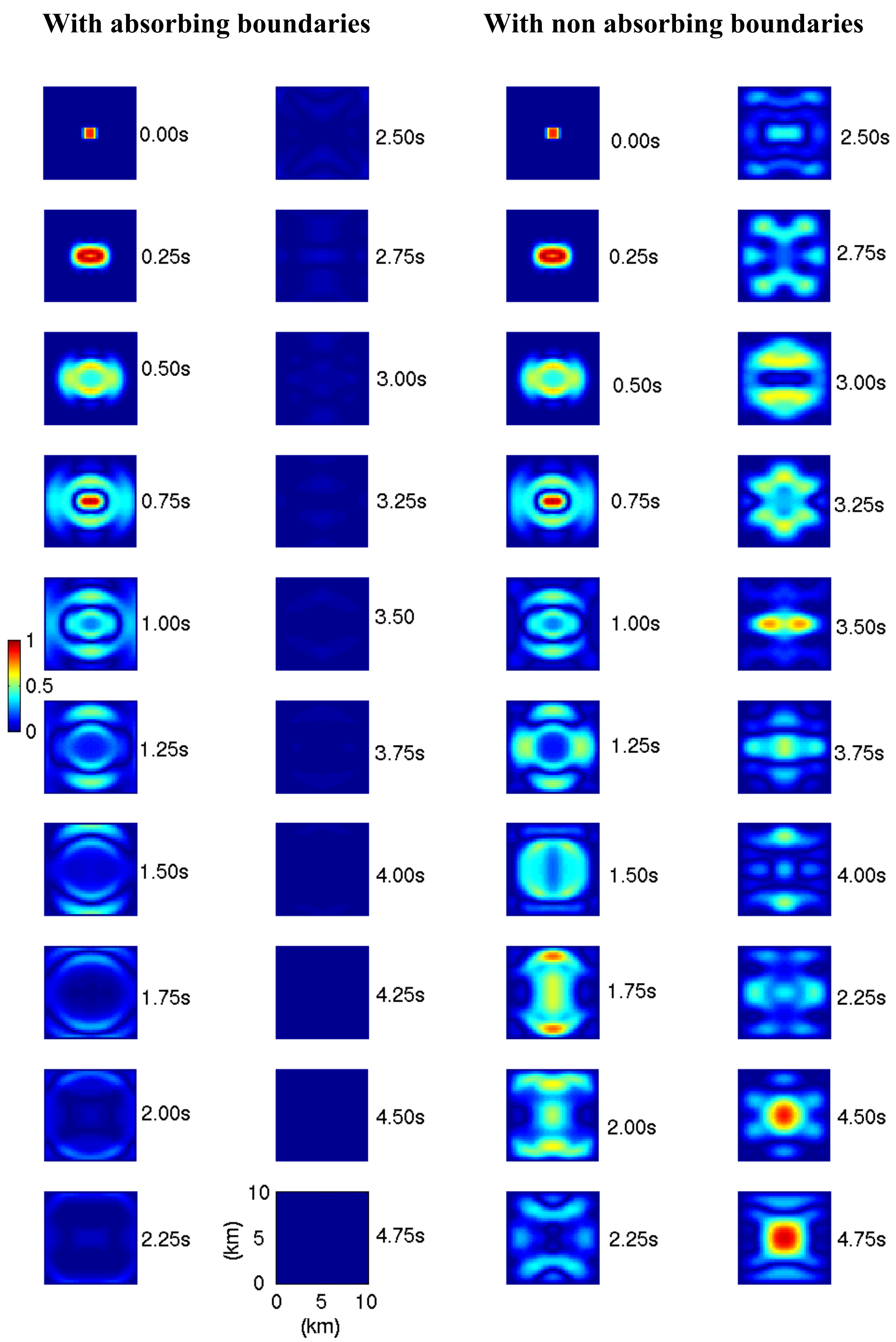

Figure 3.3. Comparison of wave progation for a model with absorbing and non-absorbing boundaries

Equation (3.5b) expresses equilibrium at the artificial boundary, involving the normal force and the force of a viscous damper with a coefficient *c*, which replace the part of the rod up to the infinity (fig. 3.2c). *c* is also called the impedance. Because *c* is independent of frequency, this transmitting boundary can be used directly for an analysis in the time domain. Therefore, Equation (3.5b) is used stead of Equation (2.4) for the borders of the computational domain.

In order to show the efficiency of the formulation given by Equation (3.5b), a numerical example is developed. In Figure 3.3 is shown the P and S wave propagation in a semi-infinite space with absorbing and no-absorbing boundary conditions. In the numerical experiment a unit rectangular horizontal load is applied on the middle of the space of 10km x 10km. A grid size of 0.25km and a step time Δt=0.05 seconds are used. The continuum is characterized by a set of P wave velocity (6.1 km/sec), S wave velocity (3.5 km/sec), density 2700 kg/m^3, corresponding to Young's modulus 8.37 x 10^{10} N/m^2, Shear modulus 3.35 x 10^{10} N/m^2 and Poisson's ratio 0.25. In Figure 3.3 we can observe the efficiency of the absorbing boundaries for the P and S waves. While for the model without absorbing boundaries, the waves are reflected from the borders of the model.

3.3 Boundary Conditions along the Pre-existing fault

As shown in fig.3.1, a layer with a pre-existing fault is considered. The pre-existing fault inside the surface S includes two adjacent surfaces pressed against each other. Let set that the fault is on the *x-y* plane in which the crack starts to propagate at the origin of coordinates *x-y-z*. The z axis is normal to the fault plane. The displacements components that satisfy the equation of motion given by Equation. (2.4) in the direction of *x, y* and *z* are *u(x,y,z,t), v(x,y,z,t)* and *w(x,y,z,t)* respectively. The rupture zone propagates along the pre-existing fault. Let set the rupture zone $\Gamma(t)$ at time t inside the pre-existing fault as shown in Figure 3.4

The constitution of the interface material along the fault must be essentially stable (i.e. no marked penetration or normal plastic deformation of the interface). In this context the displacement component normal to the fault plane, *w(x,y,0,t)*, is continuous inside and outside the rupture zone. Therefore it is assumed that

$$w(x, y, +0, t) = w(x, y, -0, t) \tag{3.7}$$

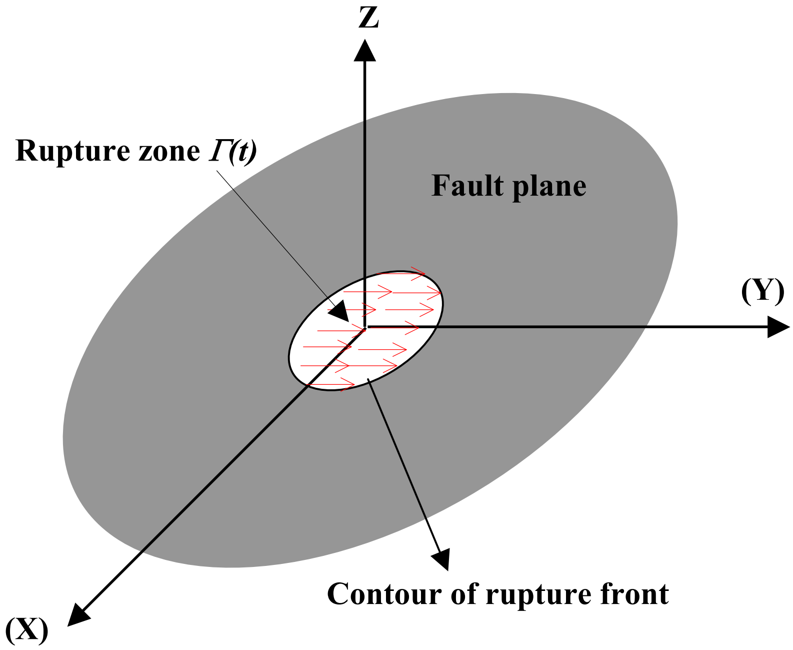

Figure 3.4. Scheme of the rupture process at time *t* along the pre-existing fault

Inside the rupture zone *Γ(t)* (*z*=0) the displacements *u(x,y,0,t)* and *v(x,y,0,t)* are discontinuous

$$D_x(x,y,t) = u(x,y,+0,t) - u(x,y,-0,t) \quad \text{for x,y} \in \Gamma(\text{t}) \tag{3.8a}$$

$$D_y(x,y,t) = v(x,y,+0,t) - v(x,y,-0,t) \quad \text{for x,y} \in \Gamma(\text{t}) \tag{3.8b}$$

and out of the rupture zone they are continuous

$$u(x,y,+0,t) = u(x,y,-0,t) \qquad \text{for x,y} \notin \Gamma(\text{t}) \tag{3.9a}$$

$$v(x,y,+0,t) = v(x,y,-0,t) \qquad \text{for x,y} \notin \Gamma(\text{t}) \tag{3.9b}$$

therefore

$$D_x(x,y,t) = D_y(x,y,t) = 0 \text{ ..... for x,y} \notin \Gamma(\text{t}) \tag{3.9c}$$

where $D_x(x,y,t)$ and $D_y(x,y,t)$ are the slip along the fault in x and y component respectively. The total slip could be given by

$$D(x,y,t) = \sqrt{D_x(x,y,t)^2 + D_y(x,y,t)^2} \qquad (3.10)$$

The shear f_t and normal f_n forces are continuous:

$$f_t = f_t(x,y,+0,t) = f_t(x,y,-0,t) \qquad (3.11a)$$

$$f_n(x,y,+0,t) = f_n(x,y,-0,t) \qquad (3.11b)$$

Inside the rupture zone $\Gamma(t)$ the shear forces f_t, follow a low friction

$$f_t = f_u - T(D,\dot{D}) \qquad \text{para x,y} \in \Gamma(\text{t}) \qquad (3.12)$$

Where f_u is the critical shear force before happen the rupture of the fault and $T(D, \dot{D})$ is the friction force on the fault that could be dependent or not of the slipping D and/or the sip velocity $\dot{D}$.

3.4 Friction Law Along the Pre-existing Shear Fault

Laboratory experiments on rock (e.g. Dieterich, 1979; Ohnaka et al., 1987, Ruina, 1983) lead to slip- and/or rate-dependent friction models. In this study we adopt the simple slip-weakening friction model in the form given by Andrews (1976). This friction law that was first proposed by Ida (1972) is extensively used for dynamic simulation of fault rupture processes (e.g., Andrews, 1976; Day, 1982b; Olsen et al., 1997; Fukuyama and Madariaga, 1998; Harris and Day, 1999). The slip-weakening friction model is schematically represented in Figure 3.5. The shear force on the fault calculated from the resultant force, f_i, of Equation (2.4), could be expressed by the shear stress, τ. The following is the relation between the shear stress, τ,. and the slip of the fault, D.

$$\begin{aligned} &\tau < \tau_u && \text{for} \quad D = 0 \\ \tau = &\begin{cases} -\dfrac{\tau_u - \tau_f}{D_c} D + \tau_u & \text{for} \quad 0 < D < D_c \\ \tau_f & \text{for} \quad D \geq D_c \end{cases} \end{aligned} \tag{3.13}$$

where τ_u is the critical stress or the upper yield point, τ_f is the final stress or the residual stress which is considered as the dynamic friction stress level, and D_c is the slip required for stress to drop to its dynamic friction level. We assume that there is not back slip on the fault, which means that the slip velocity is always greater or equal to zero.

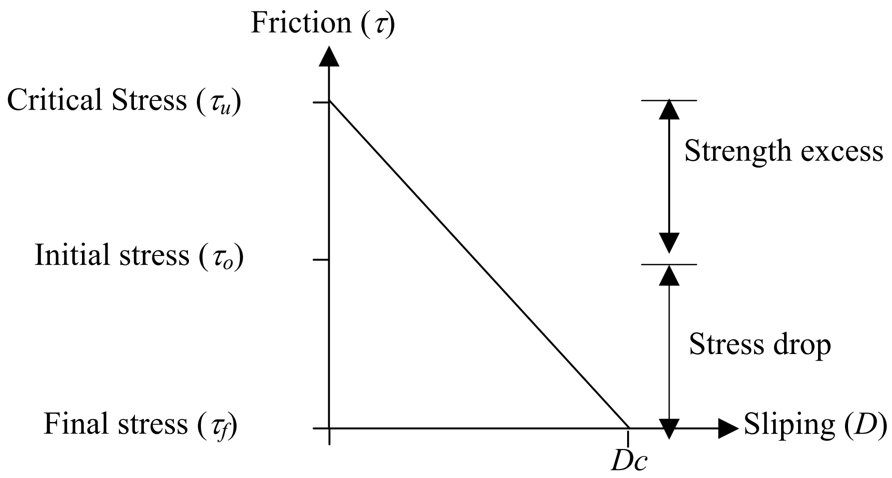

Figure 3.5. The slip-weakening friction model.

Initially the stress distribution along the fault is in the initial stress level (τ_o), the rupture is initiated artificially by imposing stress drop in a limited space, this step leads the initial stresses along the fault increase monotonically without any relative slipping along the fault until, eventually, the interface shear stress, τ, at a point exceeds the local shear strength (critical stress level τ_u) and slip at a node occurs being governed by the slip weakening model shown in Figure 3.5 and represented by Equation (3.13).

3.5 Constitutive Relation for the Tensile Crack Propagation

It was observed in rock (e.g., Atkinson, 1987) that the behavior of uniaxial tensile stress-strain shows strain softening after a peak stress has been reached. Therefore, a constitutive model for a pure mode I is the stress versus crack-opening-displacement as shown in Fig. 3.6a, it could be obtained from displacement-controlled direct tension test (Atkinson, 1987). A material behaving in this manner would show a gradual damaged zone development, as schematically shown in Fig. 3.6b. This would be related to the critical tensile fracture energy, G_{Ic}, of linear elastic fracture mechanics (LEFM) that has its roots in Griffith's energy balance concept. Therefore, extension of a fracture will occur once the G_{Ic} has been reached or exceeded. From Fig. 3.6a, the critical fracture energy, G_{Ic}, may be given as follow:

$$G_{Ic} = \int_0^{U_c} \sigma(U)dU \tag{3.14}$$

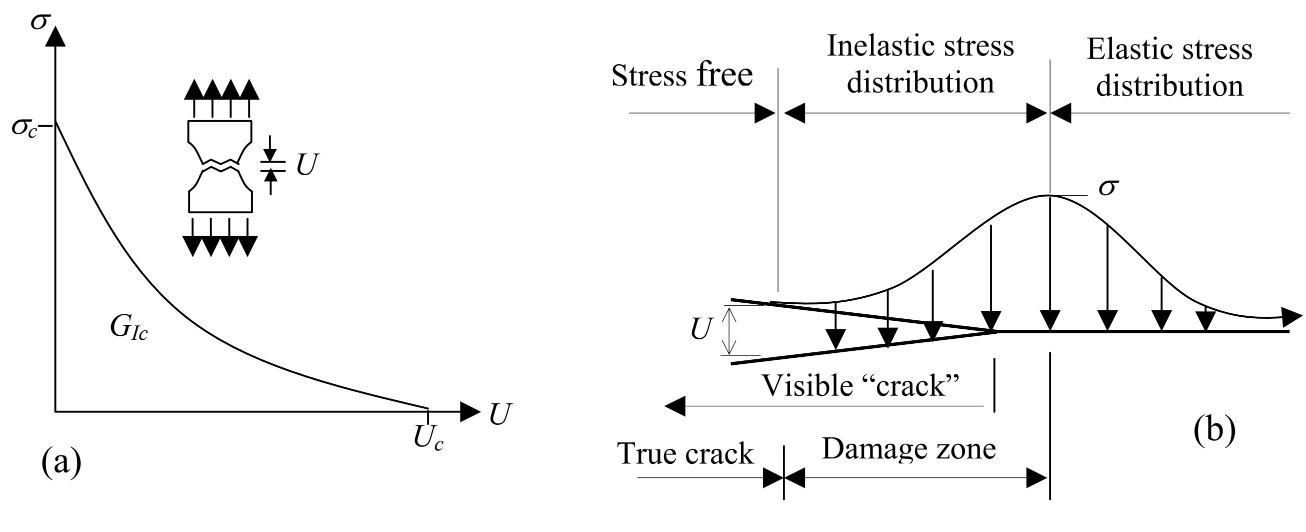

Figure 3.6. (a) Stress versus crack opening displacement relation which can be obtained from a displacement-controlled, direct tension test (Atkinson, 1987). (b) A schematic view of the hypothesized process zone (Atkinson, 1987).

Use of DEM models, that is, the representation of elastic solids using discrete masses interconnected by unidimensional elements, is very convenient to simulate tensile cracking with the features shown in Fig. 3.6. In this context, the constitutive relation for the tensile stress-strain adopted for each bar element of the DEM is shown in the Figure 3.7a. The loading and unloading path is shown in Fig. 3.7b. A similar model was successfully used by Riera and Rocha (1991) to solve dynamic tensile cracks propagation in 2D problems. Since the stress and strain are in the one-dimensional formulation, the critical tensile stress σ_c could be derived from Equation (2.3) or directly from Figure 3.7a

$$\sigma_c = E\varepsilon_p \tag{3.15}$$

where ε_p is the maximum elastic strain.

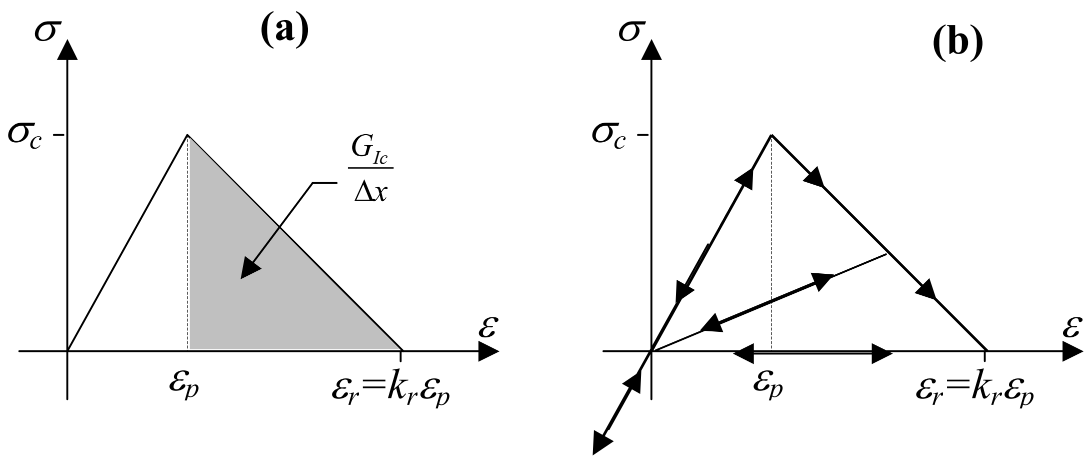

Figure 3.7. (a) Constitutive relation for the tensile crack generation used in the DEM, (b) loading and unloading paths.

Considering Equation (3.14) and Fig. 3.6, the critical fracture energy, G_{Ic}, for the DEM can be obtained as the area of the inelastic zone of the stress-strain relation shown in Fig. 3.7a; thus, using Equation (3.15) we get

$$G_{Ic} = \frac{1}{2} E \varepsilon_p^2 \Delta x (k_r - 1) \tag{3.16}$$

where Δx is the length of the element bar (grid size of the DEM.) and $k_r = \dfrac{\varepsilon_r}{\varepsilon_p}$, shown in Fig. 3.7a, is the coefficient that defines the strain softening after a peak stress has been reached, until crack totally opens. The critical tensile stress σ_c may be calculated by the modified form of the classical Griffith equation (Griffith, 1920)

$$\sigma_c \cong \sqrt{\frac{EG_{Ic}}{\pi c}} \tag{3.17}$$

where $2c$ is the pre-existing crack length. For a crack in a linear elastic solid, G_{Ic} can be expressed in terms of the critical stress intensity factor K_{Ic} in mode I. Using Griffith's energy balance concept, it follows that:

$$G_{Ic} = K_{Ic}^2(1-\upsilon^2)/E \tag{3.18}$$

where ν is the Poisson's coefficient. From Equations (3.17) and (3.18), the critical stress intensity factor K_{Ic} may be expressed in the form:

$$K_{Ic} = \chi\sigma_c\sqrt{L} \tag{3.19}$$

For the problem under consideration, L is the length of the pre-existing fault and χ is a non dimensional factor that depends on the problem geometry and the grid size of the DEM. From Equations (3.15), (3.18) and (3.19), it may be easily verified that

$$\varepsilon_p = \frac{1}{\chi}\sqrt{\frac{G_c}{(1-\upsilon^2)LE}} \tag{3.20}$$

The non dimensional factor, χ, can be estimated, from the combination of Equations (3.16) and (3.20), as:

$$\chi = \sqrt{\frac{(k_r-1)\Delta x}{2(1-\nu^2)L}} \qquad k_r > 1 \tag{3.21}$$

For the tensile crack propagation formulation given above, two parameters need to be previously defined from a set of alternatives, they may be the critical tensile stress intensity factor, K_{Ic}, or the critical tensile fracture energy, G_{Ic}, and the k_r coefficient.

Chapter 4

Validity of the Model

The numerical solution is obtained for the near-field elastodynamic motion coupled to frictional sliding on pre-existing fault. In order to validate the coupled problem, the model is validated for the dynamic rupture process of a fault for the 2D and 3D problem simulating theoretical crack problems.

4.1 Dynamic Rupture Propagation in a 2D Model

Dalguer (2000) and Dalguer et al (2001b) presented the validity of the 2D model to simulate dynamic rupture propagation. In this section, the problem used by these authors to verify the adequacy of the DEM is reproduced as follow:

The spontaneous inplane rupture process with the slip weakening law employed by Andrews (1976) is analyzed. In this problem, plane strain is assumed. The crack plane is the *x-y* plane, in which the crack propagates bilaterally in the x direction and extends indefinitely in the y direction, as shown in Figure 4.1. The medium is thus an infinite, homogeneous, isotropic, and linearly elastic crack plane. When the crack propagates, it will not stop.

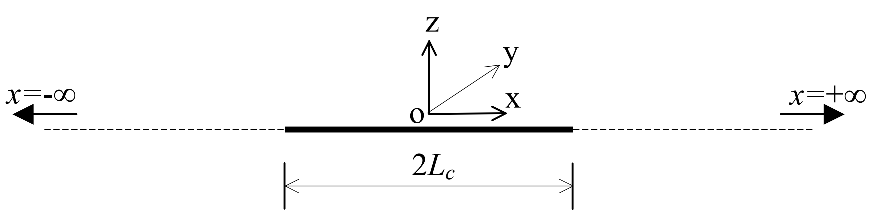

Figure 4.1 Theoretical fault, the rupture starts at the center and propagate bilaterally along the x axis and extends indefinitely in the y direction.

For the numerical computations, the parameters are normalized as follow (Andrews, 1976): Shear stress along the crack plane $\tau'=\tau/\Delta\tau$; x-axis parallel to the crack plane $x'=x/L_c$, Time $t'=t\beta/L_c$, Slip: $u'=u\mu/L_c\Delta\tau$, Slip velocity: $v'=v\mu/\beta\Delta\tau$, where β is the S wave velocity, μ is the shear rigidity, $\Delta\tau$ is the stress drop, L_c is the critical half-length (Fig. 4.1) of a Griffith crack in plane strain derived by Andrews (1976),

$$L_c = \frac{8\mu(\lambda+\mu)G}{\pi(\lambda+2\mu)(\tau_o-\tau_f)^2} \tag{4.1}$$

where λ and μ are the Lamé constants and G is the effective fracture surface energy given by:

$$G = \frac{1}{4}(\tau_u-\tau_f)D_c \tag{4.2}$$

It is assume that that Poisson's coefficient is 0.25, so $\alpha/\beta=\sqrt{3}$, where α is the P wave velocity. These non-dimensional quantities are equivalent to assuming that μ=1, $\Delta\tau$=1, β=1, $\alpha=\sqrt{3}$, L_c=1, density ρ=1. The calculations were performed with a grid size Δx=0.1L_c (length of the side of one cubic element) and $(\tau_u-\tau_o)/\Delta\sigma$ =0.8. Using equations (4.1) and (4.2), D_c=1.31 is calculated.

The near-field elastodynamic problem coupled to frictional sliding on a prescribed crack plane is solved using the 2D DEM. Initially the stress distribution along the fault is in the initial stress level (τ_o) , the rupture is initiated artificially by imposing a stress drop to propagates at least as fast as 0.5β, which leads to initial stresses along the fault that increase monotonically without any relative slipping along the fault. Eventually, the interface shear stress (τ) at a point exceeds the local shear strength (critical stress level τ_u) and slip at a node occurs, governed by the slip weakening model shown in Figure 3.5. Considering that the seismic radiation depends only on the stress change (stress drop) during the earthquake, and not on the total stress, we assume that the initial stress (τ_o) along the fault is at its zero level. Therefore, the necessary parameters required to simulate the rupture process governed by the slip weakening friction model are the strength excess, stress drop and critical slip.

Figures 4.2 to 4.7 shows the results of our numerical simulation for a theoretical spontaneous inplane rupture problem and compared with the results obtained by Andrews (1976).

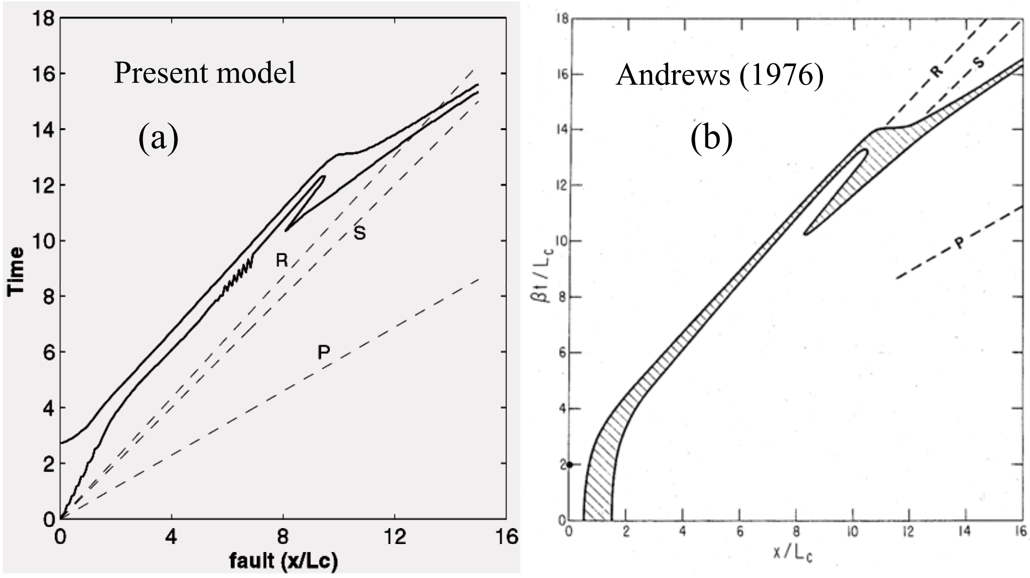

Figure 4.2 Space-time of rupture propagation of the spontaneous inplane rupture problem presented by Andrews (1976). Region between the two solid lines is the rupture front, where slip velocity is nonzero and stress drop is incomplete. Dashed line labeled P, S and R represents the wave front of the compressional, shear and Rayleigh waves respectively as a reference (Rayleigh wave velocity=0.9194β). (a) Present model; (b) Andrews (1976)

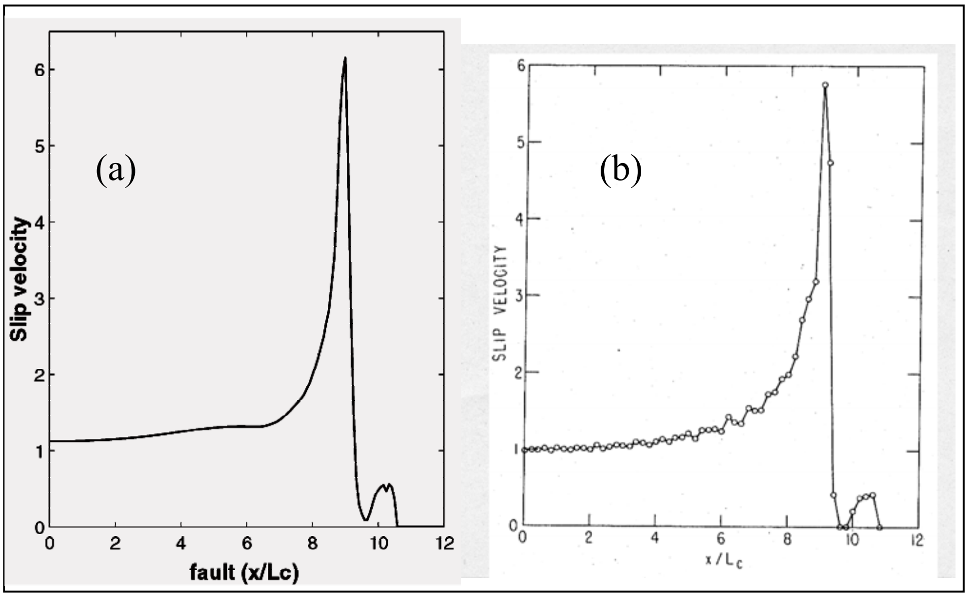

Figure 4.3. Dimensionless slip velocity, $v' = v\mu/\beta\Delta\tau$, as a function of position on the crack at the dimensionless time $\beta t/L_c = 8.07$. (a) Present model; (b) Andrews (1976).

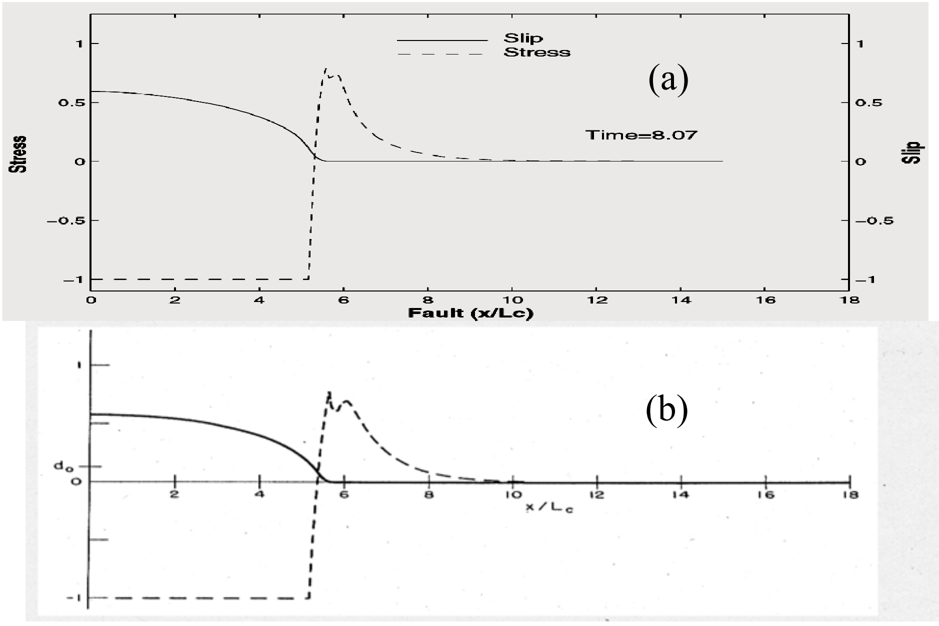

Figure 4.4. Shear stress and slip as a function of position on the crack plane at dimensionless time $\beta t/L_c$ = 8.07. Heavier solid curve is dimensionless slip function divided by 10, $\frac{\mu u}{10L_c(\Delta\tau)}$; lighter solid line is the dimensionless change of shear stress, $(\frac{\tau}{\Delta\tau})$: (a) present model; (b) Andrews (1976).

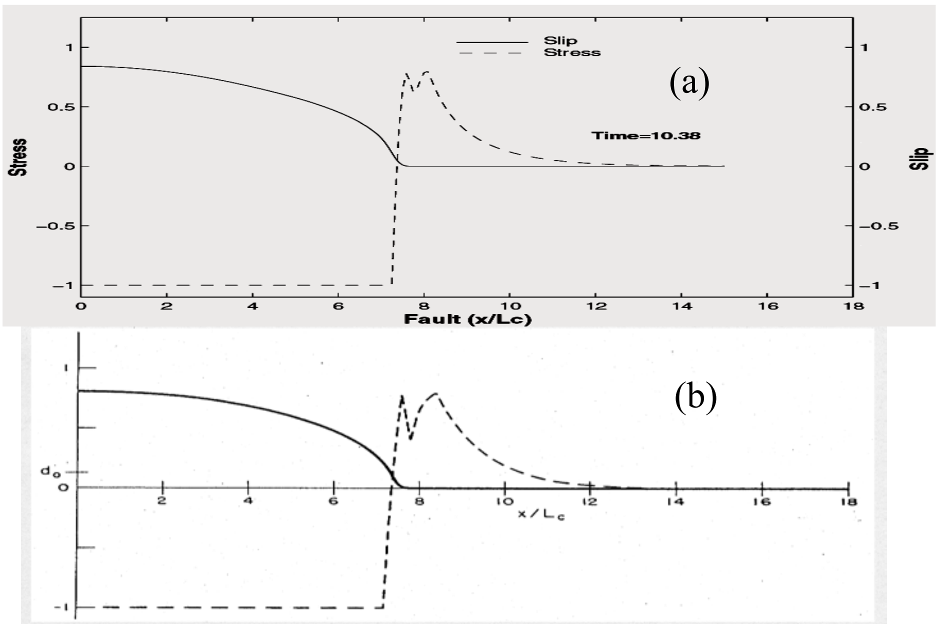

Figure 4.5. Shear stress and slip as a function of position on the crack plane at dimensionless time $\beta t/L_c$ = 10.38. Legend is the same as that for figure 4.3. (a) present model; (b) Andrews (1976).

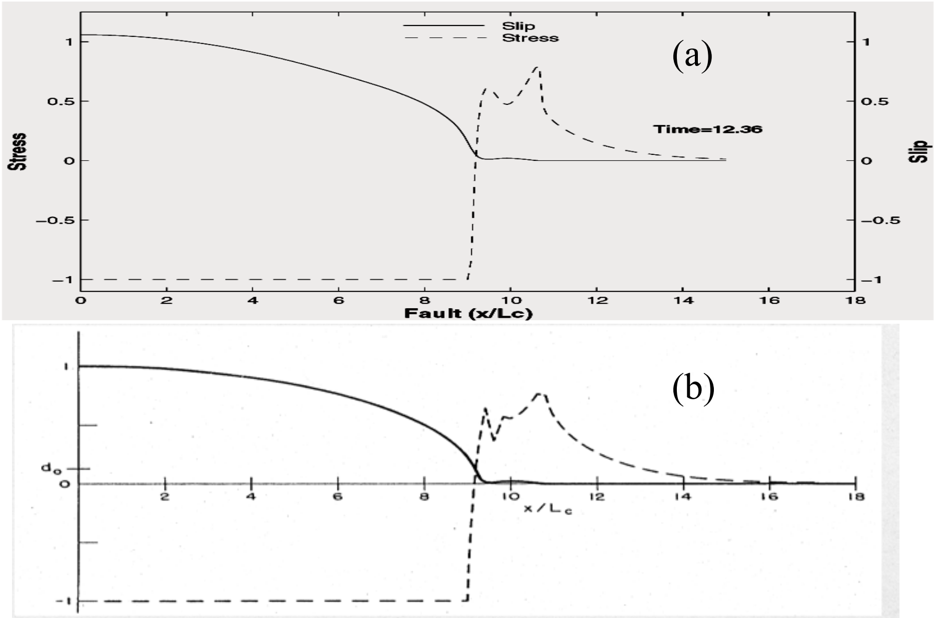

Figure 4.6. Shear stress and slip as a function of position on the crack plane at dimensionless time $\beta t/L_c$ = 12.36. Legend is the same as that for figure 4.3. (a) present model; (b) Andrews (1976).

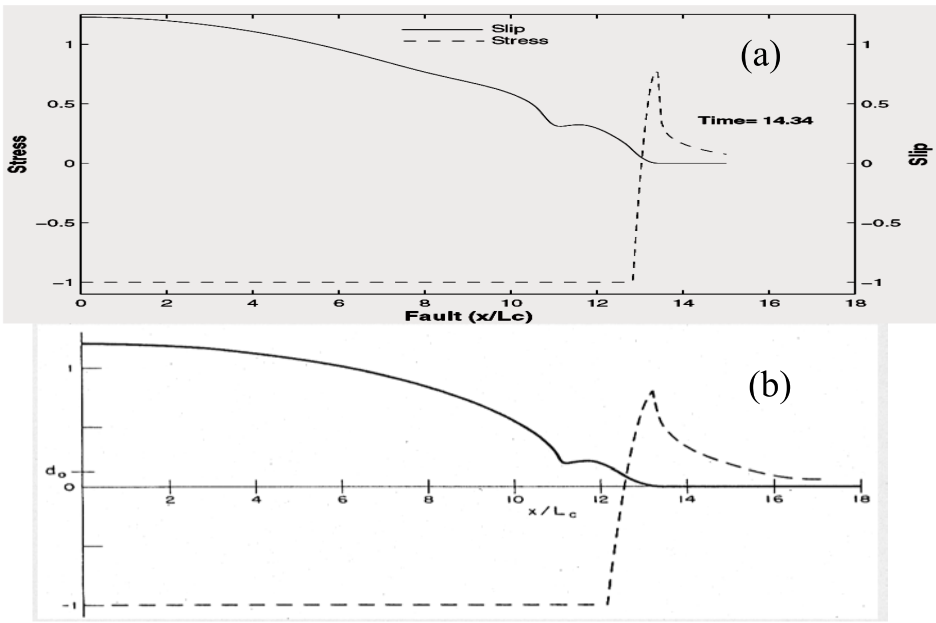

Figure 4.7. Shear stress and slip as a function of position on the crack plane at dimensionless time $\beta t/L_c$ = 14.34. Legend is the same as that for figure 4.3. (a) present model; (b) Andrews (1976).

Figure 4.2 shows the space-time distribution of rupture. The region between the two solid lines is the rupture front, where slip velocity is nonzero and stress drop is incomplete. Figure 4.3 shows the slip velocity as a function of position at the same instant, at dimensionless time $\beta t/L_c$ = 12.36. Figures 4.4 to 4.7 show the shear stress and slip as a function of position on the crack plane at dimensionless time $\beta t/L_c$ = 8.07, 10.38, 12.36 and 14.34 respectively. The peak of the shear stress on the rupture front as well as the secondary peak associated with the S waves are very precisely described by the DEM. The results are very consistent with the solution presented by Andrews (1976).

4.2 Dynamic rupture propagation in a 3D model

In order to verify the adequacy of using the DEM to simulate a dynamic rupture process in 3D, three problems presented by Madariaga et al. (1998) are herein analyzed: first, a circular shear fault that breaks instantaneously and does not propagate; second, a spontaneous growth of rupture that initiates from a circular asperity and does not stop; and third, a spontaneous growth of rupture on a finite circular fault. The slip weakening model as a friction law of the fault is adopted (Equation 3.13 and Fig.3.5)

4.2.1 Circular shear fault that breaks instantaneously and does not propagate

This problem was aproximated by Brune (1970) and solved numerically assuming circular symmetry by Madariaga (1976). Madariaga et al. (1998) also use this example to validate the Finite Difenece Method. In this problem, it is assumed that the fault appears instantaneously in the medium and that rupture occurs instantaneously inside a circular fault of radius R. The geometry of the problem is described in Fig. 4.8, the circular fault is on the x-y coordinate plane and slip is allowed just in the y direction, that is, the x component of the slip is zero. The fault is embedded in a infinite homogeneous, isotropic elastic medium with Poisson's coefficient 0.25, so $\alpha / \beta = \sqrt{3}$, where α is the P wave velocity and β the S wave velocity. The problem is solved for β=1, $\alpha = \sqrt{3}$, density ρ=1, rigidity μ=1, grid size Δx=1, radius of the circular fault R=11Δx. A simple Coulomb friction law along the fault is assumed, with a critical slip D_c=0. The critical stress is τ_u =1, while the initial stress is $\tau_o = \tau_u = 1$. This means that the strength excess is zero, so the fault is prestressed just before rupture and stress reduces instantly to zero at time t=0. With these assumptions the stress drop $\Delta\sigma$ is 1 everywhere in the rupture zone. The results are normalized following the scale used by Madariaga et al (1998), as follow:

Distance along the fault:	The unit of Δx (grid interval)
Time:	$t' = t\alpha/(H\Delta x)$ (H=1.0)
Slip:	$D' = D\mu/(2\Delta x\ \tau_u)$
Slip velocity:	$\dot{D}' = \dot{D}\mu/(2\beta\tau_u)$
Stress:	$\tau' = \tau/\tau_u$

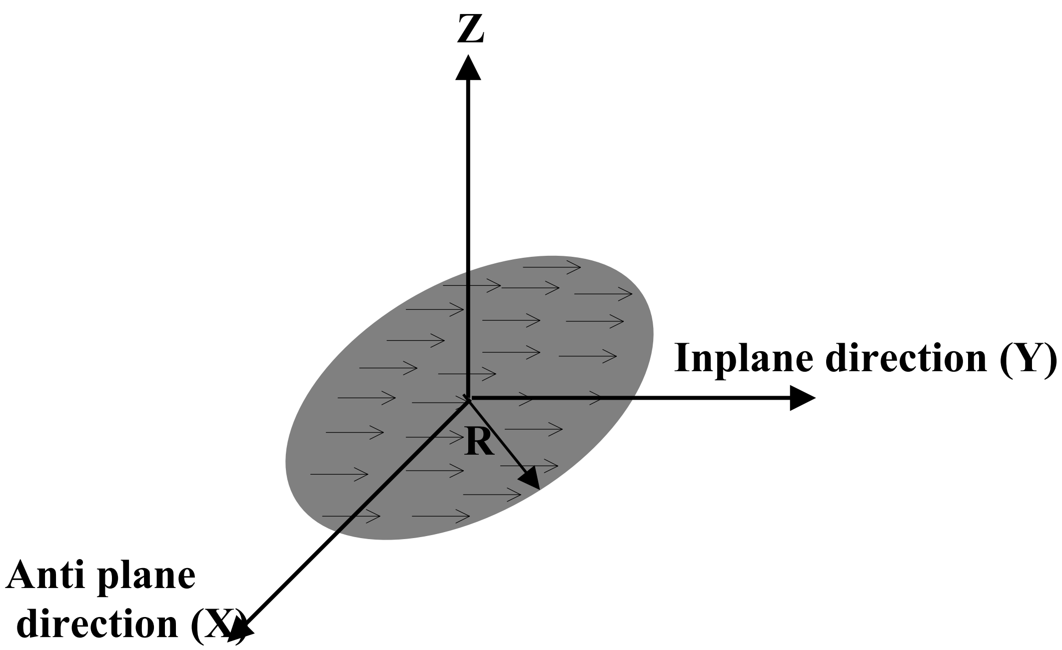

Figure 4.8. Theoretical circular fault that breaks instantaneously, the fault is on the *x-y* plane and the rupture occurs instantaneously inside a circular fault of radius *R*. The arrows show the direction on the slip.

Fig 4.9 show the slip function calculated by the DEM and by Madariaga et al (1998) at different points along the radius of the fault for the inplane direction (*y* axis) and antiplane mode (*x* axis). All the characteristics of the instantaneous rupture circular shear fault observed by Madariaga et al (1998) are very well reproduced by the DEM. For example, Madariaga et al (1998) explain that, after about 20 time units, the slip functions at the center of the fault show a break in slope corresponding to the arrival of the P stopping phase. After about 34 time units, the S stopping phase arrives in which the fault stops slipping. The solutions for the inplane and antiplane mode are similar but they are not exactly equal, so there is no cylindrical symmetry around the center of the fault.

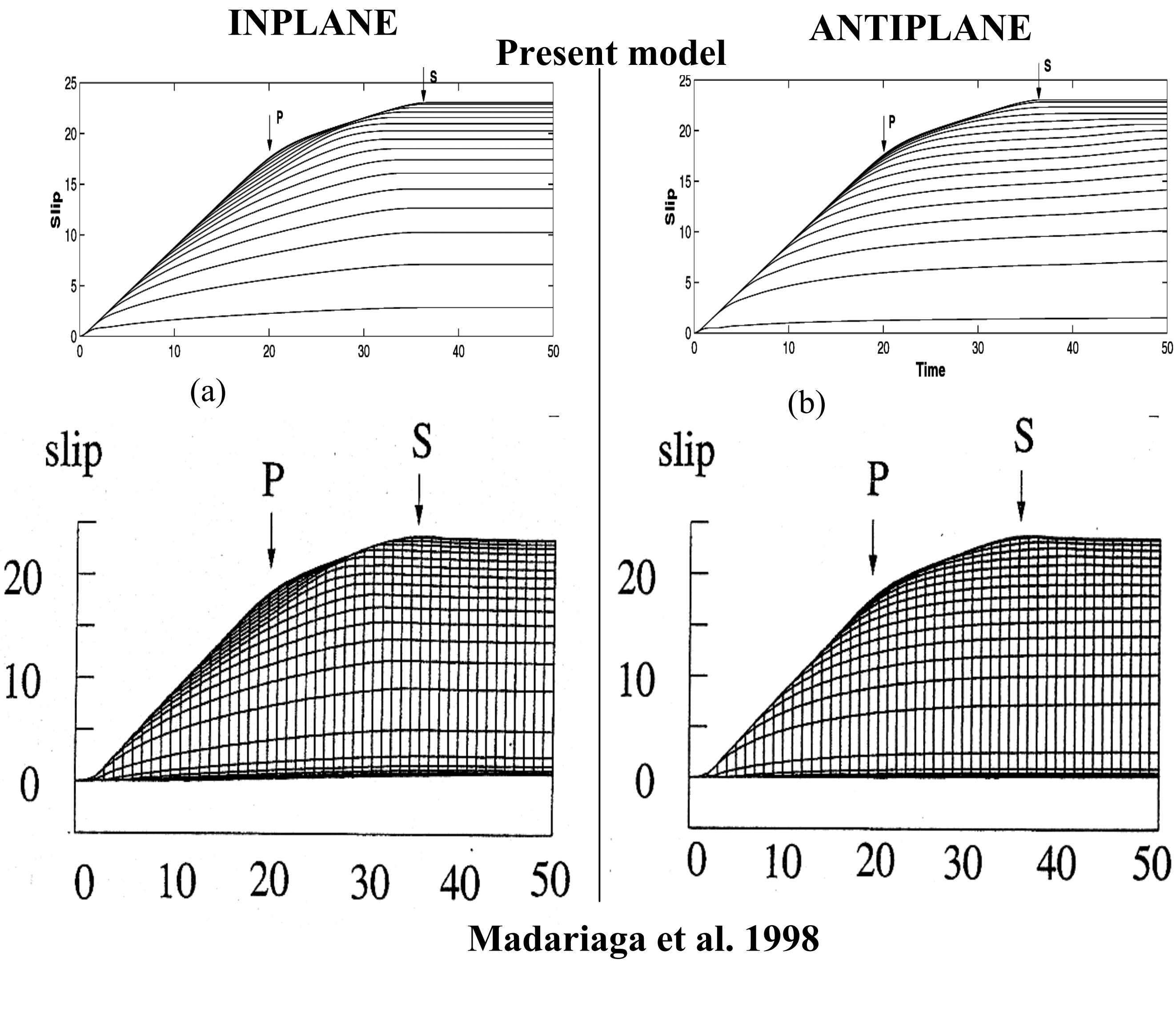

Figure 4.9. Slip as a function of time for an instantaneous circular fault rupture. Each curve represents the slip function at a different point along a radius of the fault. (a) slip for the inplane mode (along the y axis). (b) slip for the antinplane mode (along the x axis). At the top of the figures is the solution for the present model (DEM) and at the bottom is the solution presented by Madariaga et al 1998.

4.2.2 Spontaneous growth of rupture

In this problem the rupture initiates from a circular asperity, spontaneoulsly propagate and do not stop. This example was solved by Madariaga et al 1998 using FDM model. The geometry of the problem is the same described in Figure 4.8. The fault is on the *x-y* coordinate plane and the slip is allowed just in the *y* direction, that is, the x component of the slip is zero. The radius of the circular fault that break instantaneously is R=10Δx. The initial stress $\tau_o = 1.6\tau_u$ inside and $\tau_o = 0.5\tau_u$ outside the asperity, τ_u =1.0. In this problem the slip weakening friction law is used. In nondimensional units the critical slip $D_c = 4$, the normalized units for all the variables are the same used in the previous example. For the normalized time it is used H=0.35.

Figure 4.10 and figure 4.11 show the results of the spontaneous growth of rupture for the present model (DEM) and for the FDM presented by Madariaga et al (1998). The slip and stress distribution on the fault as a function of time and position along the in-plane direction shown in Figure 4.10a and b respectively is very similar with that obtained using the FDM (Figure 4.11 a,b). The time scale of figure 4.11 a,b has probably a typographical error, because this time scale do not correspond to the unit time specified in the paper of Madariaga et al (1998). In Figure 4.10c and d for the DEM, as well as figure 4.11 c and d for the FDM are shown the slip velocity and the stress distribution as a function of position along the inplane direction respectively at dimensionless time t'=200. All the properties of the spontaneous growth of rupture observed by Madariaga et al (1998) are very well reproduced by the DEM. For example, the peak of the shear stress on the rupture front as well as the secondary peak associated with the S waves are very precisely described by the DEM (Figure 4.10b and d). It was also very well simulated by the DEM for a two dimensional in-plane crack as presented in the section 4.1. As shown for the 2D problem (figures 4.4 to 4.7) when the stress field outside the fault is sufficiently strong, the rupture front becomes unstable, and the rupture jumps to the shear-wave velocity. This phenomenon was originally shown by Andrews (1976).

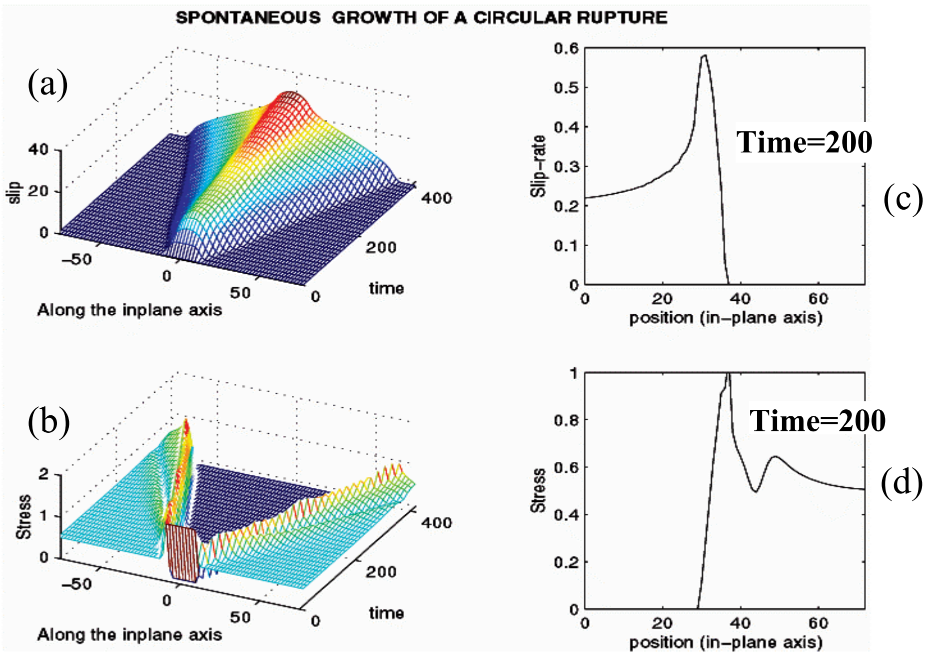

Figure 4.10. Numerical solution using the DEM of the spontaneous growth of rupture in which rupture initiates from a circular asperity, spontaneoulsly propagate and do not stop. Figure (a) and (b) show the slip and stress distribution on the fault as a function of time and position along the in-plane direction respectively. Figure (c) and (d) show the slip velocity and the stress distribution as a function of position along the inplane direction respectively at dimensionless time *t'*=200.

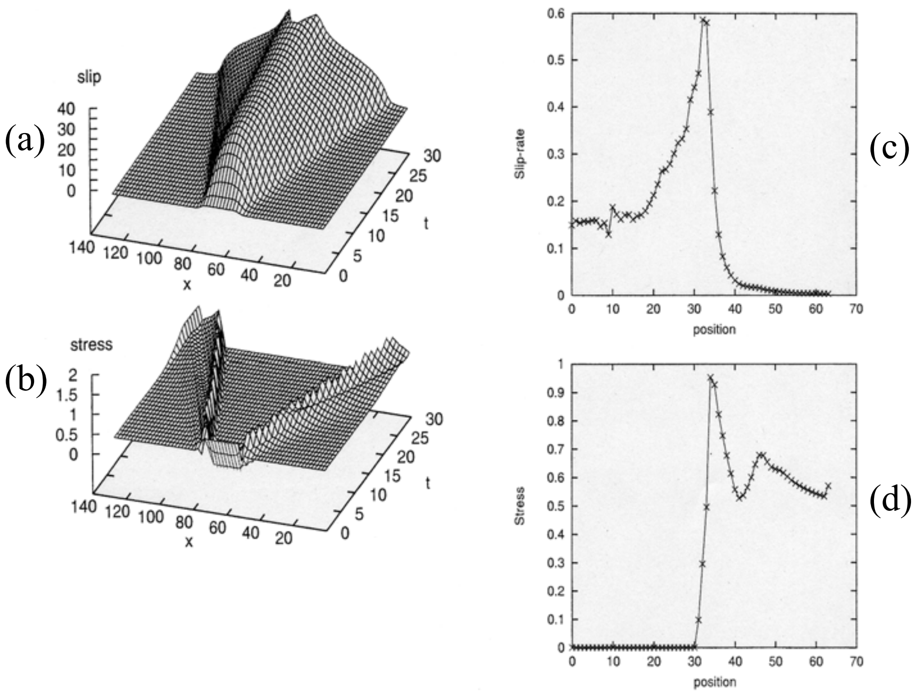

Figure 4.11. Numerical solution presented by Madariaga et al (1998) of the spontaneous growth of rupture in which rupture initiates from a circular asperity, spontaneoulsly propagate and do not stop. Description of figs. (a), (b), (c) and (d) are the same as in Fig. 4.10.

4.2.3 Spontaneous rupture on a finite fault

In this problem the rupture initiates from a concentric circular asperity and stop when it reaches unbreakable boundary of a finite circular fault. This example was solved by Madariaga et al 1998 using FDM model. The geometry of the problem is described in Figure 4.12. The fault is on the *x-y* coordinate plane and the slip is allowed just in the *y* direction, that is, the *x* component of the slip is zero.

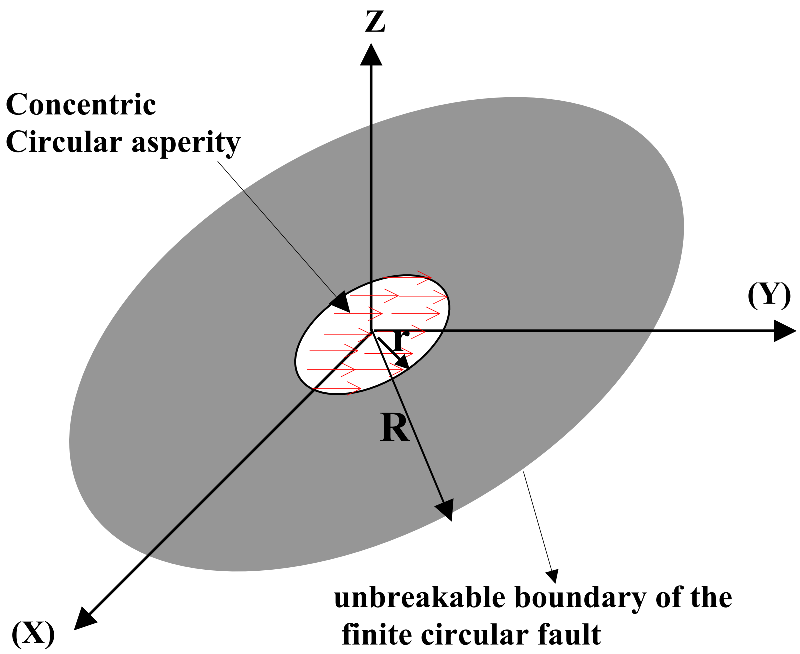

Figure 4.12. Theoretical finite circular fault. The fault is on the *x-y* plane, the concentric circular asperity breaks instantaneously and the rupture propagates until reaches the unbreakable boundary of the finite circular fault in which the rupture stop. The arrows show the direction on the slip.

The circular fault has a radius of R=50Δx. The rupture starts from a concentric asperity of radius r=6Δx. The slip weakening friction law is also used with a critical slip D_c=4. The initial stress inside the concentric asperity is $\tau_o = 1.2\,\tau_u$ and $\tau_o = 0.8\,\tau_u$ outside. The normalized units for all the variables are the same used in the previous examples

The results of the simulation are presented in snapshots of the slip velocity as shown in Figure 4.13 (for the solution using the present model) and in Figure 4.14 (for the solution using the FDM presented by Madariaga et al, (1998). The results using the DEM are also very similar with that calculated using the FDM. The rupture grow faster in the inplane direction, which is dominated by the mode II.

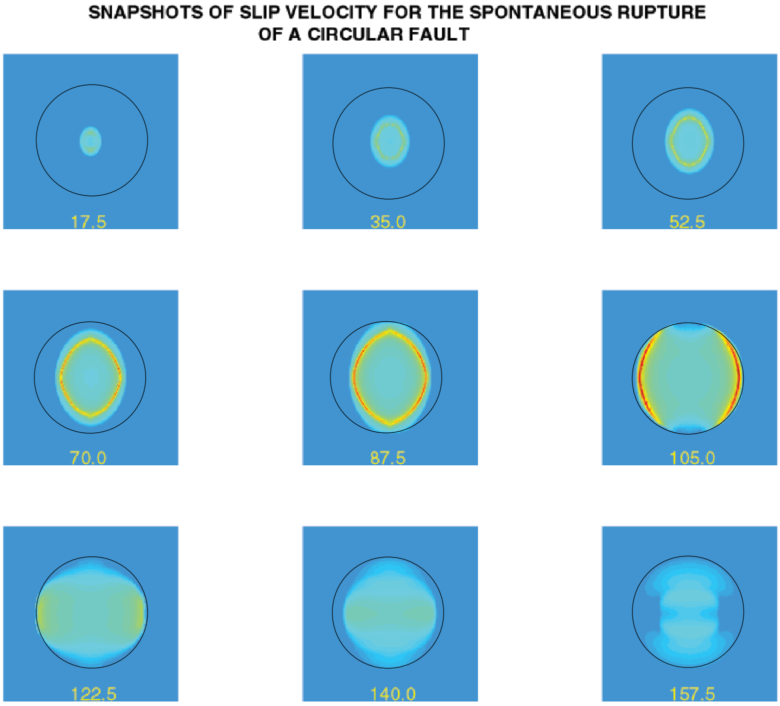

Figure 4.13. Snapshots of the slip velocity for a spontaneous rupture inside a finite circular fault calculated using the present model (DEM). The rupture starts overloaded a concentric circular asperity inside the finite circular fault. The nondimensional time for each snapshot is shown below each picture.

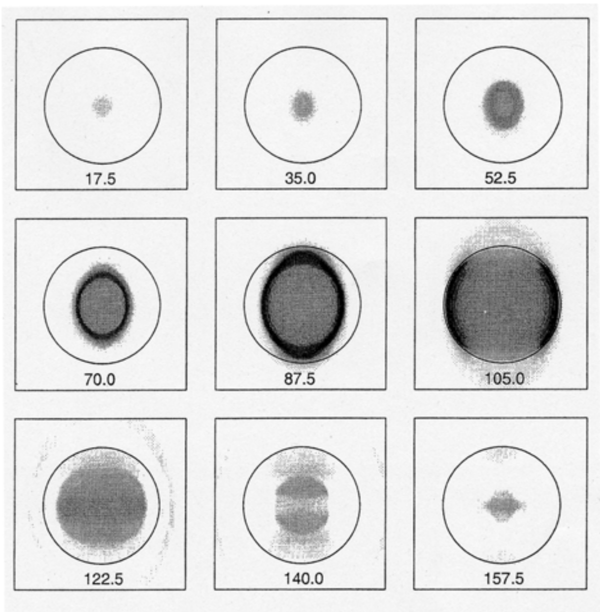

Figure 4.14. Snapshots of the slip velocity for a spontaneous rupture inside a finite circular fault calculated using the FDM presented by Madariaga et al (1998). The rupture starts overloaded a concentric circular asperity inside the finite circular fault. The nondimensional time for each snapshot is shown below each picture.

The problems analyzed to verify the adequacy of the DEM for the 2D and 3D model to simulate a dynamic rupture process were very well resolved by the DEM, the results are very consistent with the solutions presented in the specialized literature. Therefore, the 2D and the 3D DEM can be used very effectively to study spontaneous rupture propagation in a fault model embedded in an elastic medium.

Chapter 5

Parameters Estimation for Dynamic Simulation.

5.1 Esimation of Stress-drop, Strength Excess and Critical Slip.

For the 3D dynamic spontaneous rupture simulation of a real earthquakes we need to know: the geometry of the fault, the initial stres distribution along the fault, the stress drop distribution, the strength of the fault to break and the critical slip (if slip weakening friction model is used). The choice of these parameters used for the simulation of the dynamic rupture of a fault is a delicate issue, still subject of debate. Assuming that the effective stress to slip is the stress drop, we do not need to know the absolute level of the stress, therefore, the initial stress could be assumed to be in the zero level. Then, for the assumption of a slip weakening friction law, we need to define the stress drop, the strength excess and the critical slip along the fault. These parameters could be estimated from the shear stress function that changes in time during and earthquake as schematically show in Fig. 5.1a. But the direct estimation of this shear stress change from observations is not feasible, the closest information about the source that we have is the results of the kinematic waveform inversion given by the slip distribution in time (Fig. 5.1b) along the fault. In this context, for the computation of the shear stress changes during earthquake rupture we use the distribution of fault slip and rupture time obtained from the inversion of strong motion waveforms. For this purpose, using the DEM, we model the continuum surrounding the pre-existing fault as specified by the kinematic model and we solve the elastodynamic equation of motion of the continuum for a rupture along the fault plane. The slip distribution in space and time obtained by the kinematic fault model is used as a boundary condition along the pre-existing fault; this allows the determination of the relative stress time history (Fig. 5.1a) at every nodal point along the fault. This procedure, i.e., determination of the dynamic stress change from the results of kinematic waveform inversion, has been used by several authors [e.g., Quin, 1990; Miyatake, 1992; Mikumo and Miyatake, 1995; Bouchon, 1997; Day et al., 1998; Mikumo et al., 1999), most of them using the finite-difference method.

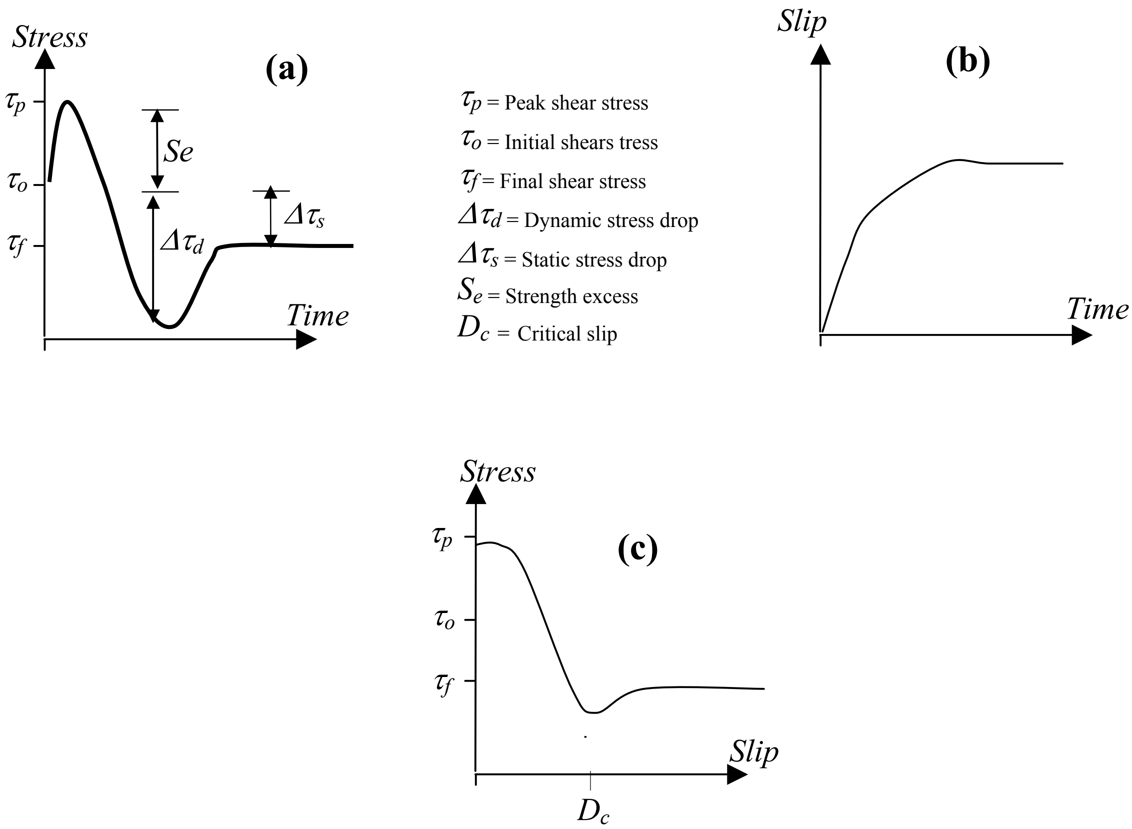

Figure 5.1. Characteristics of shear stress and slip function on any discrete point of a fault and dynamic paramenetrs specification. (a) shear stress time history; (b) slip time function; (c) shear stress *Vs* slip function.

From the results of the stress-time function (fig. 5.1a) the strength excess, the dynamic.and static stress drop could be estimated. From the expression of the stress in function of the slip as observed schematically in Fig. 5.1c, the critical slip could be roughly estimated.

Fig. 5.2 shows schematically the global procedure of the dynamic rupture simulation based on the results of kinematical wave form inversion.

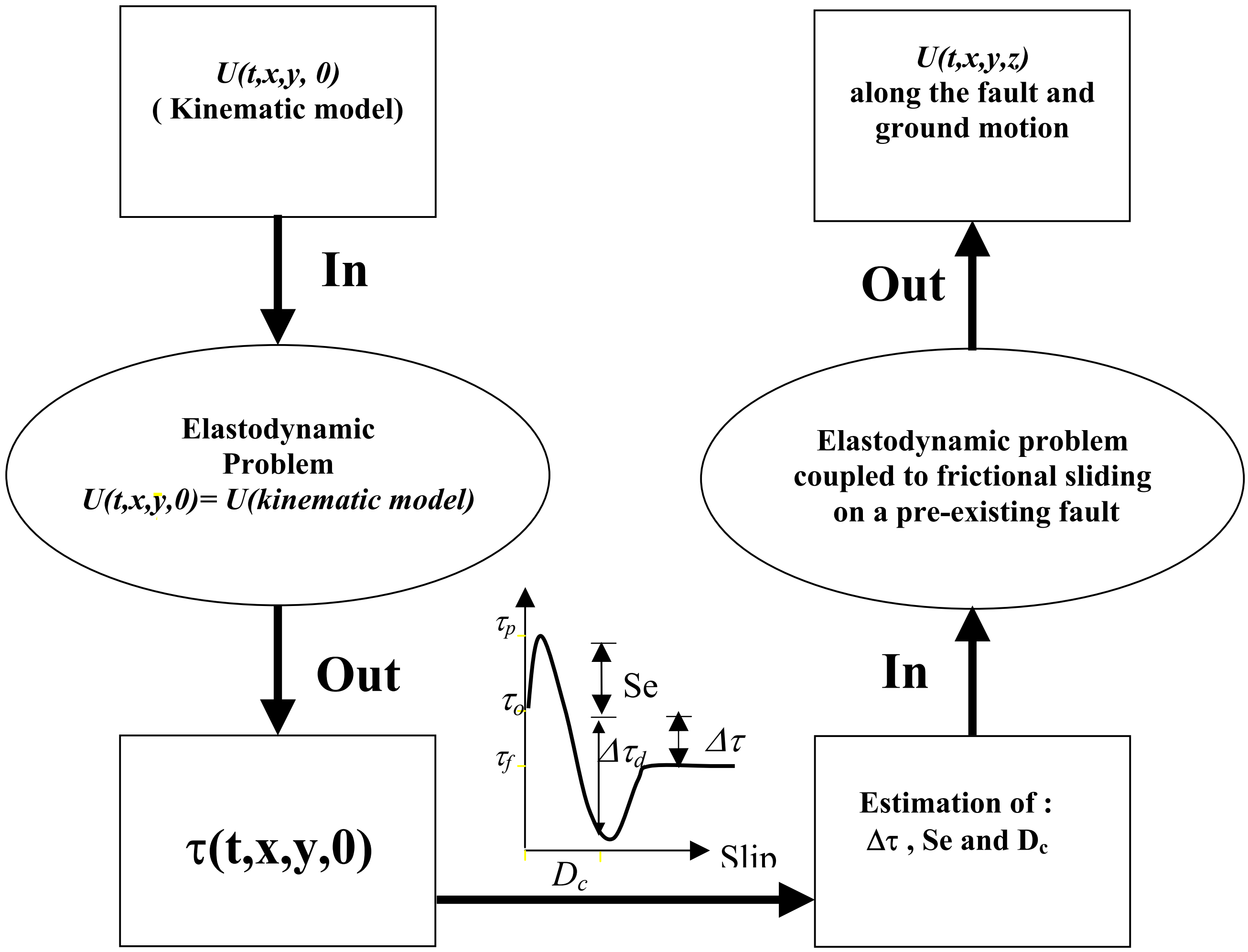

Figure 5.2. Schematic representation of the global procedure of the dynamic rupture simulation based on the results of kinematical wave form inversion.

5.2 Aplication to the 2000 Tottori Earthquake

For the estimation of the dynamic parameters (stress drop, strength excess and critical slip) we follow the procedure described above. The distribution of fault slip of the 2000 Tottori earthquake obtained from the inversion of strong motion waveforms calculated by Iwata et al. (2000) was used. We adopted the fault plane properties defined by Iwata et al. (2000), i.e., a fault plane with strike N150E and dip 90^o, fault length and width are 33km and 21km. The subfault-size is 3x3km square (it implies a grid size of the DEM equal to 3km) With the hypocenter at a depth of 13.4km. The velocity structure is shown in Table 5.1.

(a)

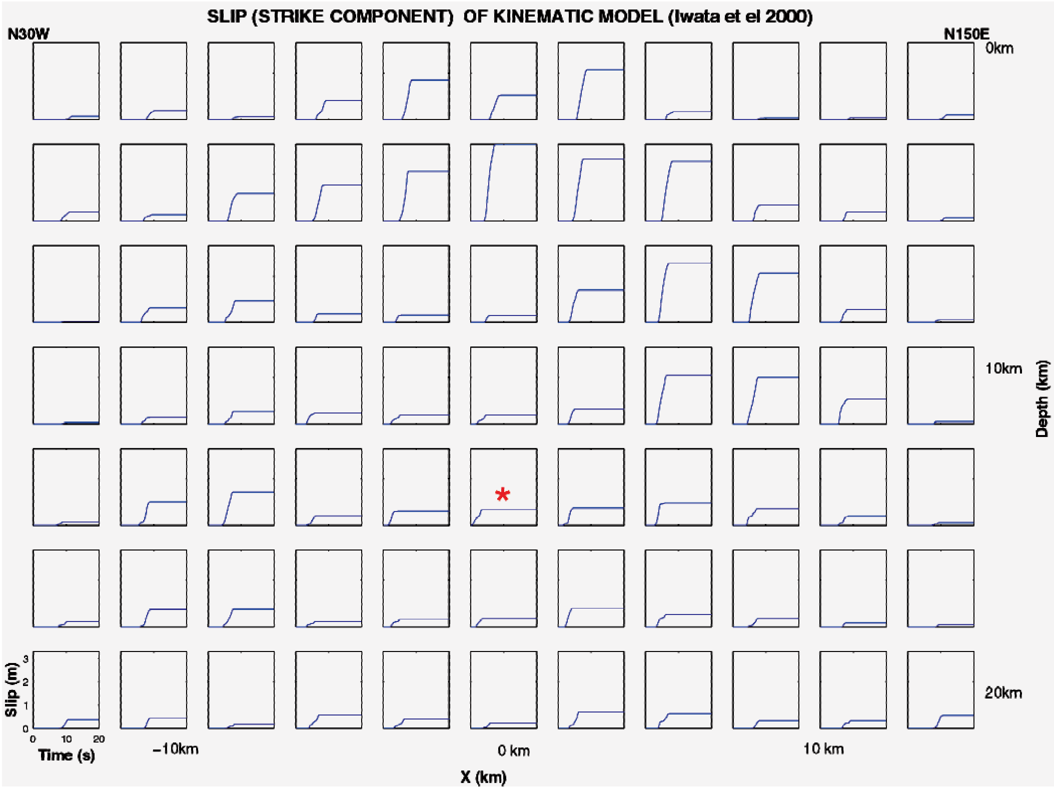

(b)

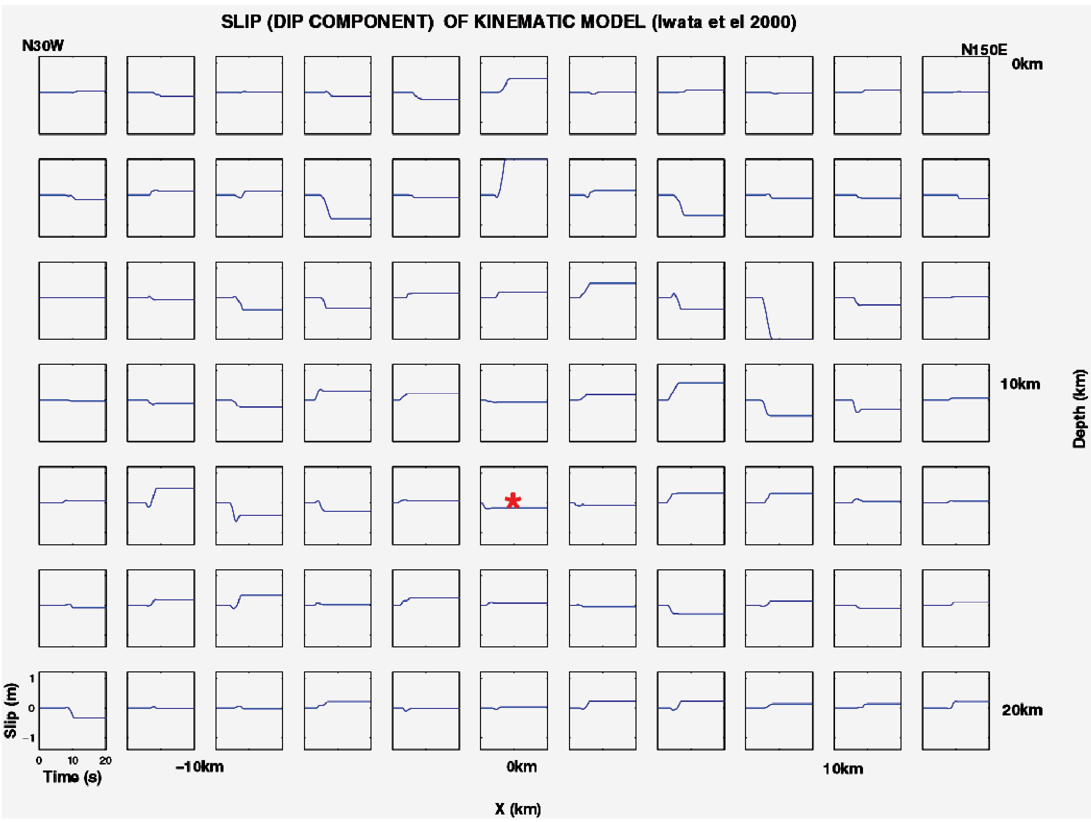

Figure 5.3. Slip time function for each sub fault given by the kinematic model and calculated by Iwata et al (2000). (a) strike component, (b) dip component.

Table 5.1. Velocity structure

Depth (km)	Vp (km/s)	Vs (km/s)	ρ (kg/m^3)
0	5.5	3.179	2600
2	6.05	3.497	2700
16	6.6	3.815	2800
38	8.03	4.624	3100

The slip time function for each sub fault given by the kinematic model as shown in Fig. 5.3 is used as a boundary condition along the pre-existing fault to solve the elastodynamic equation of motion of the continuum for a rupture along the fault plane.

The results are given by the strike and dip component of the stress time function for each subfault. But the results of interest are the stress in the direction of the total slip. For this purpose, the dip and strike component of the stress are decomposed to calculate the total stress in the direction of the total slip. If the total stress increases with the slip (hardening) a negative stress drop takes place, on the contrary, if the total stress decreases with the slip (weakening) a positive stress drop takes place.

Fig. 5.4a shows the total stress with time, from which the strength excess, the dynamic and static stress drop could be estimated. Fig. 5.4b shows the total stress-slip function, from which the critical slip could be estimated. The criterion used for the estimation is the direct observation by eyes for each stress function following the specifications of Fig. 5.1. Considering the uncertainty of the definition of these parameters, this criterion is enough to start the simulation of dynamic rupture process.

(a)

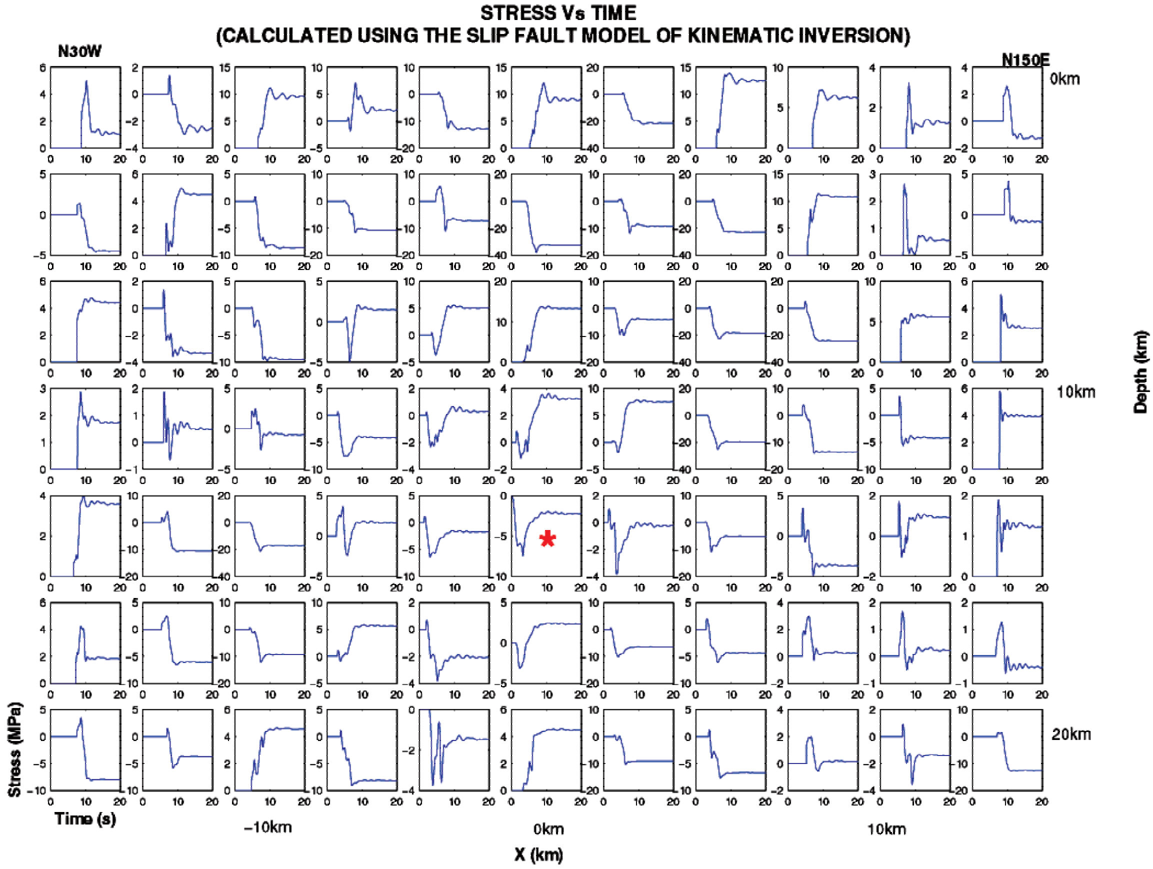

(b)

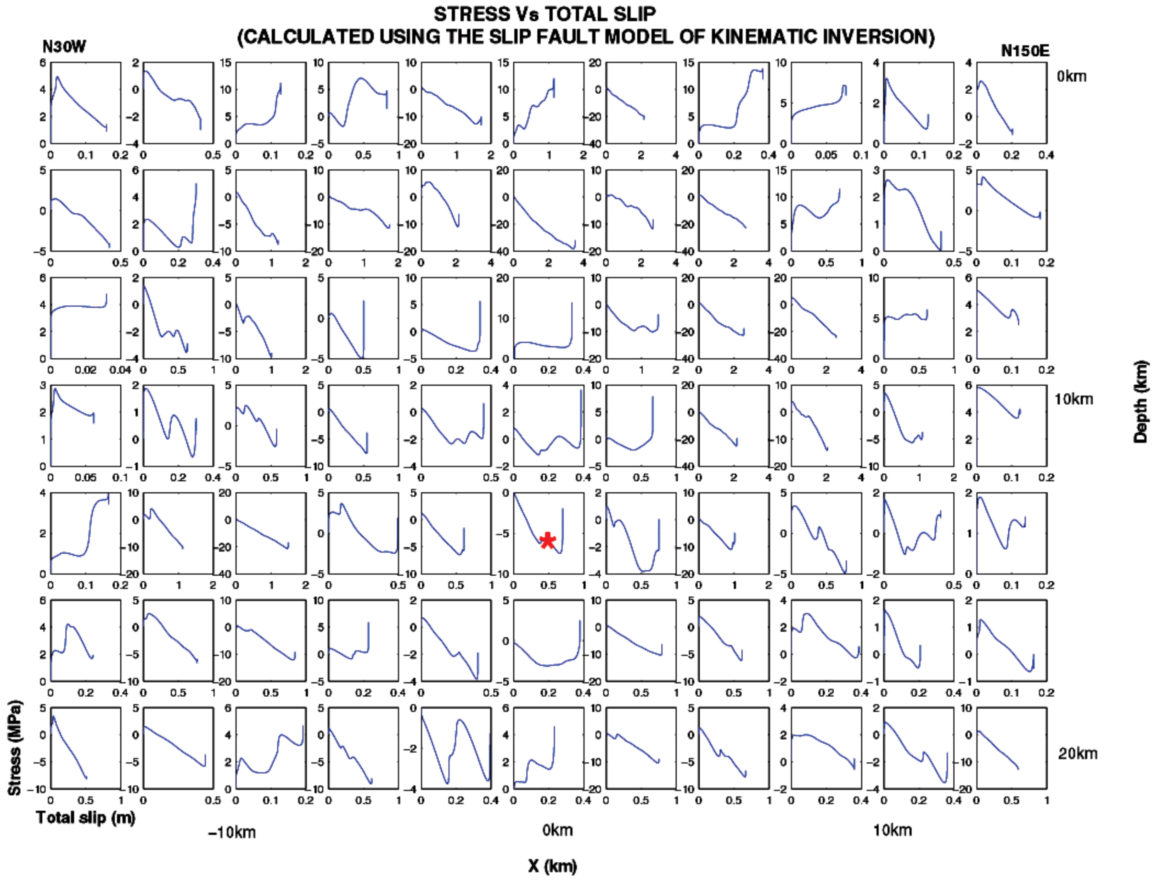

Figure 5.4. Total shear stress distribution for each sub-fault calculated from the kinematic source model. (a) total shear stress time function; (b) total shear stress-slip function

The distribution of the dynamic and static stress drop estimated from Fig. 5.4a is shown in Fig. 5.5a. In order to validate these results we compare with the results evaluated using the approach presented by Bouchon (1997) and calculated by Zhang et al. (2001), as shown in Fig. 5.5b, in which subfaults of size 0.5x0.5km was used. On account of the difference between grid sizes used in the two models, the approach of Bouchon leads to sharper plots than those resulting from the DEM. But in general both sets of results are perfectly consistent.

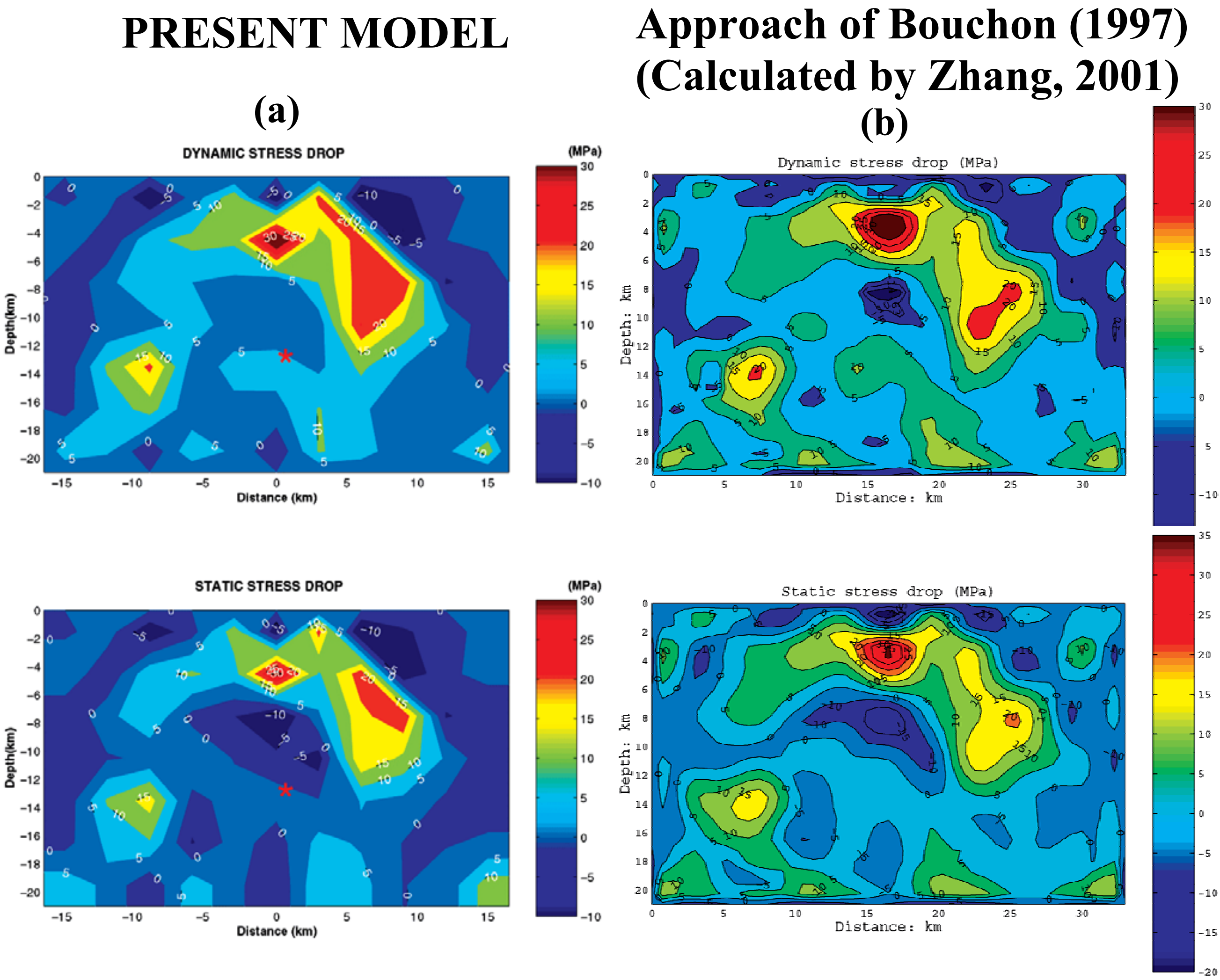

Figure 5.5 Distribution of the dynamic and static stress drop estimated from the results of kinematic source model of Iwata et al (2000) of the 2000 Tottori earthquake. (a) Results using the Discrete Element Method (present model); (b) results calculated by Zhang et al. (2001) using the approach of Bouchon (1997)

From Fig. 5.5 we can observe that there is a localized asperity in the upper central part of the fault. The maximum stress drop is 30 MPa in the asperity zone; while the dynamic stress drop shows negative values near the free-surface and at the left and right sides of the fault. This suggests that the stress continuously accumulate during the rupture process (hardening). The static stress drops in the asperities zone are very close the dynamic stress drops, but at the center of the fault and in the surrounding area of the asperities the stress is negative (max. -10Mpa), indicating that the stress in the asperity zone completely releases but in the surrounding area the stress increases after the rupture process of the earthquake.

Fig. 5.6 shows the strength excess distribution along the fault. Maximum values occur at the left and right sides of the fault, reaching around around 5MPa. The minimum values take place in all the central fringe of the fault except in a small portion between depths of 4 and 9km where moderate strength excess of 4MPa are determined. It suggests that the tectonic shear stress had reached close to the level of the critical stress before the earthquake in almost all the central fringe of the fault.

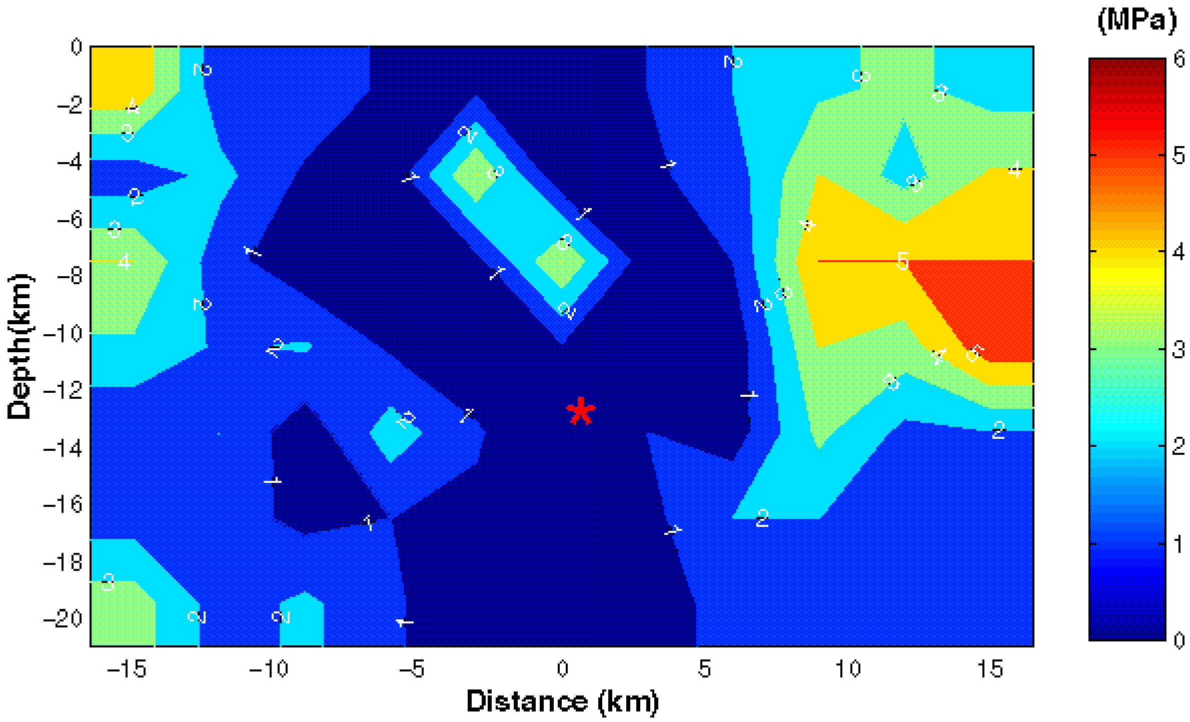

Figure 5.6. Strength excess distribution along the fault estimated from the results of kinematic source model of Iwata et al (2000) of the 2000 Tottori earthquake.

From the results shown in Fig. 5.5 and 5.6, we may conclude that the causative fault of the 2000 Tottori earthquake has a very heterogeneous stress distribution, with a localized asperity in the upper central part of the fault. Fault zone heterogeneity is now widely accepted in the study of earthquakes. The classical definition of asperities and barriers (e.g., Kanamori and Stewart, 1978; Aki, 1984), in which both terms are related to the absolute level of shear stress and strength distribution along the fault plane, is a simple as well as a robust description of such heterogeneity. This may also be important in controlling the number of foreshocks, i.e., the stronger the heterogeneity the greater the number of foreshocks (Dodge and Beroza, 1996). Certainly the same concept is also valid for the number of aftershocks. The stress heterogeneity associated with the foreshocks and aftershocks of the 2000 Tottori earthquake is going to be presented in the next item.

Fig. 5.7a shows the critical slip distribution along the fault. The critical slip (D_C) was estimated approximately from the zone in which the stress has positive stress drop. The approximated values of D_C vary with depth, being 2m near the free-surface, 1.0m in the center of the fault and 0.4m in the deepest zone as shown in Fig. 5.7b.

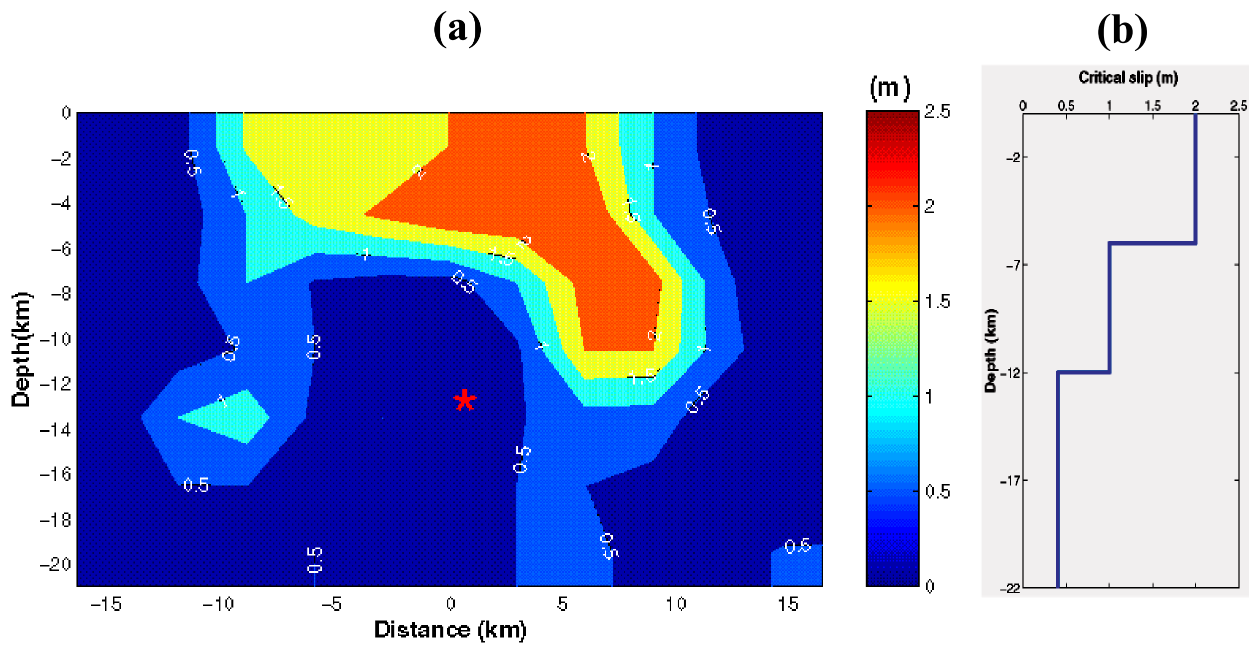

Figure 5.7. (a) Critical slip distribution along the fault estimated from the results of kinematic source model of Iwata et al (2000) of the 2000 Tottori earthquake. (b) Approximated values of D_C varying with depth.

5.2.1 Foreshock and aftershock associated with the stress distribution a long the fault of the 2000 Tottori earthquake.

The foreshock distribution is the manifestation of an earthquake nucleation (e.g., Jones et al., 1982; Jones, 1984; Dodge and Beroza, 1996; Ellsworth and Beroza, 1998) and the aftershock are triggered by the main shock, in response to the stress changes caused by the dynamic process of the earthquake. The physical understanding of the interaction between the foreshock, main shock and aftershock remains unresolved. Within this context, however, the study of Harris (1998), who reviewed many published works and presents a compilation of quantitative earthquake interaction studies from a stress change perspective, suggests that the stress changes may explain aspects of this phenomenon.

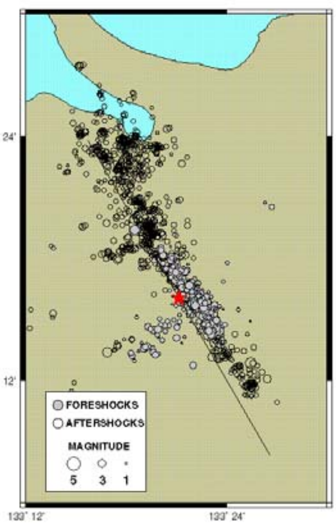

(a)

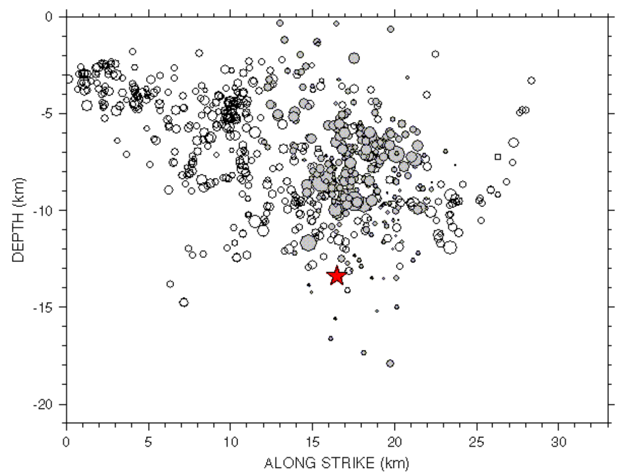

(b)

Figure 5.8. Comparison of the relocated hypocenter distribution of the seismic activity in 1989, 1990, 1997 (foreshocks)and 2000 (aftershocks) determined by Shibutani et. al. (2001). The solid line and the start correspond to the fault plane and epicenter of the 2000 mainshock respectively a) Map view; b) Along the fault plane.

The recent 2000 Tottori-ken Seibu earthquake (Mj=7.3) provides us a good chance to study the problem of earthquake interaction. Shibutani et al. (2001) reported a swarm seismic activity including six moderate events (Mj=5.1-5.4) occurred in 1989, 1990 and 1997 in the same area of this earthquake (Fig. 5.8). These authors carried out a temporary seismic observation in and around the source area and processed the data to determine the hypocenters location of the preceding seismic activity, the main shock and the aftershock (Joint Group for Dense Aftershock Observation of the 2000 Tottori-ken Seibu Earthquake, 2001). The relocated hypocenter distribution of the three preceding swarms as well as the 2000 activity determined by Shibutani et. al. (2001) show that these events occurred on the same fault plane as the Tottori earthquake and were distributed on specific areas within the fault plane (Fig. 5.8). In this context, we define the seismic activity of 1989, 1990 and 1997 as foreshock because they broke weak zones on the same fault plane of the main event and could be the manifestation of nucleation of the Tottori earthquake.

The first intuitive interpretation of this seismic activity preceding and succeeding the 2000 earthquake could be due to a possible strong heterogeneity over the fault plane, i.e., some of the strong patches on the fault behave as asperities and others as barriers. In order to explain some aspect of the space distribution of these foreshock and aftershock we can associate them with the dynamic stress distribution calculated in the previous item, that is the strength excess, the dynamic and static stress drop distribution. In Fig. 5.9 and 5.10 we compare foreshock and the aftershock location with the strength excess and stress drop distribution, respectively.

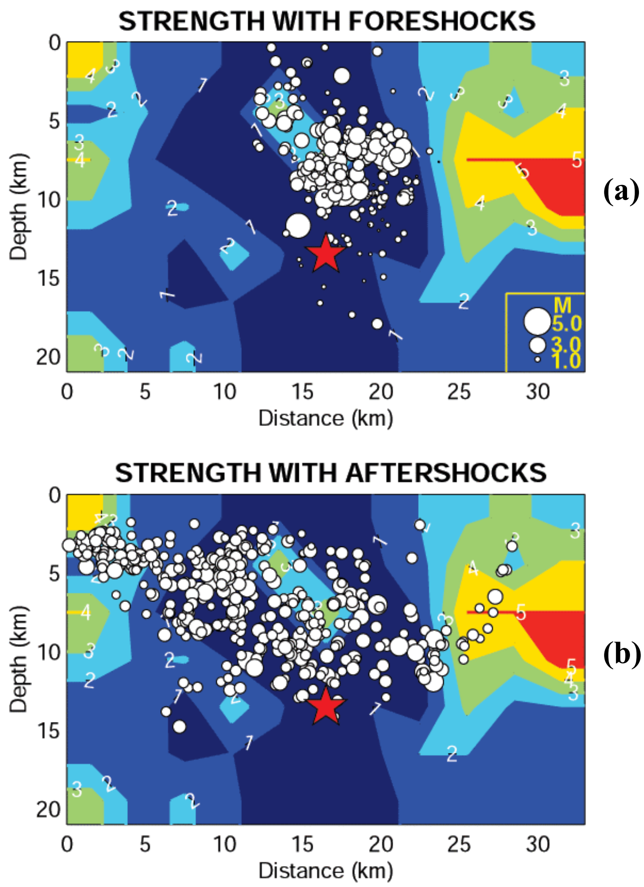

Figure 5.9. Comparison of the strength excess distribution with: (a) swarm seismic activity in 1989, 1990, 1997 (foreshock) and (b) aftershocks

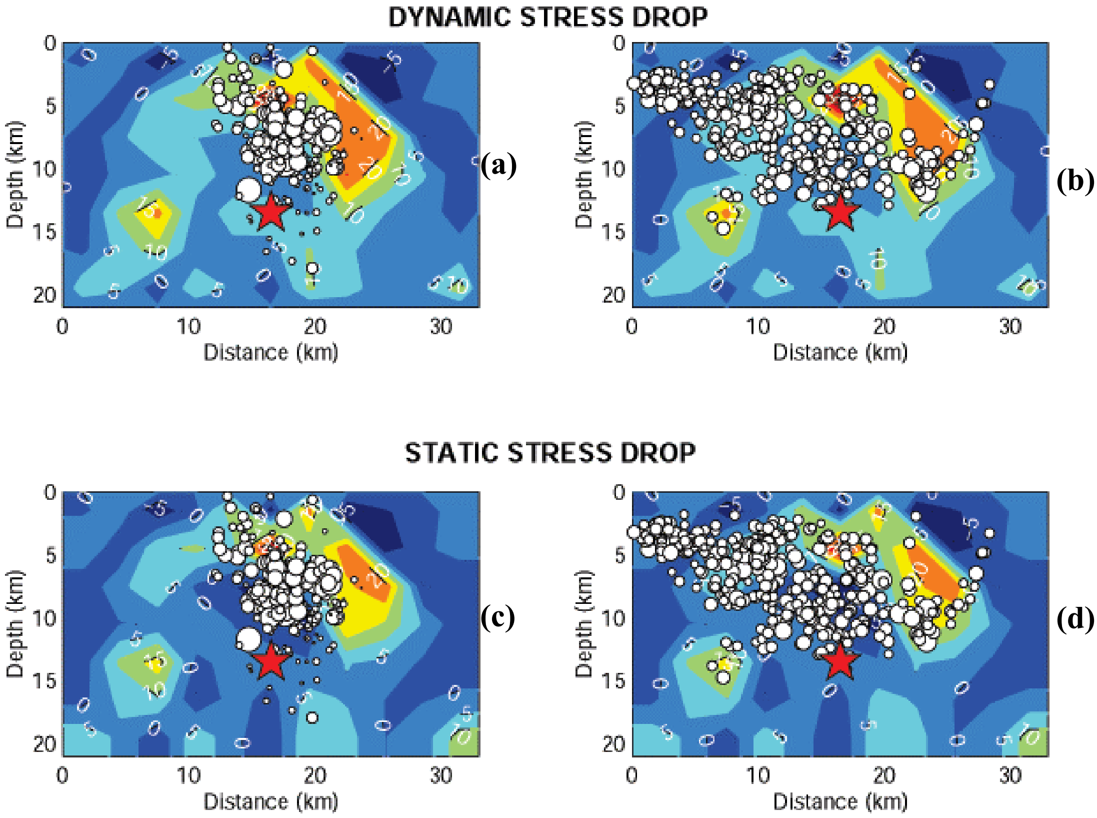

Figure 5.10. Comparison of the swarm seismic activity in 1989, 1990, 1997 (foreshock) and aftershocks with the dynamic and static stress drop distribution; a) foreshocks and dynamic stress drop; b) aftershock and dynamic stress drop; c) foreshock and static stress drop; d) aftershock and static stress drop.

From Fig. 5.9a we can observe that the foreshocks distribution was confined to a finite zone localized in the central part of the fault. Most of these events are located in the zone where the strength excess is very small. This suggests that the zones where the strength excess is larger behaved as barriers, being possibly responsible for arresting the rupture in the 1989, 1990 and 1997 events. In Fig.5.9b it may also be observed that the aftershocks happened in this confined zone and on the left side of the fault. Apparently the right side, which presents the largest values of strength excess, was the strongest barrier. From Fig. 5.10a,c, we can observe that this confined zone is located below the asperity in the area where the dynamic stress drop is almost zero and the static stress drop is negative. It suggests that the asperity was also a barrier for the rupture process of the three swarms. The central zone where the dynamic stress drop has almost zero values, imply that in this zone the stress was already relaxed or dropped during the previous seismic activity. But the question arise why does this seismic activity occur in this confined zone? And why the existence of this confined zone? Does the main shock was triggered by the stress changes from this previous swarm seismic activity? Shibutani et al. (2001) suggest that the 2000 Tottori earthquake and the preceding seismic activity might have been triggered by crustal fluids because this source area is located between the Daison Volcano, which was active during the Pleistocene, and the Yokata monogenic volcanic cluster, which was active in the early Pleistocene. Ohmi and Obara (2001) reported that several deep low-frequency earthquakes were found near the source area. If we observe the static stress drop distribution of Fig. 5.10c,d, this confined zone has considerable negative static stress drop. It seems to be that this zone is very active in which the stress accumulate faster than any other places on the fault. The biggest aftershocks happen in this zone (Fig. 5.10b,d), and probably this zone will continue active.

The calculation of the dynamic stress changes during the rupture process of the 2000 Tottori earthquake using the DEM shows important characteristics of this earthquake associated with the foreshock and aftershock distribution, confirming that the DEM may be reliably used in the analysis of dynamic stress changes during the rupture process of an earthquake.

But from the analysis it is not clear whether the main shock was triggered by stress changes from the foreshocks, but certainly the foreshocks distribution is the most obvious manifestation of earthquake nucleation, so that earthquake prediction might require more detailed knowledge of the stress and strength distributions on faults.

This part of the work was submitted to the Journal "Geophysical research Letter" (Dalguer et al., 2001c).

Chapter 6

Application of the Model in 2D

6.1 Preceding works

The model was used to simulate variable problems in 2D. Riera and Rocha (1991) used the approach in fracture studies, these authors simulate the propagation of only tensile cracks, their results converge with available theoretical predictions. Doz and Riera (1995) employed the method to model the stick-and-slip motion along friction surfaces, Dalguer et al. (1999) evaluated the foreshock and periodicity of earthquakes, Dalguer et al. (2001a,b) simulate successfully the dynamic shear rupture process of the 1999 Chi-chi (Taiwan) earthquake. Detail information of the DEM and its application to several dynamic problems in 2D related to the rupture process of an earthquake may be found in Dalguer (2000).

As an example of the works listed above for the application of the model to simulate dynamic rupture process of an earthquake in 2D, one of the problems solved by Dalguer (2000) and presented in Dalguer et al. (2001a) is shown in Fig. 6.1. In this figure the snapshots every one seconds for the velocity parallel to a dipping fault during 12 seconds is shown. This figure corresponds to the results of the dynamic rupture process of the reverse fault near the hypocentral area of the 1999 Chi-Chi (Taiwan) earthquake. As observed in Fig.6.1, Dalguer et al. (2001a) showed that this kind of fault generates large differences between the near-source ground motions on the hanging wall and on the footwall. The ground motions on the hanging wall are larger than in the footwall, the numerical simulation suggests that such a difference is principally caused by the asymmetric geometry of the hanging wall and footwall. For this earthquake, where the rupture of the fault reaches the surface, the effect of the asymmetry on the ground motion is considerable. The characteristics of this kind of earthquakes (dipping fault) were also shown by Mikumo and Miyatake (1993) in their investigation of the dynamic rupture process of the 1961 Kita-Mino earthquake in central Japan and by previous theoretical dynamic simulation of dipping fault, for example Nielsen (1998), Shi et al. (1998), Oglesby et al. (1998, 2000), as well as that observed in the foam rubber experiment of a thrust fault presented by Brune (1996).

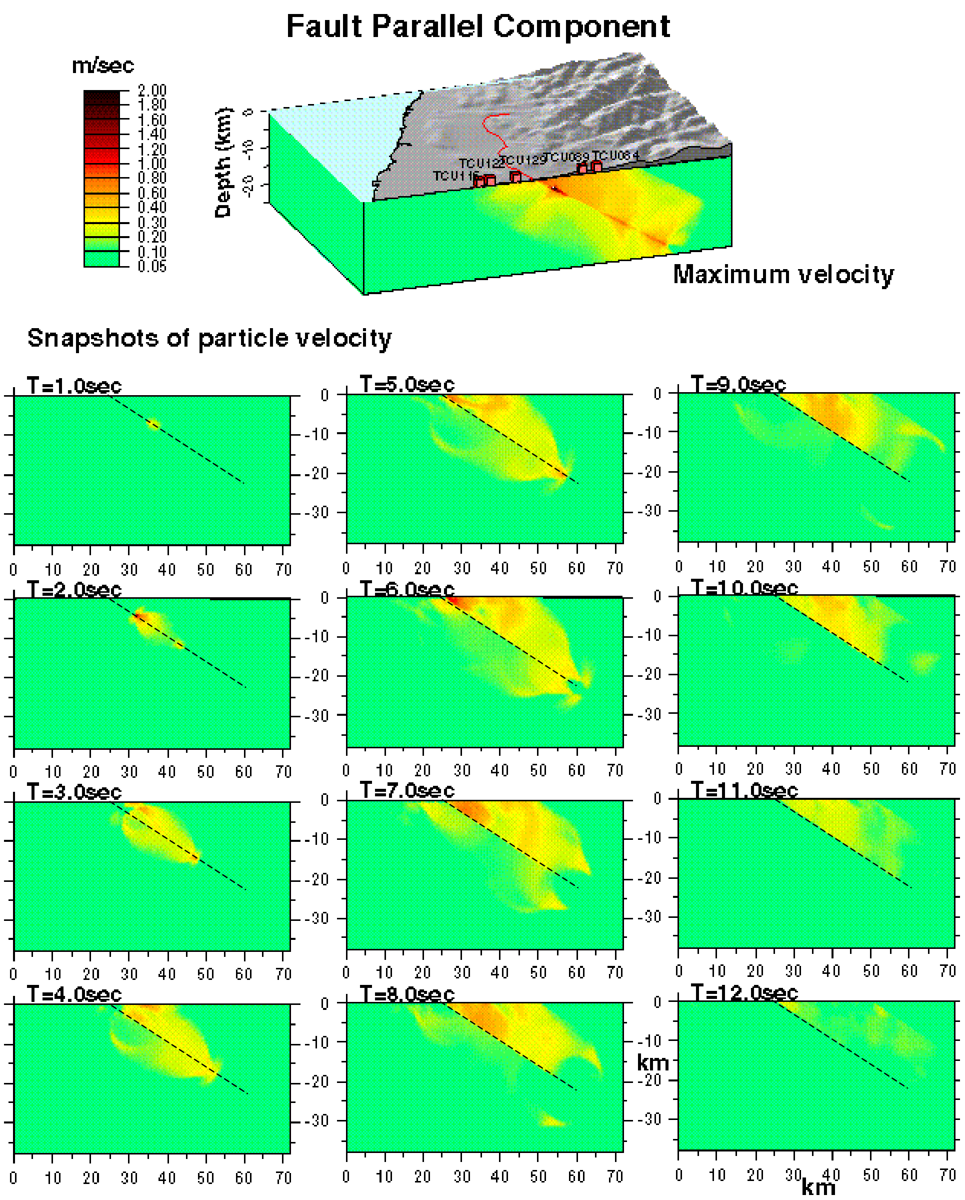

Figure 6.1. Results of the dynamic rupture process simulation of the reverse fault near the hypocentral area of the 1999 Chi-Chi (Taiwan) earthquake presented by Dalguer et al. (2001a). The figure shows the maximum velocity and snapshots (from 1 to 12 sec. after the rupture starts) of the particle velocity fault parallel component. The dashed line represents the pre-existing fault. The computational domain is clearly showed by the maximum velocity figure (boundary between the yellow and green color).

6.2 Application of the 2D Model in the Present Thesis

6.2.1 The effects of strength excess and critical slip on the near source ground motion of dipping faults that break the free surface.

In the present thesis, the dynamic rupture process of a dipping fault that breaks the free-surface is simulated in order to study the effects of the strength excess and critical slip on the near source ground motion. The purpose of this study is to show the importance in the choice of these parameters to the analysis of the near source ground motion when slip weakening model is used as a friction law in the dynamic simulation.

Many numerical simulations of the dynamic rupture process of an idealistic dipping fault are developed. The problem is tackled in a plane strain condition. The fault model used for the dynamic simulation are shown in Fig. 6.2. The homogeneous medium is characterized with P wave velocity (6.1 km/sec), S wave velocity (3.5 km/sec), density 2700 kg/m^3 and Poisson's ratio 0.25. The dip of the fault is 33^o 41', length 100km, the hypocenter is located at a depth of 28km.

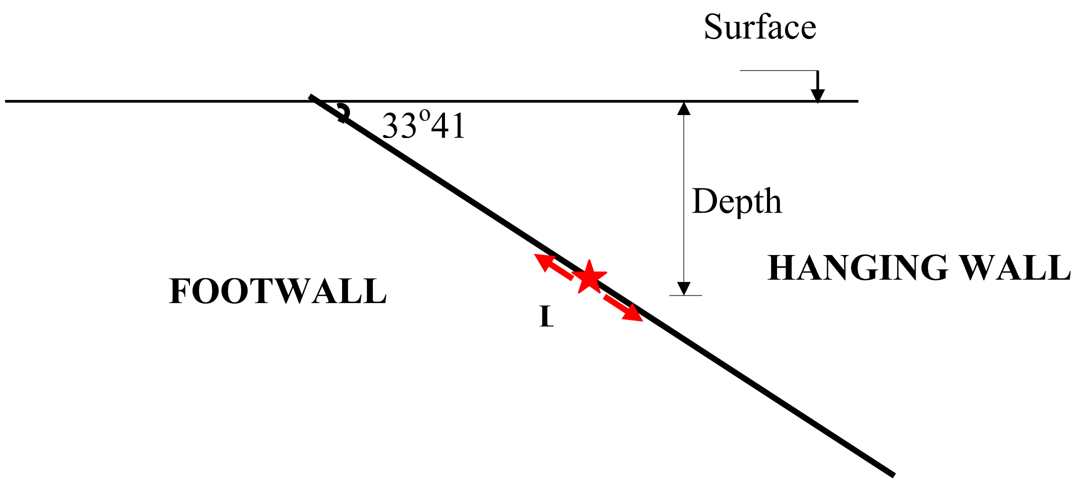

Figure 6.2. Fault model used for the dynamic simulation of the rupture process of a dipping fault that breaks the free-surface

The fault models are constructed taking into account the two sides of the fault. We assume that the fault has a thickness equivalent to the size of one cubic cell. Once the fault breaks, the linkage between the two surfaces of the fault is broken. The models used for the simulation (Figure 6.2) include a pre-existing fault 100 km wide in a solid of 130km x 40km. The cubic cells of the DEM have 0.25 km long sides.

For all the models the stress drop keeps constant ($\Delta\tau$=10MPa). The strength excess is represented by the parameter S (S=Strength excess/stress drop).

$$S = \frac{\tau_u - \tau_0}{\tau_0 - \tau_f} \tag{6.1}$$

First the shear fracture energy G given by the equation

$$G = \frac{1}{2}(\tau_u - \tau_f)D_c \tag{6.2}$$

is kept constant with G=1x10^{7}J/m^2.

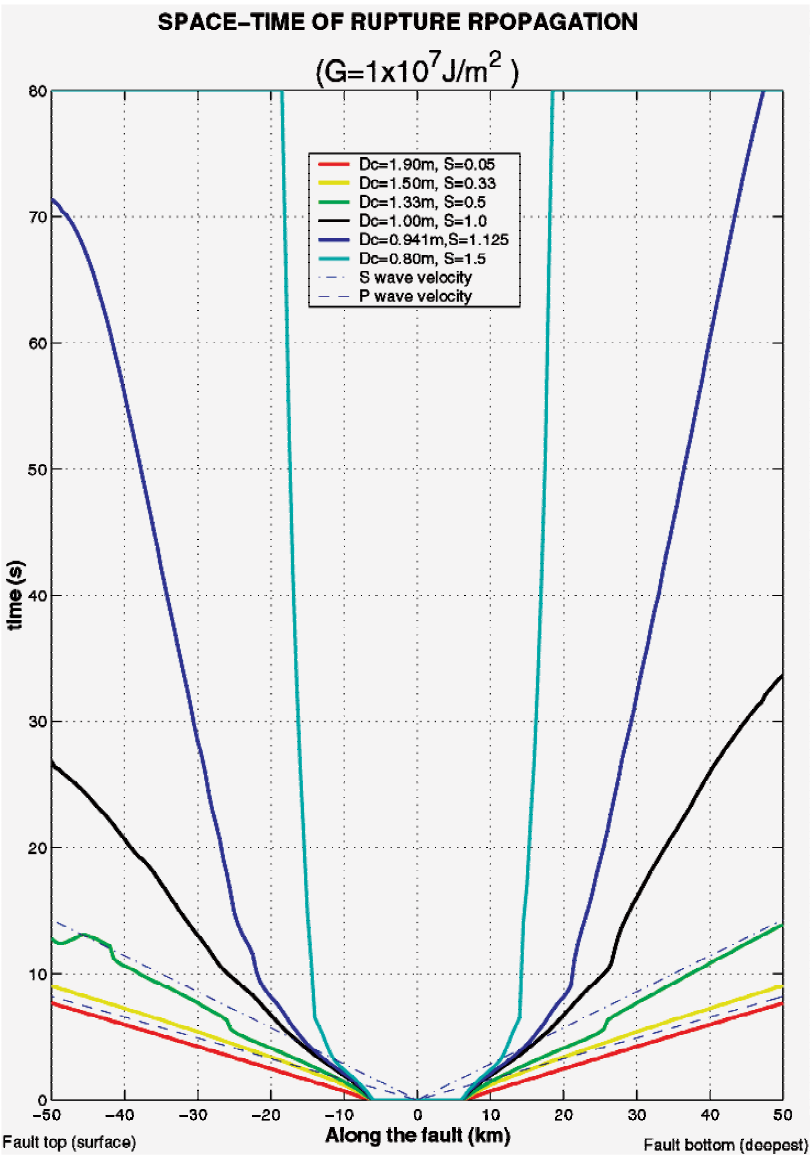

Figure 6.3. Space-time of rupture propagation for different combinations of D_c and the parameter S, keeping constant the fracture energy G=1x10^{7}J/m^2.

Fig 6.3 shows the space-time of rupture propagation for different combinations of D_c and the parameter *S*. The model with the highest rupture velocity (supersonic velocity) correspond to the model with D_c=1.90 and *S*=0.05. The model with the lowest rupture velocity correspond to the model with D_c=0.8 and *S*=1.5. The rupture velocity increases as *S* decreases and D_c increases. The model with D_c=1.33 and *S*=0.5 (green line in the Fig. 6.3) calls the attention because the rupture process of this model shows more irregular progress of the rupture near the free surface than the others models. In order to understand why the irregularity of this model, the shear stress changing in space and time is shown in Fig. 6.4. Fig. 6.4a shows the space-time of the shear stress during the rupture and Fig. 6.4b shows the shear stress on the fault for different times. As observed in Fig. 6.4b, there are two permanent peaks of shear stress close each other during almost all the rupture process. The first peak corresponds to the main rupture front. The secondary peak is originated from the stress peak associated with the S wave velocity that propagates ahead of the mean rupture front. When this secondary stress peak reaches a critical value the fault break forming a secondary rupture front. These two ruptures front join in somewhere in the fault forming again one rupture front, but because the rupture velocity never overcomes the S wave velocity, the process repeats again. This suggests that the irregularity in the rupture process of this model is because the permanent creation of the two rupture fronts. When this mechanism approaches the free surface, the stress reflected from the free surface bumps the two rupture fronts (Fig. 6.4a) and contaminates the rupture process, originating a complex rupture mechanism. The effects of this irregular rupture process on the ground motion are considerable, as observed in the Fig. 6.5, where the peak velocity on the free-surface is shown. The model with irregular rupture process (green line) shows higher values in the vertical component even than the model with supersonic velocities in which they are expected to have the highest values. In the horizontal component the values are similar to the model with supersonic velocity, specially in the hanging wall. The models with subsonic velocity always show the lowest values.

The results suggest the existence of a critical rupture velocity that can generate the strongest ground motion near the source. For the set of models used above, the model that propagate with this critical rupture velocity has *Dc*=1.33 and *S*=0.5, model with green line in Fig. 6.3, and 6.5

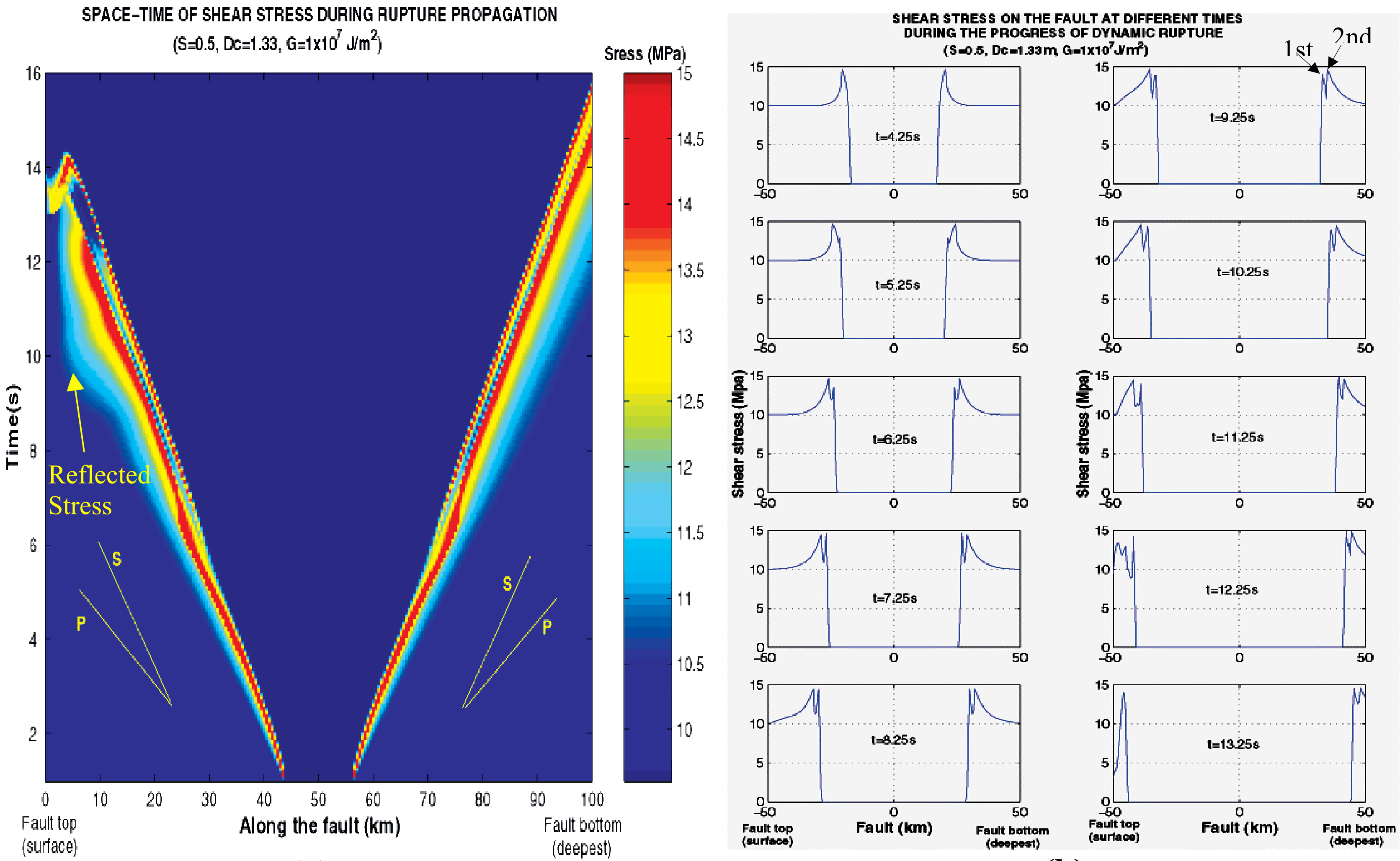

(a) (b)

Figure 6.4. Shear stress changing in space and time during the progress of the dynamic rupture. (a) Space-time of the shear stress during the rupture; (b) Shear stress as a function of position along the fault for different times.

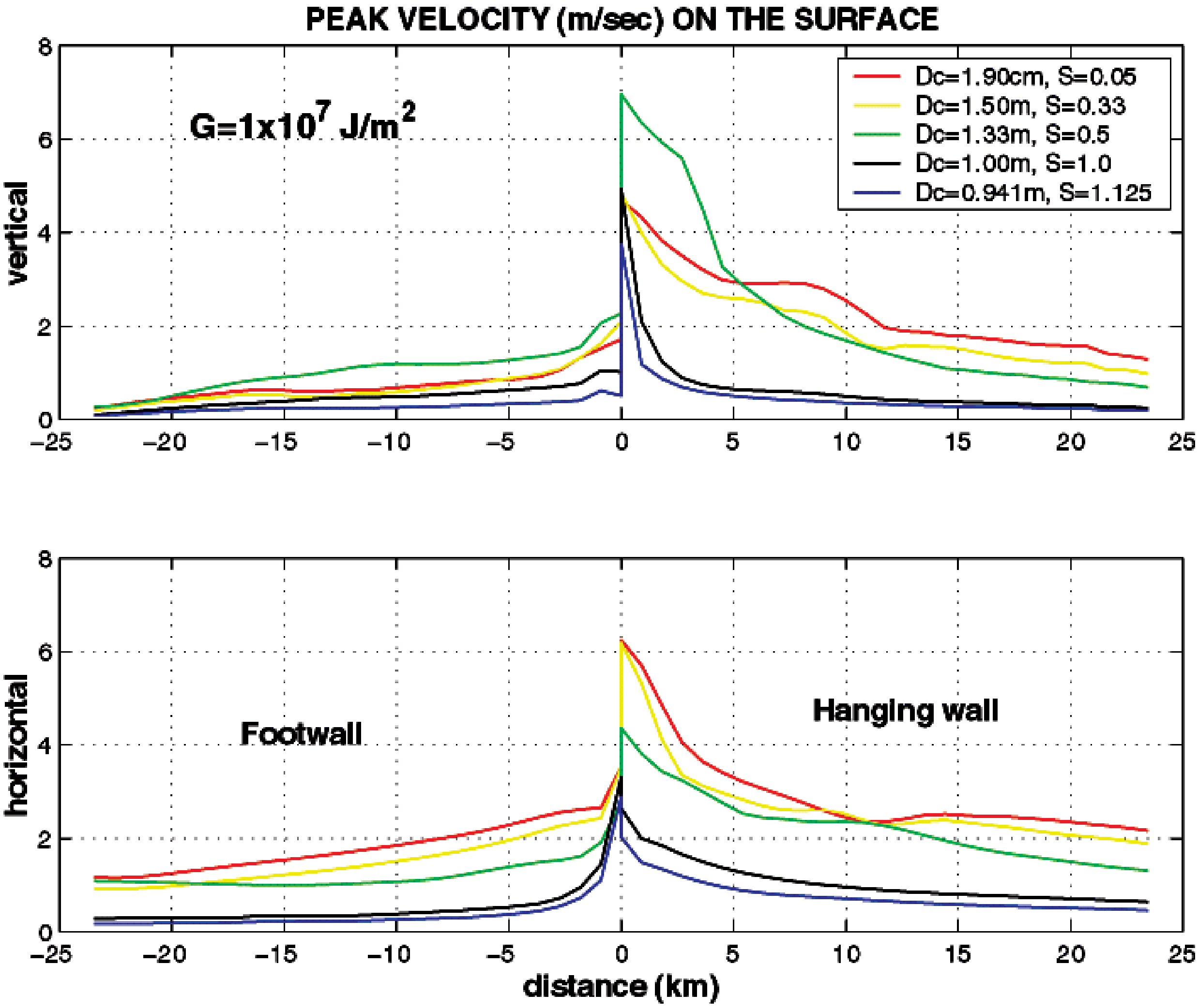

Figure 6.5. Comparison of the peak velocity on the surface between the models with different combinations of D_c and the parameter S, keeping constant the fracture energy $G=1x10^7 J/m^2$.

Now lets look for more critical models keeping the parameter S=0.5 constant. Fig. 6.6a shows the space-time of rupture propagation for different combinations of D_c and shear fracture energy G. The model with the smallest D_c values shows supersonic rupture propagation (red and yellow line), and the others models (red, black an green line) propagate with a rupture velocity around the 95% of the S wave velocity. These last three models show the same irregularity of rupture process analyzed before. Now lets observe again the effects on the ground motion. Fig. 6.6b shows the peak velocity on the free-surface for the models with S=0.5. As observed before, the models that have irregular rupture process present the highest values of peak velocity, even higher that the models with supersonic velocity. From these results the critical rupture velocity seems to be around 95% of the S wave velocity.

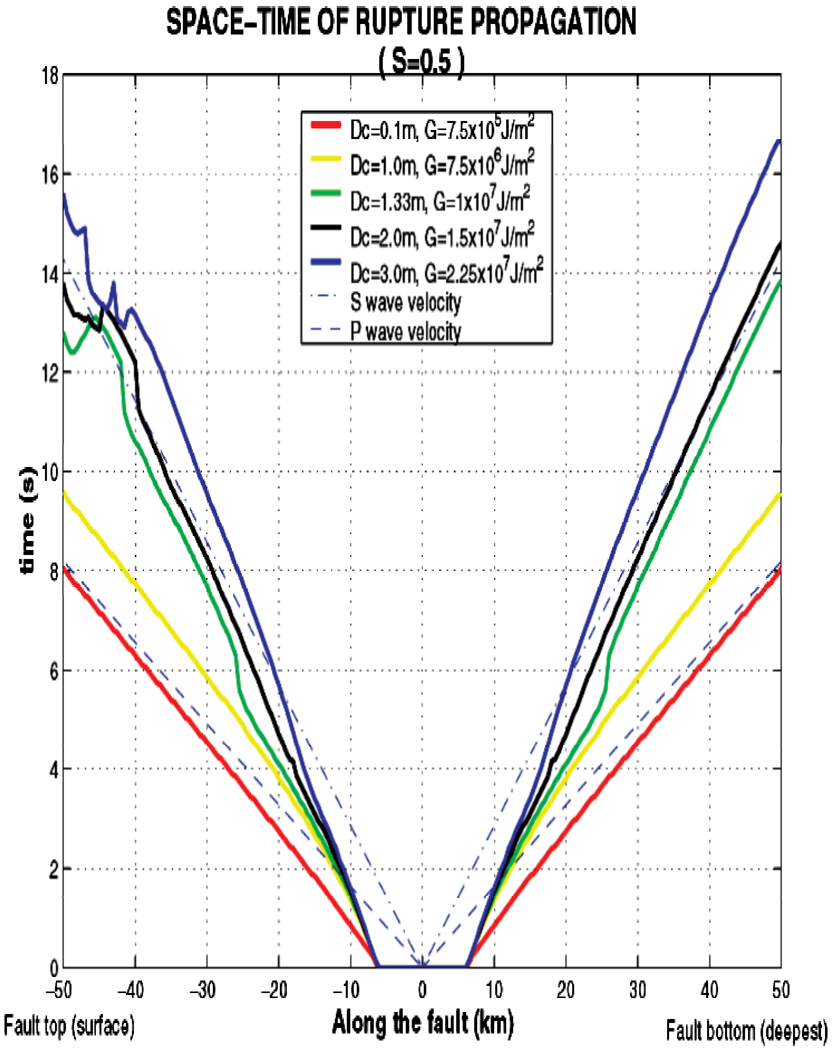

(a)

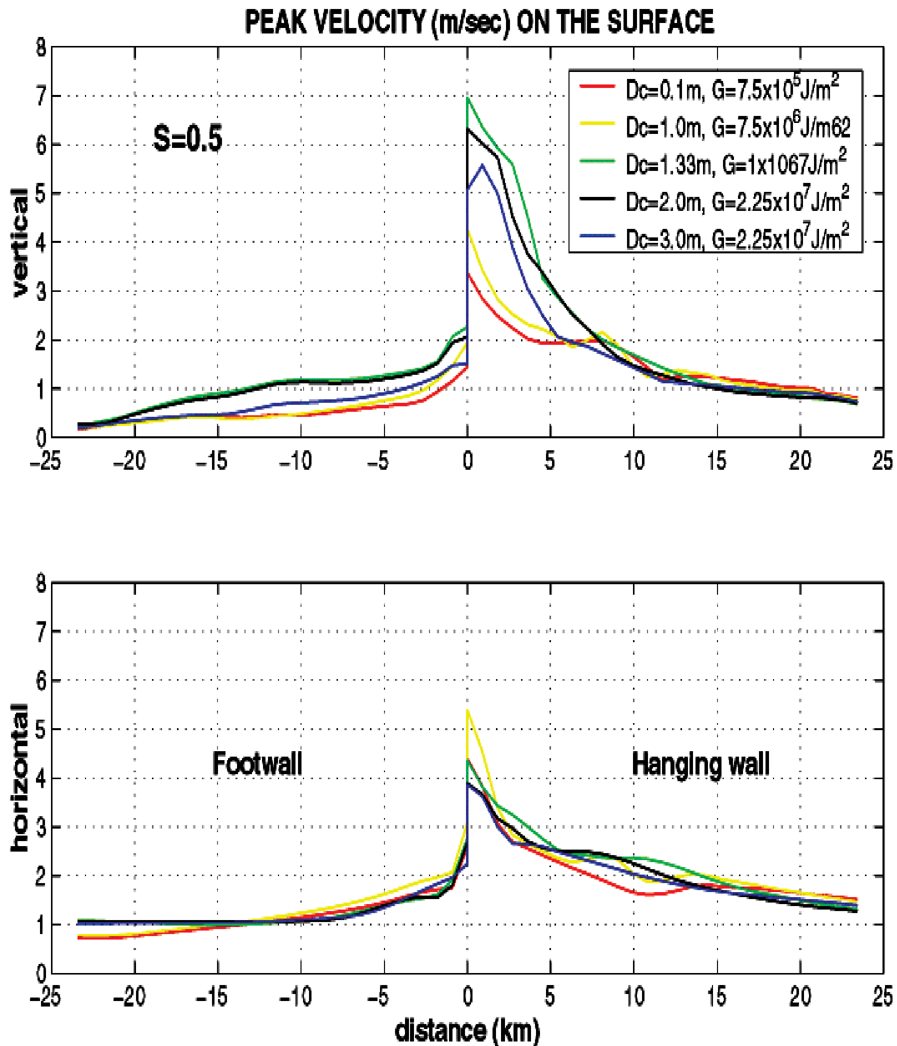

(b)

Figure 6.6. (a) Space-time of rupture propagation and (b) peak velocity on the surface for the models with different combinations of D_c and fracture energy G keeping constant the parameter S =0.5

The results suggest that the near source ground motion generated from the rupture process of dipping faults that break the free surface is strongly affected by the rupture velocity, that is, by the combination of the strength excess and critical slip. In general, higher rupture velocity produces stronger ground motion than slower rupture velocity. But when the rupture process reaches the critical rupture velocity (around 0.95*Vs*) the rupture becomes complex and the general expectation breaks, that is, the rupture in stage generates higher peak ground velocity than any others models, even than models with supersonic rupture velocity.

In order to observe if the effect of the rupture process on the ground motion described above affect also to faulting when the rupture do not break the free surface, we developed the same models keeping constant the shear fracture energy *G,* but now the rupture is forced to stop 3 km before reaches the surface. The peak ground velocity shown in Fig. 6.7 show similar characteristics compared to the models that break the free surface (Fig. 6.5). Therefore, the effects of the critical rupture velocity on the ground motion are also important for the models that do not break the surface.

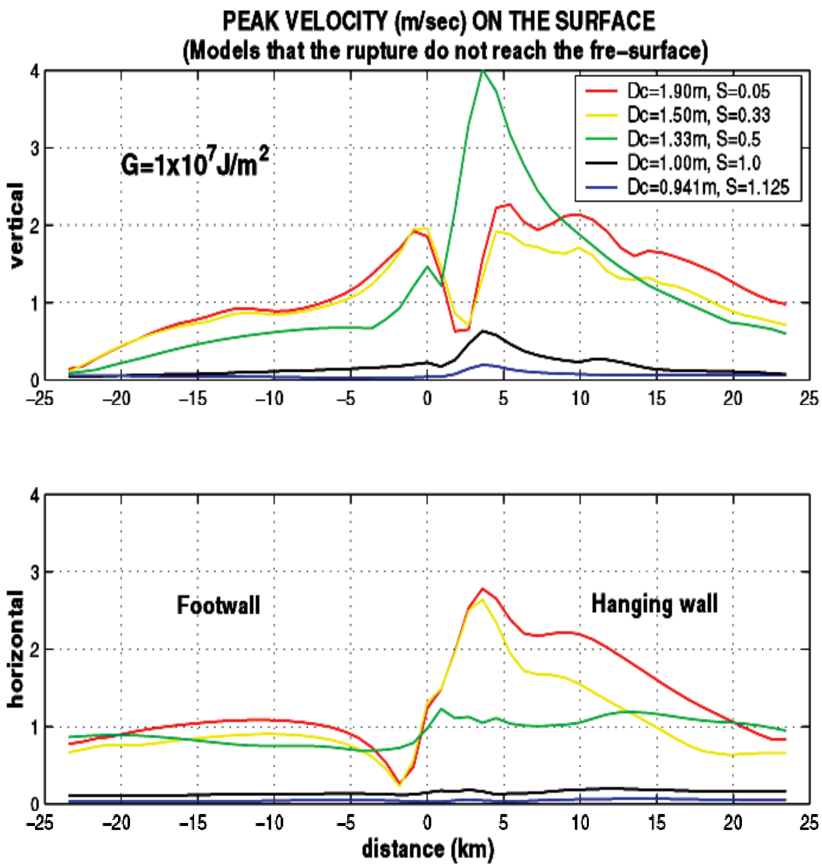

Figure 6.7. Comparison of the peak velocity on the surface between the models with different combinations of D_c and the parameter *S*, keeping constant the fracture energy G=1x10^{7}J/m^2, for the dynamic rupture process of dipping fault that do not reach the free-surface.

Finally we can conclude that the estimation of the parameters strength excess and critical slip is important to the analysis of the near source ground motion. From the results described above the rupture velocity strongly affects the near source ground motion, and the rupture velocity is highly dependent by the combination of the strength excess and critical slip, therefore, the right combination of this two parameters is important to for example explain some characteristics of the fault rupture, ground motion and damage pattern caused by a real earthquake.

6.2.2. Simulation of new tensile cracks during a 2D dynamic shear rupture propagation.

For the numerical tensile rupture simulation, it is assumed that the tensile stress concentrations resulting from the shear slip on the pre-existing fault cause the new cracks in mode I and propagates away from the pre-existing fault. Extension of a fracture will occur once the critical tensile fracture energy G_{Ic} has been reached or exceeded. The tensile fracture is governed by the constitutive relation tensile stress-strain formulated in the item 3.5. Steps include the formation of individual microcracks, propagation and linking of these cracks during the shear dynamic rupture process.

The spontaneous inplane rupture is analyzed in a plane strain condition. A pre-existing fault has a length L=85km. The fault movement is assumed to be right-lateral slip. The dynamic parameters for the shear slipping are constant along the fault and they are adopted as follow: the stress drop $\Delta\tau$=10MPa, Strength excess= 5.0MPa and Critical slip D_c=0.5m. The rupture propagates bilaterally from the center of the fault with the stress drop constant everywhere on the shear crack plane.

For the generation of the tensile cracks, it is assumed that the critical fracture energy in mode I G_{Ic}=5x10^{5}J/m^2 and a coefficient k_r=1.5 (the definition of these parameters are given in item 3.5).

A homogeneous medium with P wave velocity 6.1 km/sec, S wave velocity 3.5 km/sec and density 2700 kg/m^3 is assumed. It correspond to a Young's modulus 8.37 x 10^{10} N/m^2, Shear modulus 3.35 x 10^{10} N/m^2 and Poisson's ratio 0.25.

The generation of the tensile cracks for the 2D in-plane problem is shown in the snapshots every one second during 16 seconds as observed in Fig. 6.8. The tensile cracks expand with the shear rupture growth and propagate from the tip of the shear crack. A large number of cracks are mainly generated on the dilatation side, as expected. The dilatation and compression sides are specified by the positive sign (+) and negative sign (-) respectively as shown in the right inferior figure of Fig. 6.8. The length of the new cracks is increasing gradually from the origin (hypocenter) to the end of the fault. It could be observed that at the end of the pre-existing fault the tensile cracks are extending for largest distant forming branches of cracks. The final stage of the formation of the cracks is consistent with that observed in laboratory (e.g. Petit and Barquins, 1988) as well as the field observations (e.g. Vermilye and Scholz, 1998).

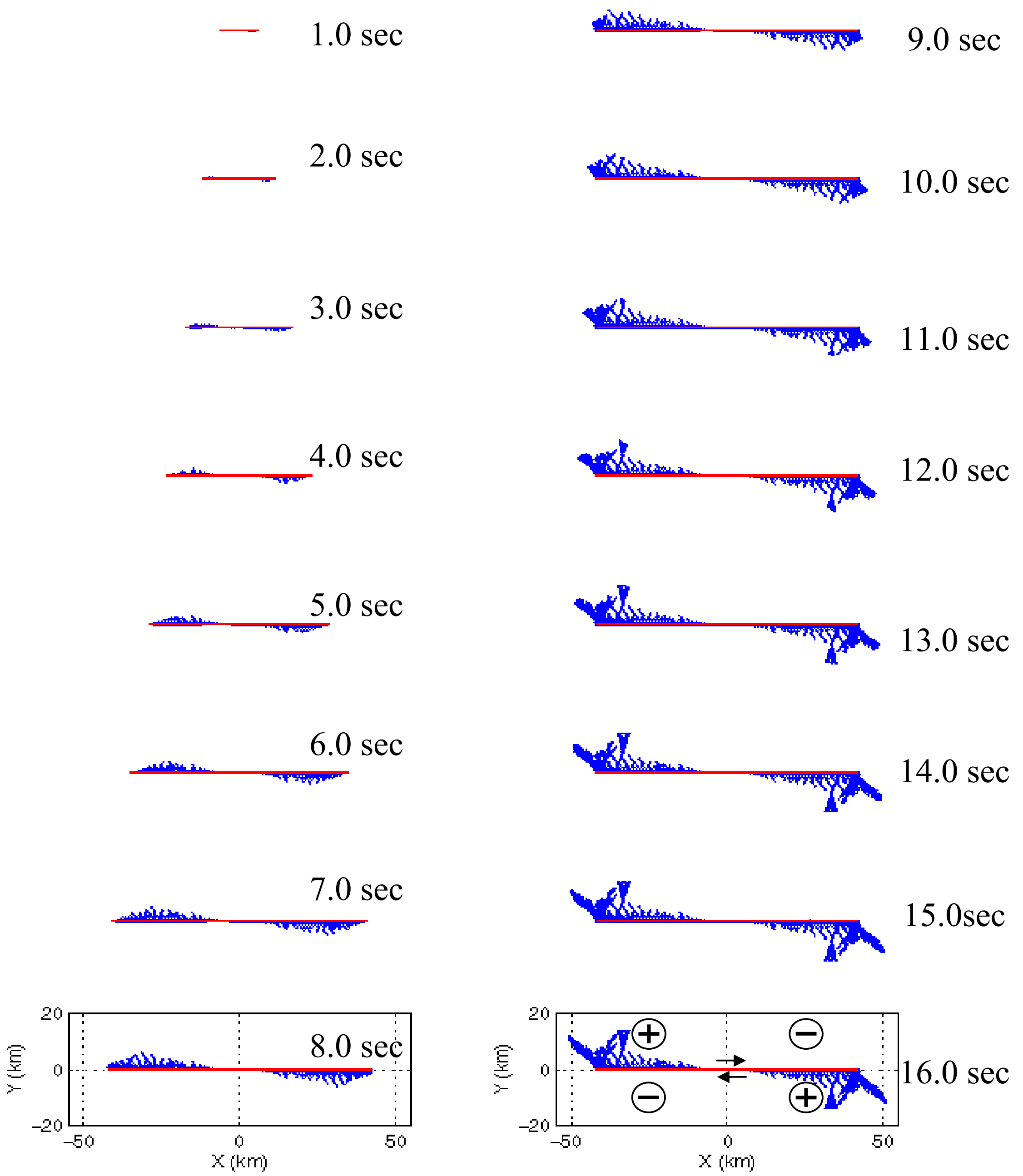

Figure 6.8. Snapshots (1 to 16 sec) of the shear rupture progress and generation of tensile cracks. The horizontal straight solid line is the shear crack and the irregular lines that leave the straight line are the tensile cracks. The signs (+) and (-) means dilatation and compression sides respectively.

Chapter 7

Application of the Model in 3D

7.1 Dynamic Rupture and Near Source Ground Motion Simulation of a Vertical Shallow Strike Slip Fault

The numerical shear rupture simulation is obtained for the near-field elastodynamic motion coupled to frictional sliding on a pre-existing fault. Initially the stress distribution along the fault is at the initial stress level, the rupture is initiated artificially by imposing a stress drop in a limited small region, which leads to initial stresses along the fault that increase monotonically without any relative slipping along the fault. Eventually, the interface shear stress (τ) at a point exceeds the local shear strength (critical stress level τ_u) and slip at a node occurs, governed by the slip weakening model shown in Figure (3.5) and represented by equation (3.13). Considering that the seismic radiation and slip depend only on the stress change (stress drop) during the earthquake, and not on the absolute stress, we assume that the initial stress (τ_o) along the fault is at its zero level. Therefore, the necessary parameters required to simulate the rupture process governed by the slip weakening friction model are the strength excess, stress drop and critical slip.

For the simulation, an idealistic pre-existing fault, in which shear rupture propagation occurs, is embedded at a depth of 3km from the free-surface. For analyzing a more realistic earthquake source, a fault with an asperity embedded in a stratified medium and located 1.5km from the top of the pre-existing fault is used. We call this model as asperity model. The parameters used for the 3D dynamic simulation and the geometry of the asperity fault model are shown in Fig.

7.1. We assume that an asperity is a zone with higher stress drop than surrounding areas. The dynamic parameters for the shear slipping are as follow: for the asperity area we assume stress drop $\Delta\tau$=18MPa, Strength excess= 3.0MPa and Critical slip D_c=0.5m; and surrounding the asperity, stress drop $\Delta\tau$=2.5MPa, Strength excess= 3.0MPa and Critical slip D_c=0.15m. The velocity structure of the medium is shown in Table 7.1. The fault movement is assumed to be right-lateral slip. The model used for the simulation is a solid of 60km x 60km x 40km. The side of the cubic cells is 0.5 km long.

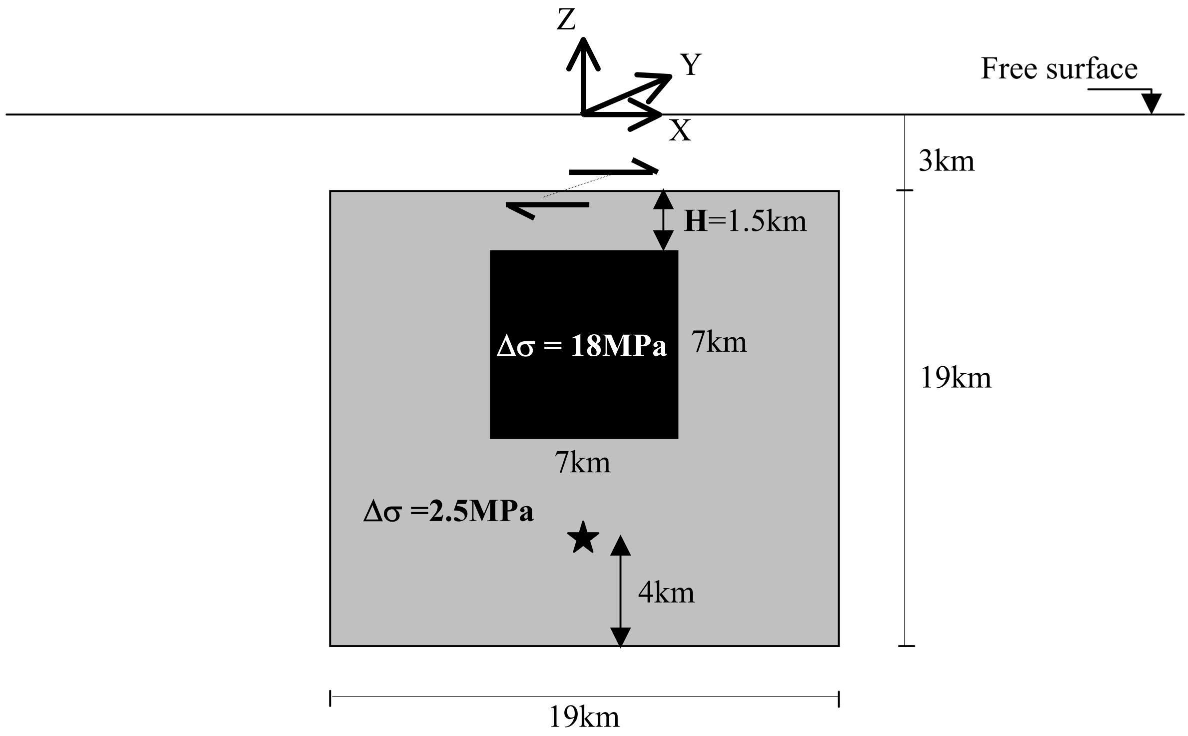

Figure 7.1 Fault model and parameters distribution used for the 3D dynamic simulation (asperity model)

Table 7.1. Velocity structure for the asperity model

Depth (km)	Vp (km/s)	Vs (km/s)	ρ (kg/m^3)
0 - 2.5	4.5	2.6	2400
2.5 - 20	6.0	3.5	2700
20 - ~	6.7	3.9	2800

The results of the shear rupture simulation are presented in snapshots of the slip and slip velocity every one second during 9 seconds as shown in Fig. 7.2 and Fig. 7.3 respectively. From these figures we can observe that the rupture grows faster in the in-plane direction, which is dominated by mode II. The rupture crosses the asperity from the bottom to the top. Around 4 to 5 sec the rupture reaches the asperity. From this stage the slip and slip velocity increase considerably because the higher stress drop in the asperity area. The largest values of the slip are concentrated in the middle of the asperity (Fig. 7.2). In Fig. 7.3 we can observe that during the rupture process the slip velocity has its peak value in the rupture front. When the rupture is in the bottom of the asperity (around 4s) the slip velocity starts to has higher values and gradually increase while the rupture cross the asperity. The maximum values are reached around 6 second when the rupture is in the top of the asperity. The general characteristics of these results are consistent with the theoretical 3D models presented in chapter 4, item 4.2.

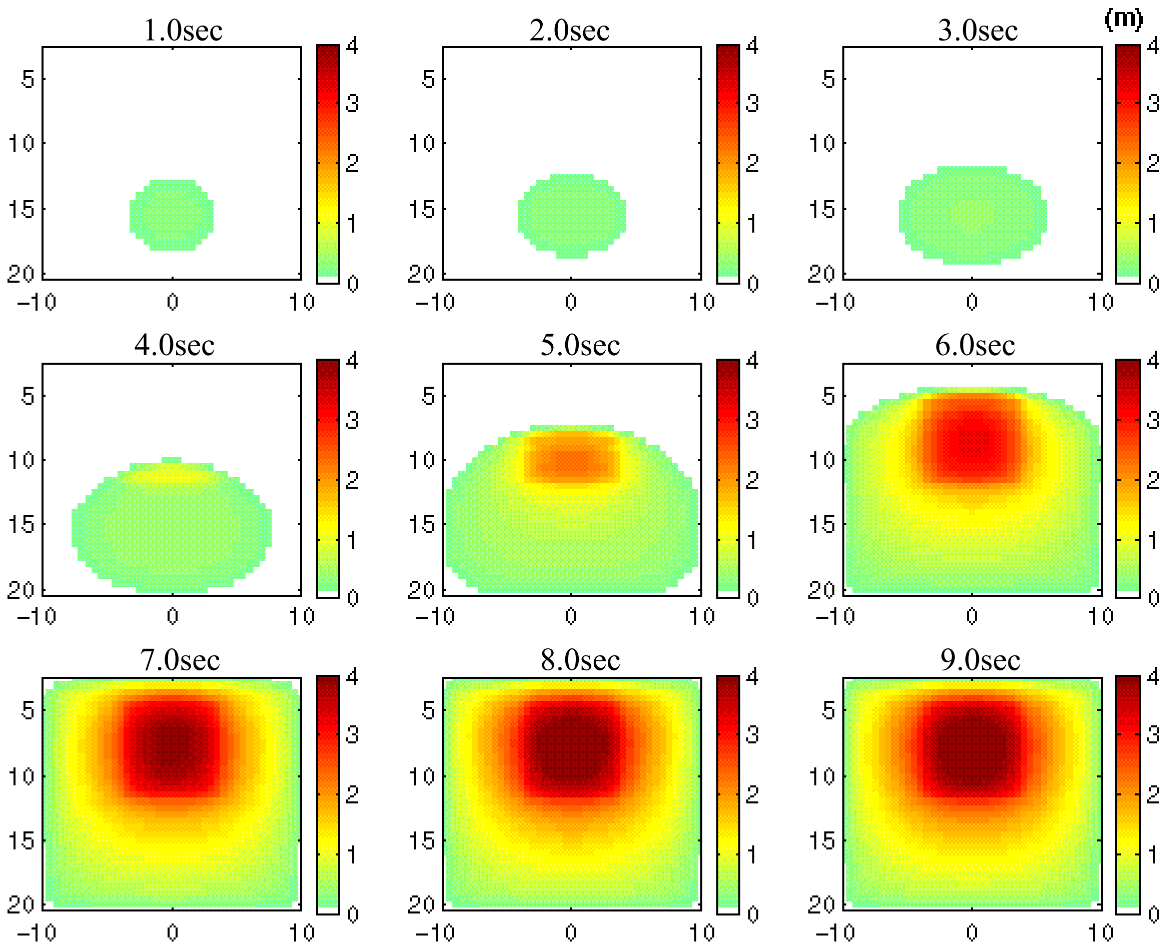

Figure 7.2. Snapshots of the slip for the spontaneous shear rupture of the asperity model with asperity embedded *H*=1.5km from the top of the pre-existing fault (fig. 4.1). The time for each snapshot is shown on each picture.

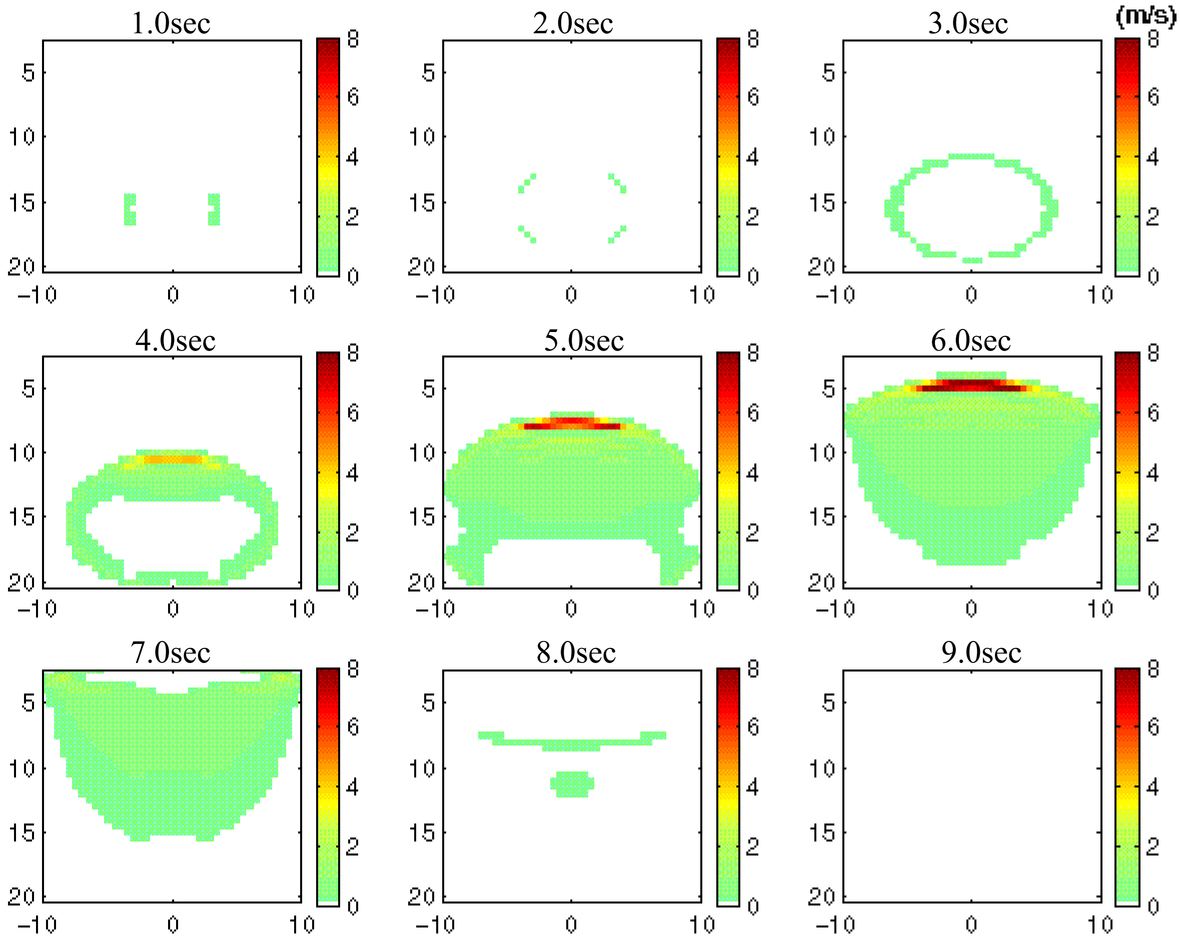

Figure 7.3. Snapshots of the slip velocity for the spontaneous shear rupture of the asperity model with asperity embedded H=1.5km from the top of the pre-existing fault (fig. 4.1). The time for each snapshot is shown on each picture.

The horizontal and vertical ground motion on the surface caused by the dynamic rupture process is also calculated. Fig. 7.4 and Fig. 7.5 show the maximum of the displacements and velocity ground motion respectively. Note that the finite dimensions of the fault produce complex pattern of displacement and velocity at the ends of the fault. This pattern of ground motion is consistent with theoretical results caused by shallow vertical strike-slip faults (e.g. Lay and Wallace, 1995)

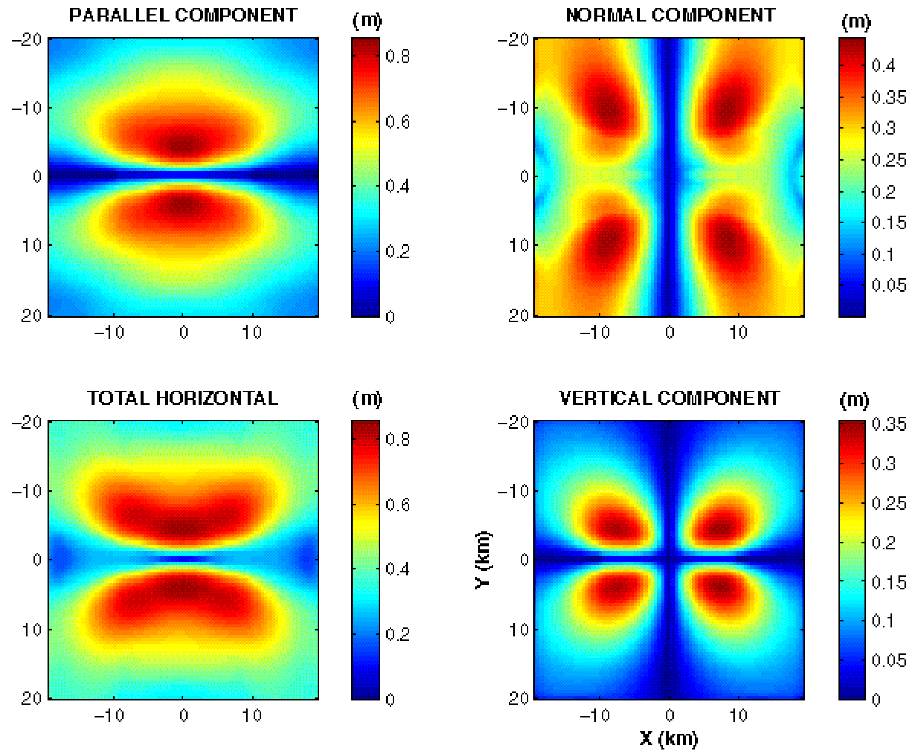

Figure 7.4. Maximum displacements ground motion on the surface caused by the dynamic spontaneous shear rupture of the asperity model with asperity embedded *H*=1.5km from the top of the pre-existing fault (fig. 4.1).

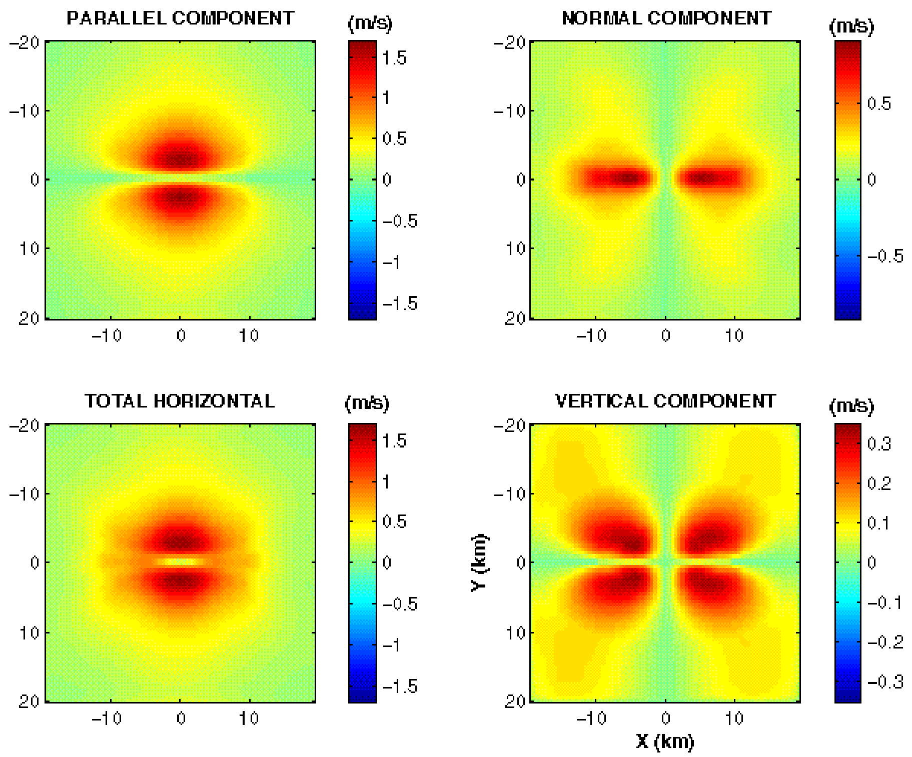

Figure 7.5. Peak velocity ground motion on the surface caused by the dynamic spontaneous shear rupture of the asperity model with asperity embedded *H*=1.5km from the top of the pre-existing fault (fig. 4.1).

7.2 The Effects of the Generation of Tensile Cracks During the Dynamic Shear Rupture on the Shear Slipping and Near Source Ground Motion.

As suggested before, shear rupture will propagate only along a weakness zone. In the present model, this zone is defined as a pre-existing fault, in which only shear slip, governed by a friction law, takes place. Additionally, the formation of tensile cracks during the shear rupture process is opened. The formulation is the same as explained for the problem in 2D (item 6.2.2), that is, for the numerical tensile rupture simulation, it is assumed that the tensile stress concentrations resulting from the shear slip on the pre-existing fault cause the new cracks in mode I and propagates away from the pre-existing fault. The mechanism of the tensile crack propagation is going to be governed by the low constitutive relation formulated in item 3.5,that is, extension of a fracture will occur once the critical tensile fracture energy G_{Ic} has been reached or exceeded.

Now, numerically we want to study how the shear slipping and near source ground motion are affected by the distribution of generated tensile cracks. For this purpose, the same fault model of the previous item is used (Fig. 7.1). For the generation of the tensile cracks, it is assumed that the critical fracture energy in mode I G_{Ic}=5x10^{5}J/m^2 and a coefficient k_r=1.5 (the definition of these parameters are given in item 3.5). The results of the simulation are described as follow:

In order to depict a general view of the total tensile cracks generated during the dynamic rupture process of the pre-existing fault, two perspective of the final stage of the cracks were drawn in Fig. 7.6. In Fig 7.6b it may be seen that the surface of the new cracks forms a flower structure on top of the fault and on the bottom of the asperity. But in the lateral sides of the fault and of the asperity, the cracks develop only in the dilatational side of the fault (Fig.7.6a). Fig. 7.6c shows a top view in which the cracks that reached the free-surface are observed. A detail explanation of the generation of the cracks will be presented in the next item.

The effects on the shear slipping are observed in the snapshots of the slip and slip velocity every one second during 12 seconds of Fig. 7.7 and Fig. 7.8 respectively. Comparing these results with that obtained in the previous model (free of tensile cracks), the maximum slip was almost duplicated and the slip velocity was extending approximately for more four second. As observed in Fig. 7.8, the slip velocity has similar characteristics until around 6 seconds, after that, from 7 to 11 second, there is some irregular slip, caused by the generation of the tensile cracks.

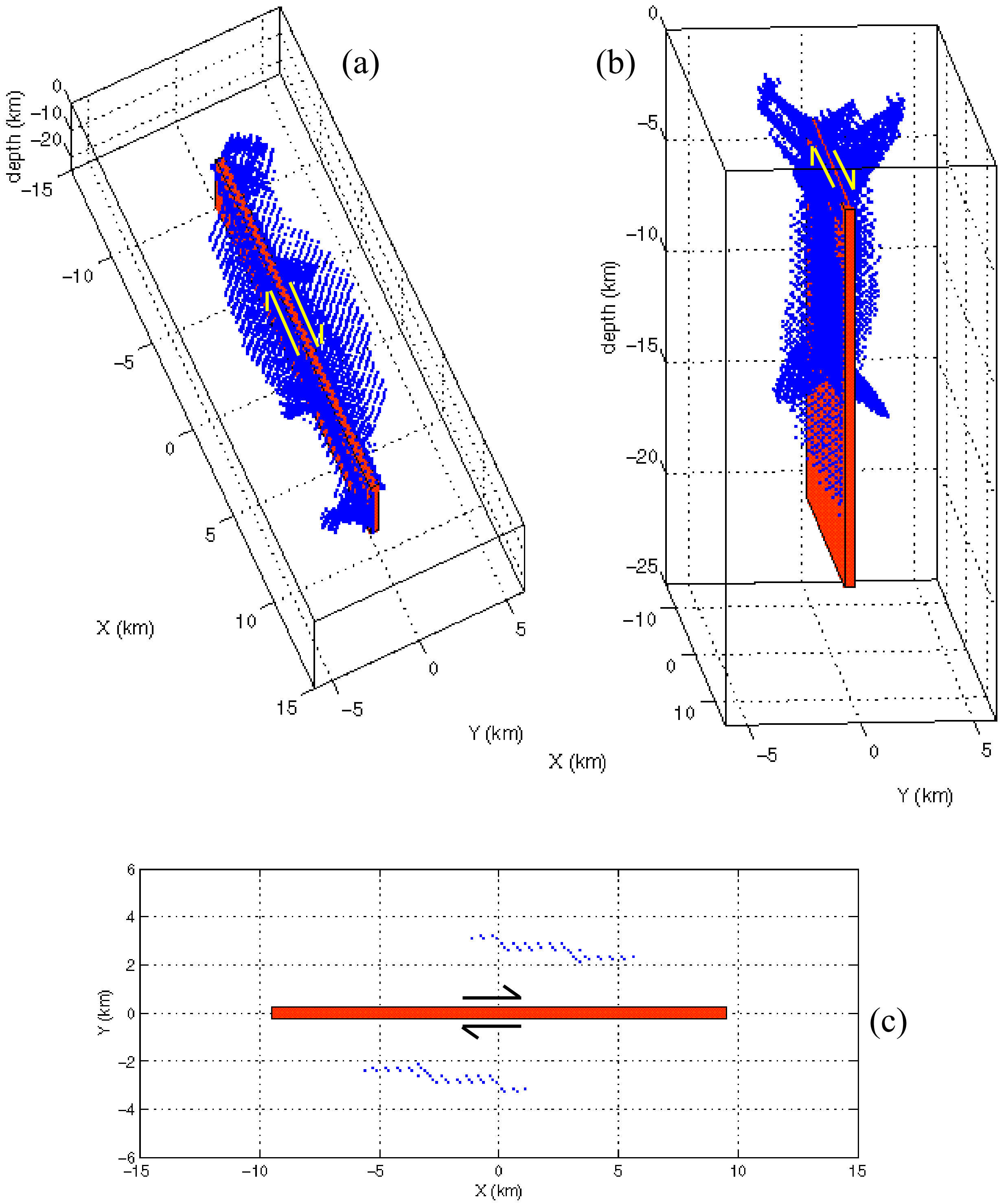

Figure 7.6. Three views of the final stage of cracks evolution for the model in which the asperit is embedded H=1.5km from the top of the pre-existing fault (fig. 4.1). The red color represents the shear crack along the pre-existing fault while the blue color represents the tensile cracks: (a) view of new surface cracks developed from the sides of the fault and asperity; (b) view of the new surface cracks that develop a flower pattern. (c) surface rupture.

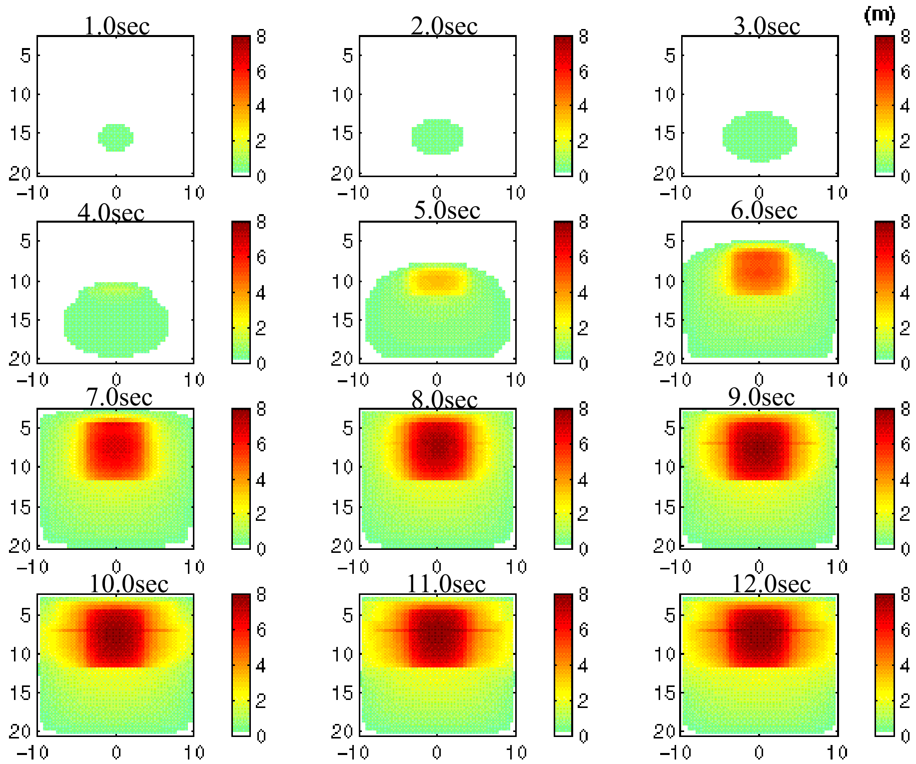

Figure 7.7. Snapshots of the shear slip for the model in which tensile cracks are generated. The asperity is embedded *H*=1.5km from the top of the pre-existing fault (see fig. 4.1). The time for each snapshot is shown on each picture.

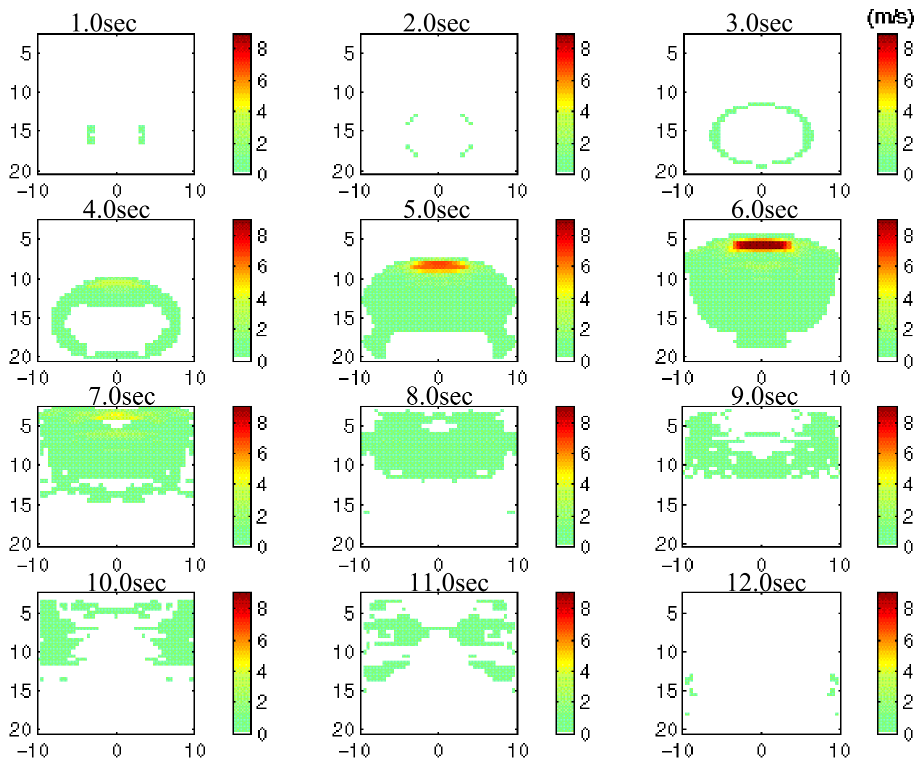

Figure 7.8. Snapshots of the shear slip velocity for the model in which tensile cracks are generated. The asperity is embedded *H*=1.5km from the top of the pre-existing fault (see fig. 4.1). The time for each snapshot is shown on each picture.

Now let see the effects on the near source ground motion. Fig. 7.9 and 7.10 show the maximum displacement and velocity ground motion on the free-surface respectively. The pattern of the ground motion suffers a drastic change, specially for the normal and vertical component. The cracks that reached the free-surface are the main responsible of this changing. The maximum values are concentrated along the rupture surface. The maximum displacements values of the normal and vertical components are almost duplicated, but the parallel component is almost the same (Fig.7.9). For the peak velocity values, the normal component also duplicate and the vertical component reach values almost four time the model free of cracks, but these maximums values are locally concentrated on the cracks that reached the free-surface. The parallel component keep almost the same values.

Finally we can conclude that the generation of tensile cracks strongly affects the rupture process of the fault and the near source ground motion.

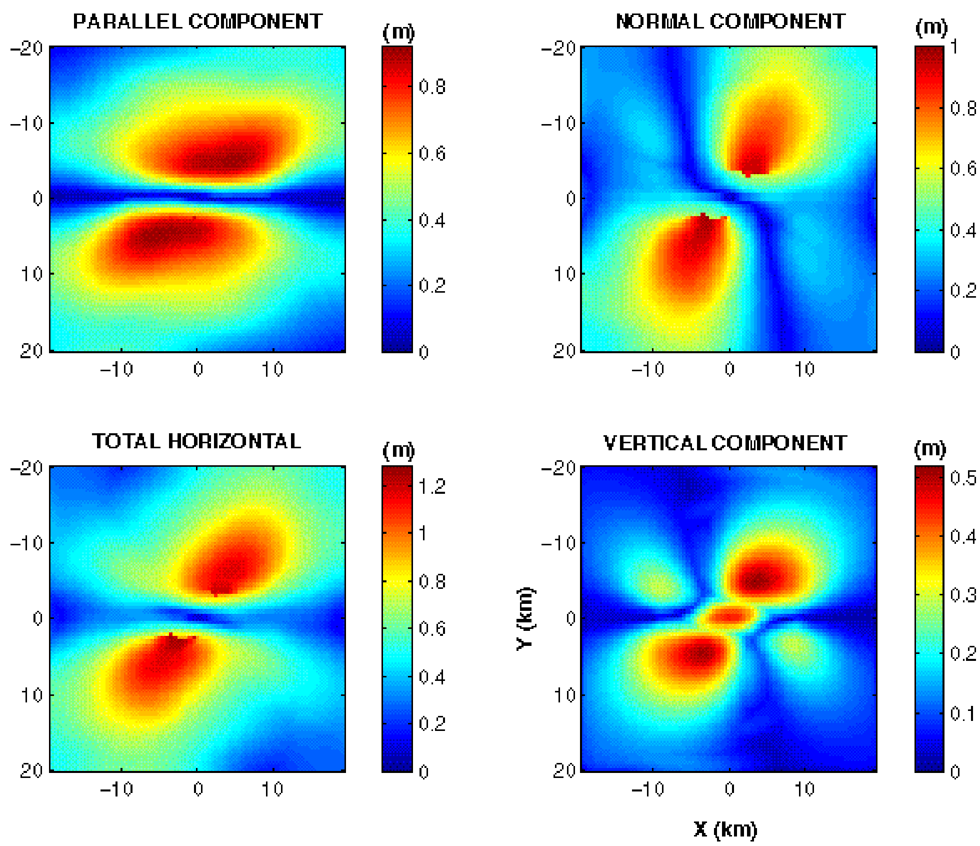

Figure 7.9. Maximum of the displacements ground motion on the surface caused by the dynamic spontaneous shear rupture for the model in which tensile cracks are generated. The asperity is embedded *H*=1.5km from the top of the pre-existing fault (see fig. 4.1).

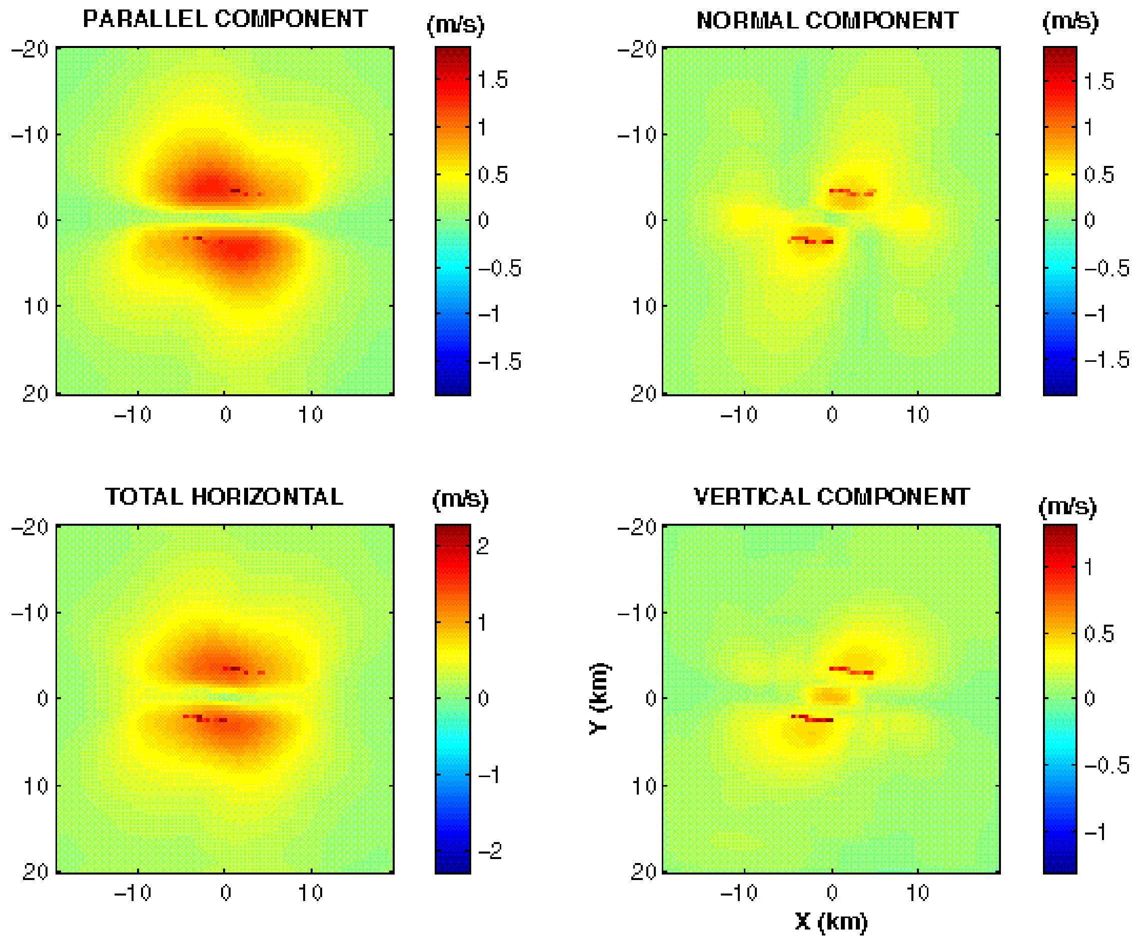

Figure 7.10. Peak velocity ground motion on the surface caused by the dynamic spontaneous shear rupture for the model in which tensile cracks are generated. The asperity is embedded H=1.5km from the top of the pre-existing fault (see fig. 4.1).

7.3 Generation of Tensile Cracks and how they Reach the Free-surface.

We want to investigate numerically the formation of new cracks and how they reach the free-surface during an earthquake in a 3D model of a vertical strike slip shallow fault. For this purpose we assume that the pre-existing fault, in which shear rupture propagation occurs, is embedded at a depth of 3km from the free-surface. The fault movement is assumed to be right-lateral slip.

Firstly, as shown in Fig. 7.11, a homogeneous fault model embedded in a homogeneous medium is used, that is, the dynamic parameters for the shear slipping are constant along the fault (stress drop $\Delta\tau$=7.5MPa, Strength excess= 2.0MPa and Critical slip D_c=0.2m). The medium is characterized by a set of P wave velocity 6.1 km/sec, S wave velocity 3.5 km/sec and density 2700 kg/m^3. This model is called "*homogeneous model*".

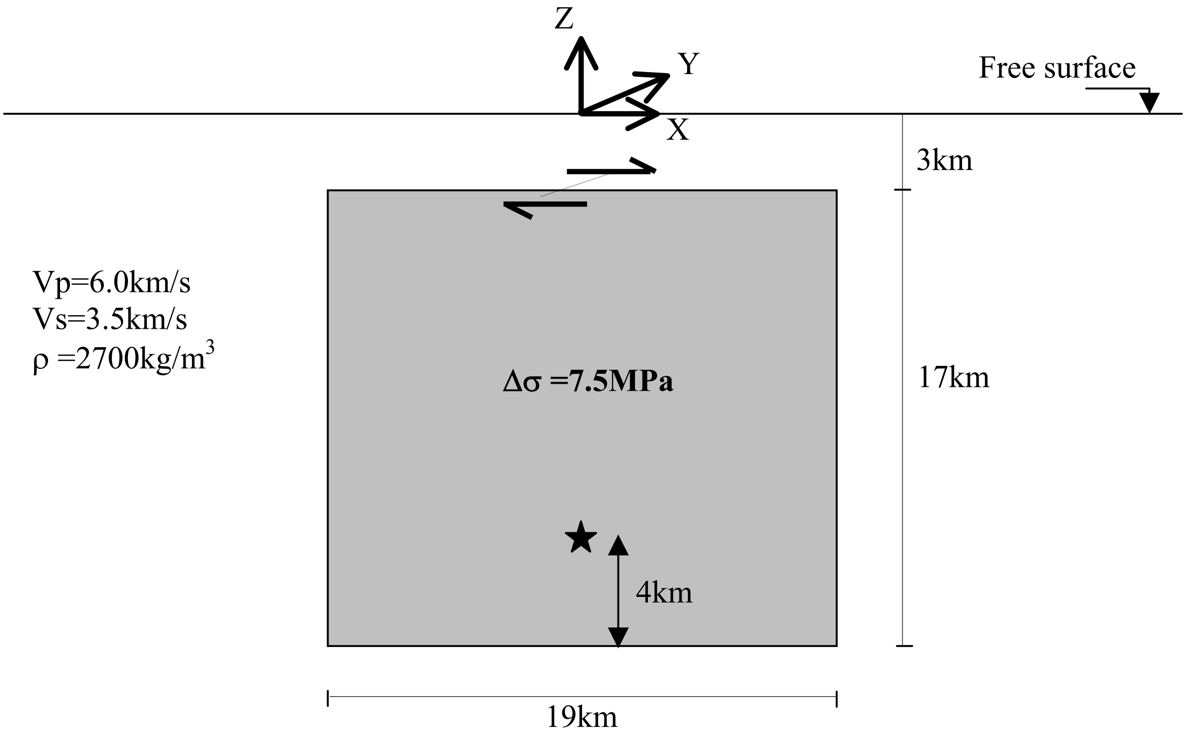

Figure 7.11 Homogeneous fault model and parameters distribution used for the 3D dynamic simulation.

For analyzing a more realistic earthquake source, a fault with an asperity embedded in a stratified medium is used, the geometry and the dynamic parameters of the fault model are the same as the model used in the item 7.1 (Fig. 7.1). The velocity structure of the medium is shown in Table 7.1. This model is called as "*asperity model*".

In order to study the effects of the asperity location on the propagation of new cracks, four cases with different asperity depth are simulated. In these models the distance H from the top boundary of the fault to the top boundary of the asperity area (Fig. 7.1) is taken as H=4.0km, H=3.0km, H=2.0km and H=1.5km respectively. The last model is the same analyzed in the item 7.2.

The results for the homogeneous model are shown in Figs. 7.12 to 7.14. Fig. 7.12 shows two views of the final stage of the new cracks. It may be seen that from the ends of the pre-existing fault new tensile cracks grew, forming very well defined new fractures, in a flower pattern structure.

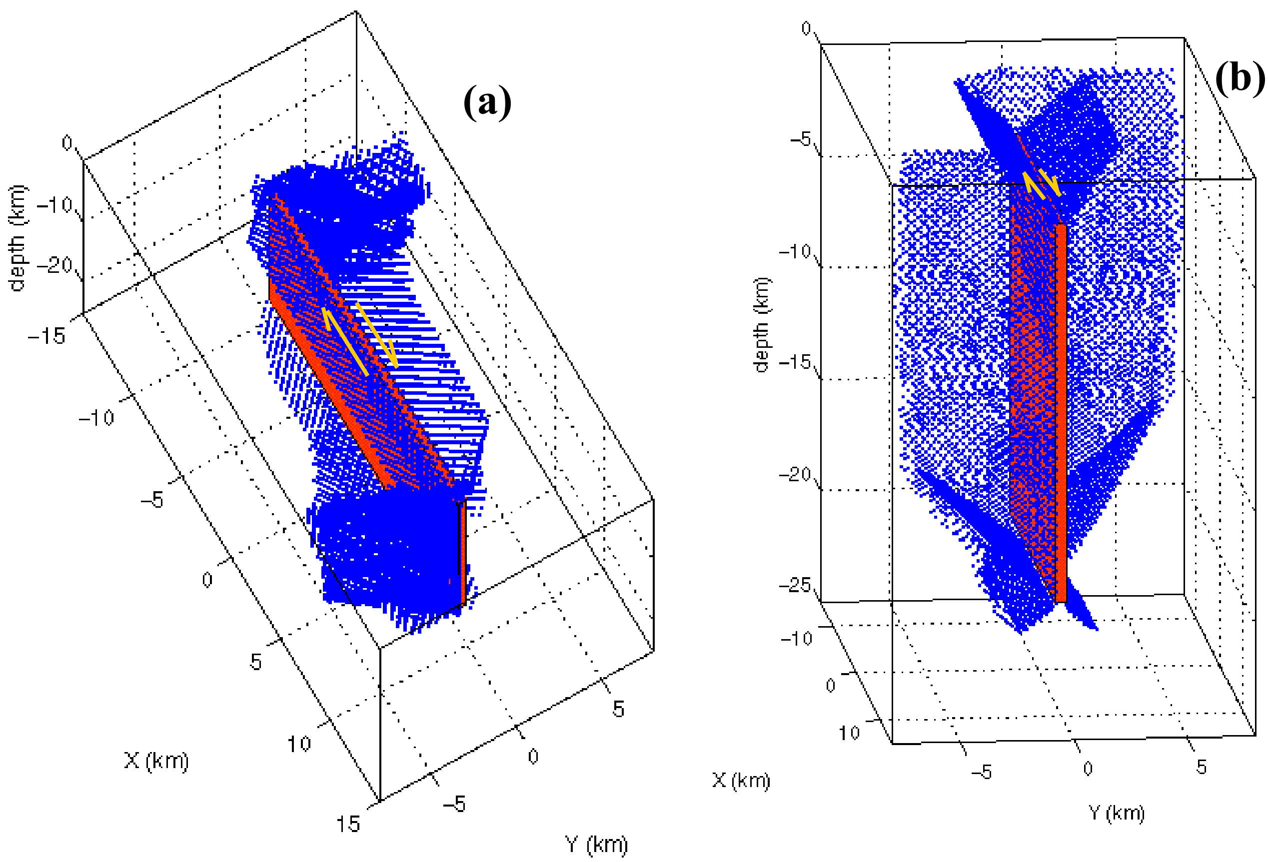

Figure 12. Two perspectives of the final stage of the cracks evolution for the homogeneous model. The red color represents the shear crack on the pre-existing fault and the blue color represents the tensile cracks: (a) view of the new surface cracks that grew from the sides of the fault; (b) view of the new surface cracks originated from the bottom and top boundaries of the fault that develop a flower structure

Figs 7.13a and 7.13c, present bird eye's views and an outline view of the fault, respectively, showing that the orientation of the new cracks across the pre-existing fault is asymmetric for the in-plane direction (mode II, Fig. 7.13a) and symmetric for the anti-plane (mode III, Fig. 7.13c). It is interesting to note, as shown in Fig. 7.12, that the pattern of new cracks (flower structure) formed from the top of the fault (near the free surface) is different from the pattern observed at the bottom. On the top of the fault, along the strike direction, two surfaces are generated symmetrically from the border of the two side of the fault forward the free-surface. On the other hand, from the bottom of the fault, four new surface are generated, two of them symmetrically from the border of the fault forward the depth; but the others two surfaces are generated asymmetrically ahead of the free-surface, that is, they generate only from one side of the fault in the tensile zone of the in-plane mode. These characteristics are clearly observed in the vertical cross section (VS1, VS2 and VS3) shown in Fig.7.14, the location of these sections is specified in Fig. 7.13a. The horizontal section (SH1) shown in Fig. 7.14 correspond to the middle of the fault as shown in Fig.7.13b and 7.13c, the cracks are developed on the dilatational side of the in-plane direction. The difference between the new cracks patterns generated at the top and the bottom of the fault may be attributed to the free-surface effects. The surface rupture is shown on the right-bottom side of Fig. 7.14, corresponding to the two surface cracks originated from the top of the fault. The location of the dilatation or tensile compression sides of the in-plane direction is specified in Fig. 5.

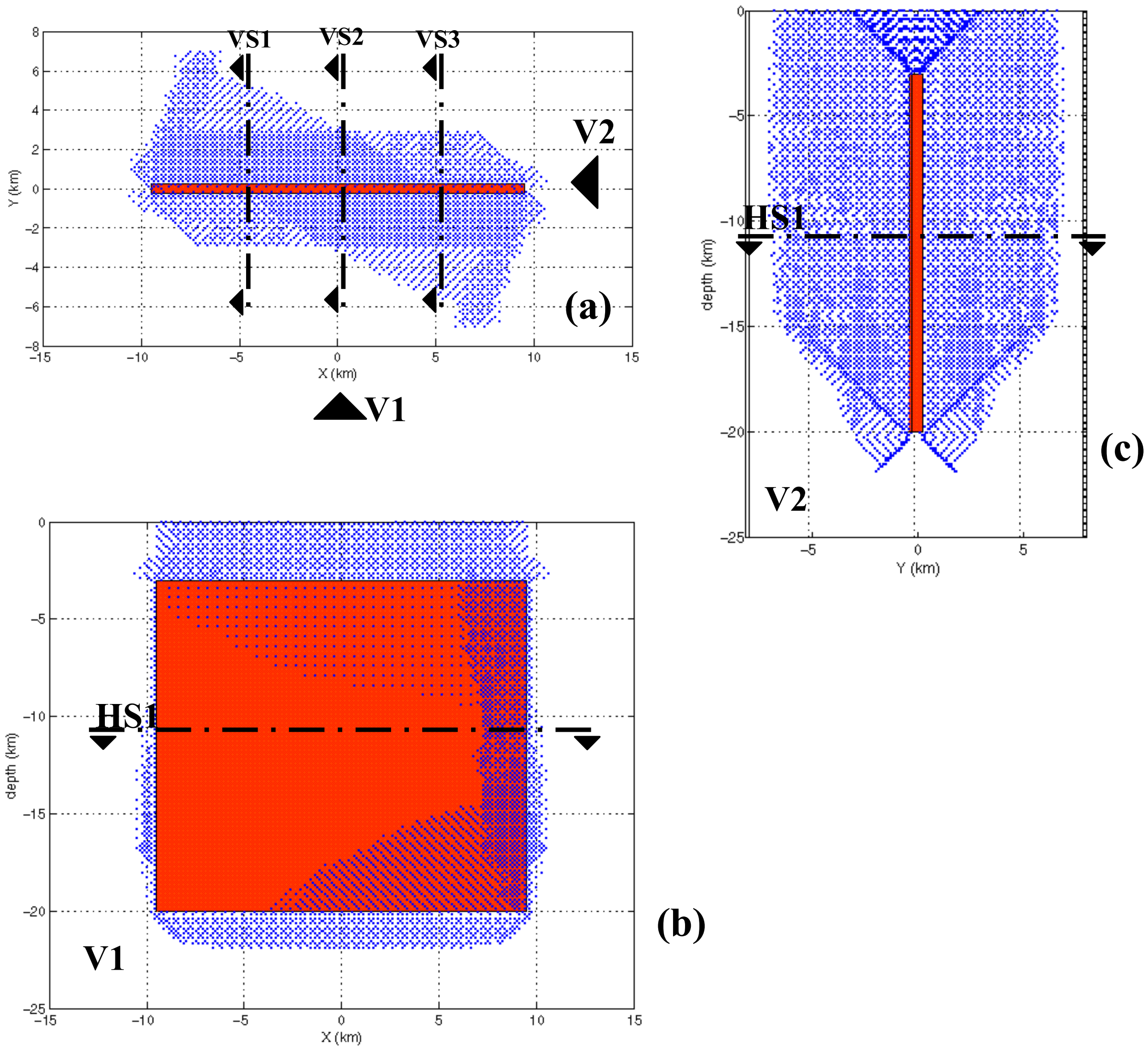

Figure 7.13. Views of the final stages of the cracks evolution for the homogeneous model: (a) Bird's eye view; (b) frontal view (V1); (c) outline view (V2)

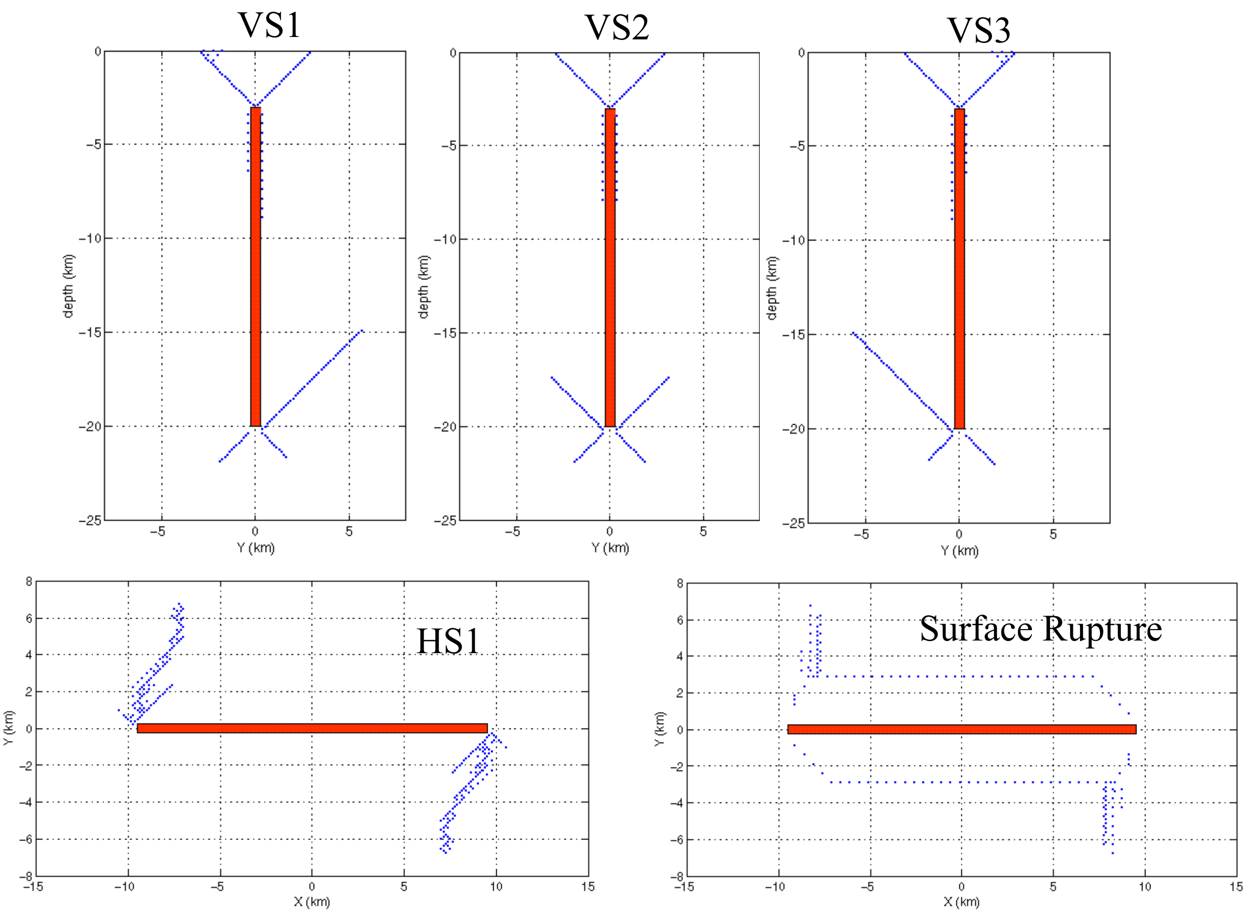

Figure 7.14. Vertical cross sections VS1, VS2, VS3, horizontal cross section HS1 and surface rupture of the final stages of cracks evolution for the homogeneous model. The location of the sections are specified in Fig. 7.13. The thick straight solid line is the shear crack and the irregular lines that leave the thick straight line are the tensile cracks.

The simulation of new cracks corresponding to the asperity model, for the four cases considered, is shown in Figs.7.15 to 7.20. The bird's eye view, frontal view and side view of the pre-existing fault are shown in Figs. 7.15 to 7.18 for the models with H=4km, H=3.0km, H=2.0km and H=1.5km, respectively. These figures show a general view of the cracks. As also observed in the homogeneous model, the cracks develop asymmetrically in the in-plane direction (mode II) and symmetrically in the anti-plane (mode III). The frontal view (Fig.7.15b to 7.18b) shows a concentration of cracks in the asperity zone. In general, all four cases present the same characteristics, that is, the cracks grow mainly from the borders of the asperity zone, and from the top and lateral sides of the fault. No significant cracking occurs along the lower edge, in contrast with results found for the homogeneous model. This may be due to the fact that the stress drop in the homogeneous model is larger than that in the surrounding area of the asperity.

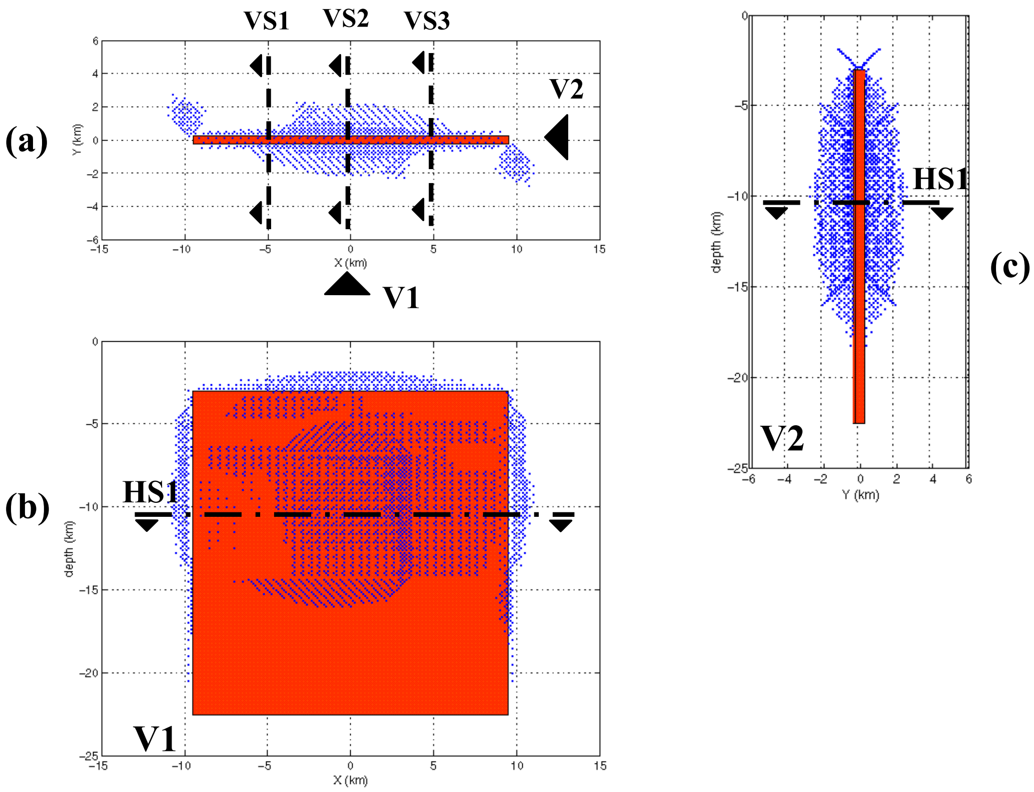

Figure 7.15. Views of the final stage of the cracks evolution for the asperity model with *H*=4.0km: (a) Bird's eye view; (b) frontal view (V1); (c) outline view (V2)

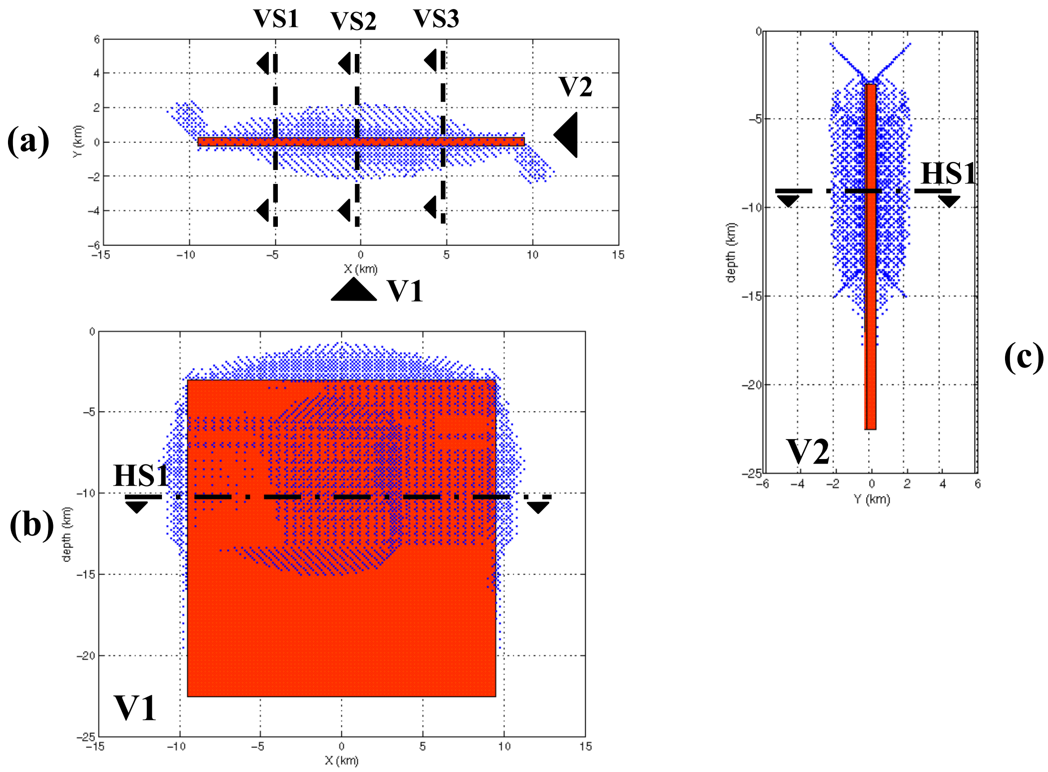

Figure 7.16. Views of the final stage of the cracks evolution for the asperity model with *H*=3.0km: (a) Bird's eye view; (b) frontal view (V1); (c) outline view (V2)

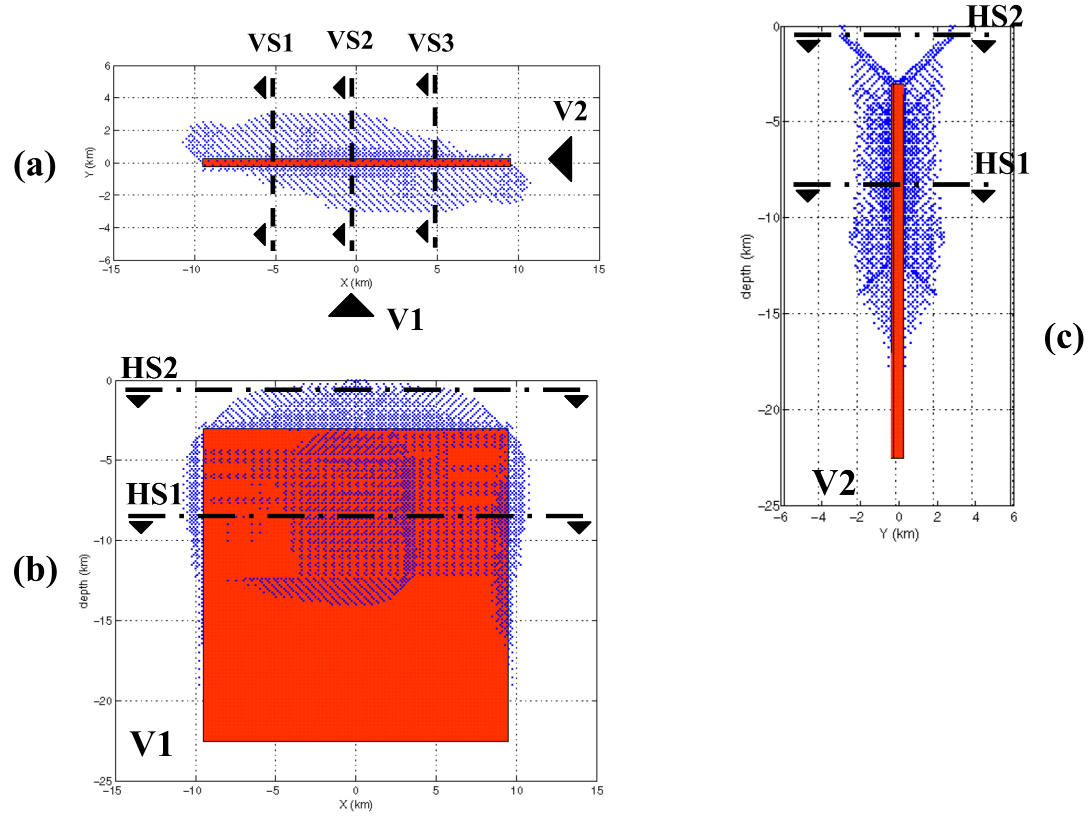

Figure 7.17. Views of the final stage of the cracks evolution for the asperity model with *H*=2.0km: (a) Bird's eye view; (b) frontal view (V1); (c) outline view (V2)

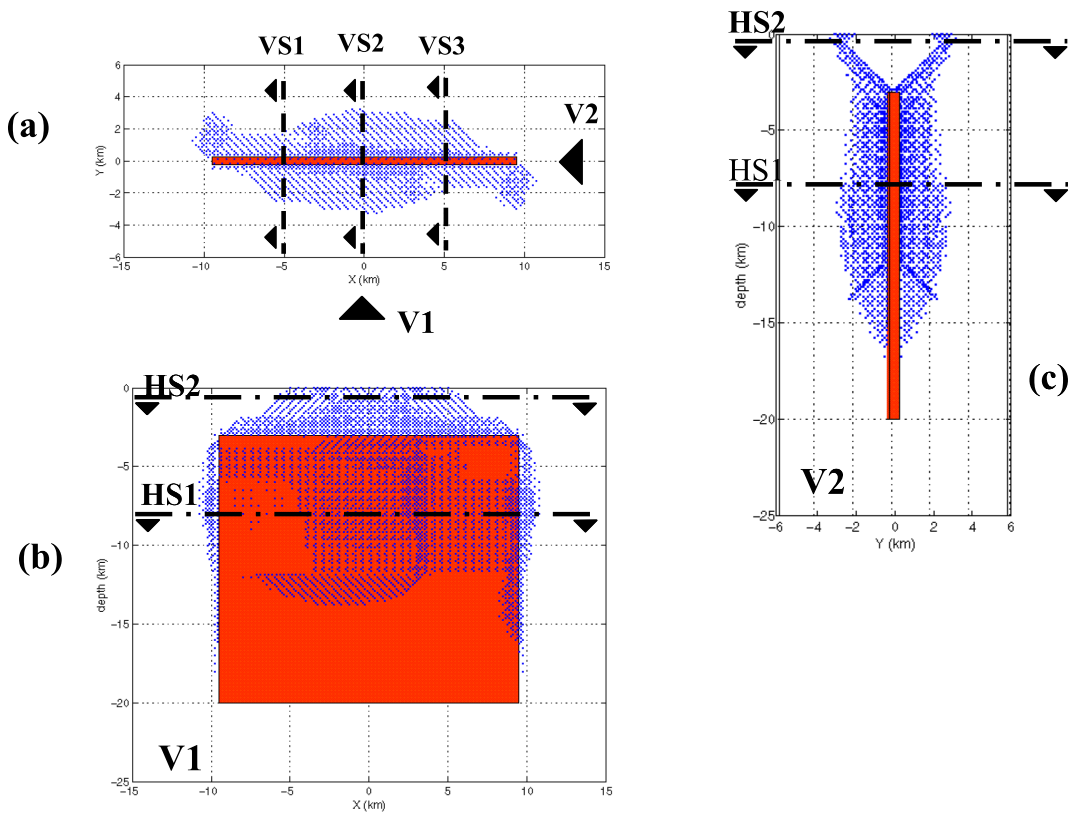

Figure 7.18. Views of the final stage of the cracks evolution for the asperity model with *H*=1.5km: (a) Bird's eye view; (b) frontal view (V1); (c) outline view (V2)

Fig. 7.19 shows the vertical cross sections VS1, VS2 and VS3 for the four cases. The location of these sections is specified in Fig. 7.15a to 7.18a. The section along the middle of the asperity (VS2), for all the models, shows that the cracks, developed from the top of the fault and from the top and bottom of the asperity, are generated symmetrically at the two sides of the fault. On the other hand, the sections located outside the asperity (VS1 and VS3) show the generation of asymmetric cracks. Even the sections VS1 and VS3 are located outside the asperity, they show that the lowest cracks occur at a depth corresponding to the same level of the bottom of the asperity, whereas the significance upper cracks are originated only from the top of the fault. The crack developed from the bottom and top of the asperity has the same length for all the models, as shown in section Vs2. On the contrary, the length of the cracks originated from the top of the fault (section VS1, VS2 and VS3) and from the bottom part outside the asperity (section VS1 and VS3) increase as the asperity approaches the top of the fault. This increment of length is small for the bottom cracks, while it is very large for the upper cracks. The crack from the top of the fault developed symmetrically from the two sides of the fault across the middle of the asperity (Section VS2), while it is asymmetric outside the asperity (Sections VS1 and VS2). This asymmetry is the same for the models with H=4.0km, 3.0km and 2.0km, while for the model with H=1.5km the asymmetry is inverted, possibly because the cracks originated from the top of the asperity of the model with H=1.5km extend until reaching a level –2.5km, which exceeds the level of the top boundary of the fault, equal to –3.0km. Once the cracks that come from the top of the asperity extend beyond the top boundary of the fault, these cracks and those originated from the top of the fault advance in parallel. This phenomenon may cause an inversion of the increment of the tensile stress on the two side of the fault, consequently, the asymmetry of the cracks developed from the top of the fault could be also inverted, as occurs in the model with H=1.5km shown in sections VS1 and VS3.

The results suggest that the effects of the asperity on the generation of cracks originated from the top boundary of the fault increase as the asperity approaches it. It may be clearly seen that for the model with H=4.0km and 3.0km, the effects of the asperity is slight, while for the model with H=2.0km and 1.5km they largely increase.

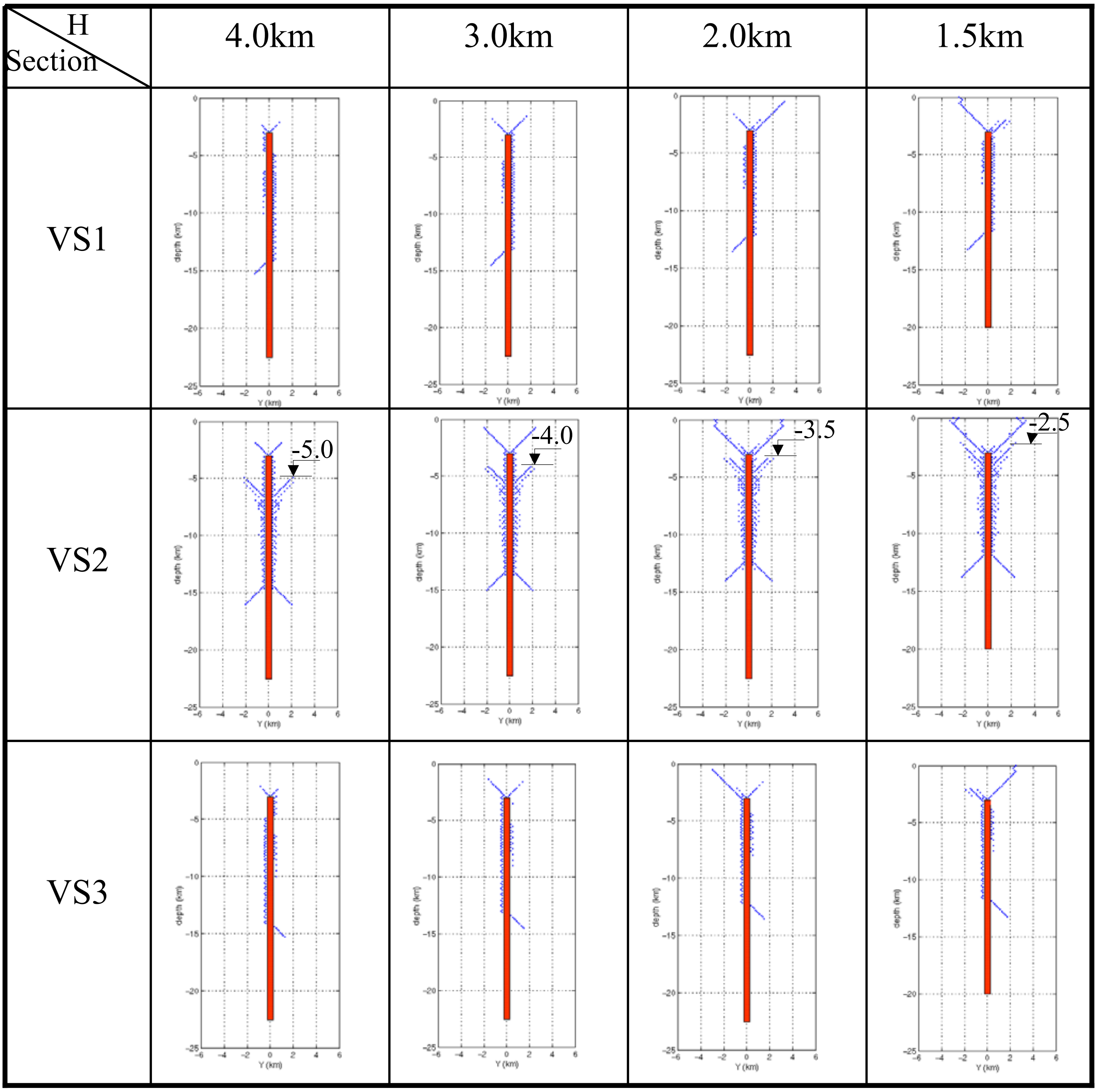

Figure 7.19. Vertical cross sections VS1, VS2 and VS3 for the four cases of the asperity model. The location of these sections is specified in Fig. 7.15a to7. 18a

Fig. 7.20 shows the horizontal cross sections HS1, HS2 and the Surface Rupture for the four cases. Sections HS1, located in the middle of the asperity as specified in Fig. 7.15b,c to 7.18b,c for all the models respectively, show similar characteristics, that is, the new cracks extend from the end of the fault and from the end of the asperity on the dilatational side of the pre-existing shear fault. Sections HS2, located at a 1.0km depth from the free-surface, as specified in Figs. 7.17b,c to 7.18b,c; show the cracks originated from the top of the fault for the models with *H*=2.0km and *H*=1.5km; while the cracks of the other two models do not reach this level. The purpose of Section HS2 is to show the difference of crack extension between the models with *H*=2.0km and *H*=1.5km. The trace of these cracks, located approximately 2.5 km from the fault, for the model with *H*=2.0km is parallel to the pre-existing fault and extend to the dilatational side. On the contrary, in the model with *H*=1.5km, the cracks extension is opposite. As explained before, this could happen because the increment of the tensile stress around the top of the fault is inverted on the two sides of the fault. This inversion is probably due to the proximity of the asperity to the top of the fault. The cracks originated from the asperity reach the top of the fault and from there they extend parallelly to the cracks originated from the top of the fault.

The surface rupture, as shown in Fig. 7.20, is observed only for the models with *H*=2.0km and *H*=1.5km. The cracks of the model with *H*=2.0km reach the free-surface in a small zone approximately 3.0km from the center of the trace of the pre-existing fault. On the other hand, the model with *H*=1.5km generates surface rupture of along 6.5km on the two side of the fault. The limiting conditions for the new cracks to reach the free-surface seems to be when the asperity is located between 2.0km and 1.5km below the top of the fault, of course, for the conditions given in the problem.

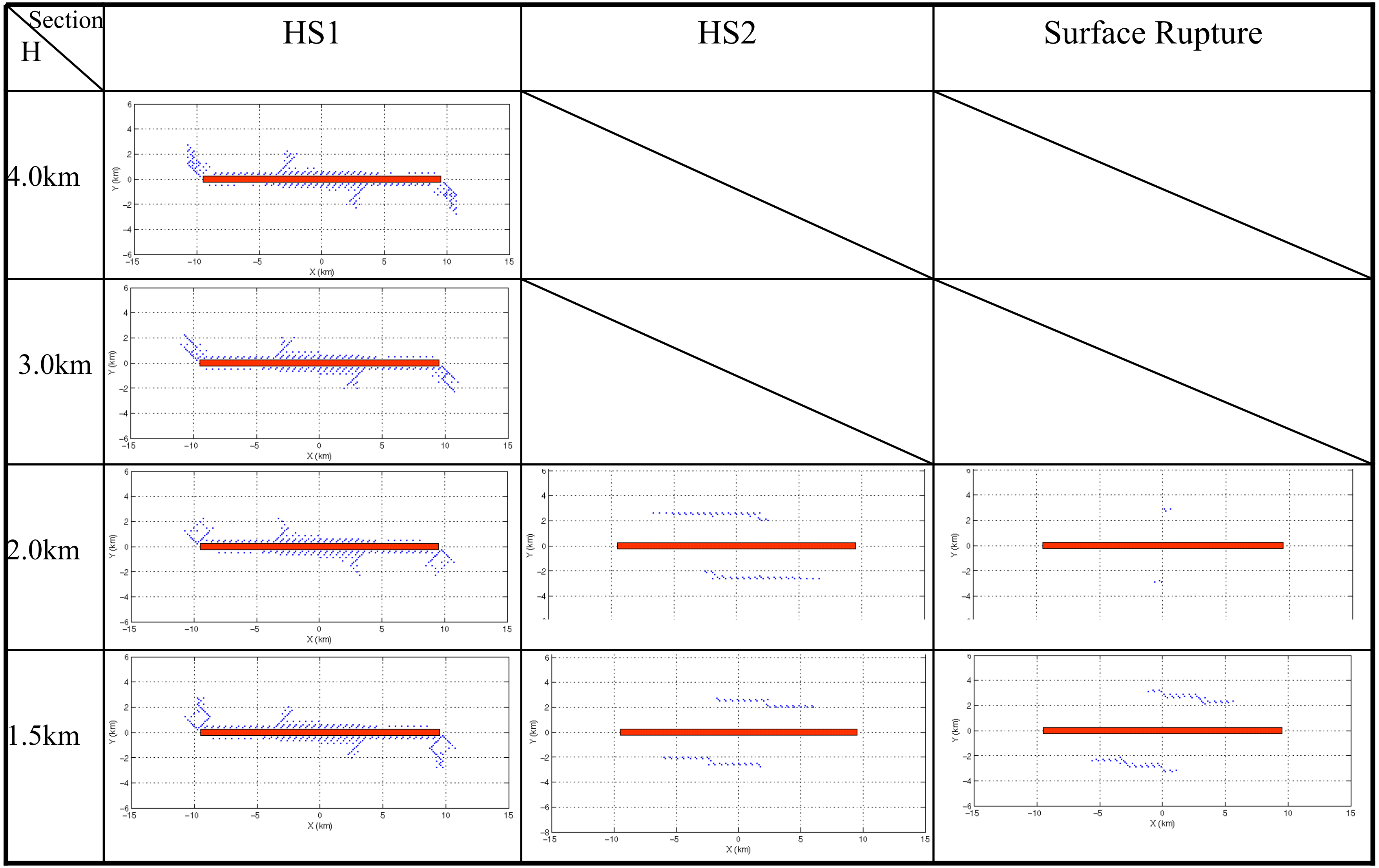

Figure 7.20. Horizontal cross sections HS1, HS2 and Surface Rupture for the four cases of the asperity model. The sections HS1 are specified in Fig. 7.15b,c to 7.18b,c for each case respectively, and the sections HS2 are specified on Fig. 7.17b,c and 18b,c for the cases with H=2.0km and H=1.5km respectively.

Chapter 8

Generation of Tensile Cracks by the Dynamic Shear Rupture Process during the 2000 Tottori Earthquake

8.1 Introduction

The 2000 Tottori (Japan) earthquake (Mj= 7.3) was originated on fault plane with strike N150E and a dip 90^o (Fig. 8.1). Small traces of surface breaks parallel and away to the trace of the main fault were found during the field observation developed by Fusejima et al. (2001) after the earthquake (Fig. 8.2). The study of seismic reflection survey around the 2000 Tottori earthquake area developed by Inoue et al. (2001) suggests the existence of fractures developed as a flower structure near the free-surface (Fig. 8.3). From these two investigations we can imply that some of the small cracks observed on the free-surface (Fig. 8.2) could correspond to the possible fracture developed as a flower structure during the Tottori earthquake. In order to get a better understanding of the surface rupture caused by this earthquake, a full shear dynamic rupture process is numerically simulated. The additional feature in the problem under consideration is the possibility of introducing internal new cracks that propagates under tensile stress as a consequence of the dynamic process of the shear slip propagation. As presented in the previous chapter (chapter 7) the generation of tensile cracks during a shear slipping in a shallow strike slip could form a flower structures and some of these cracks could reach the free-surface.

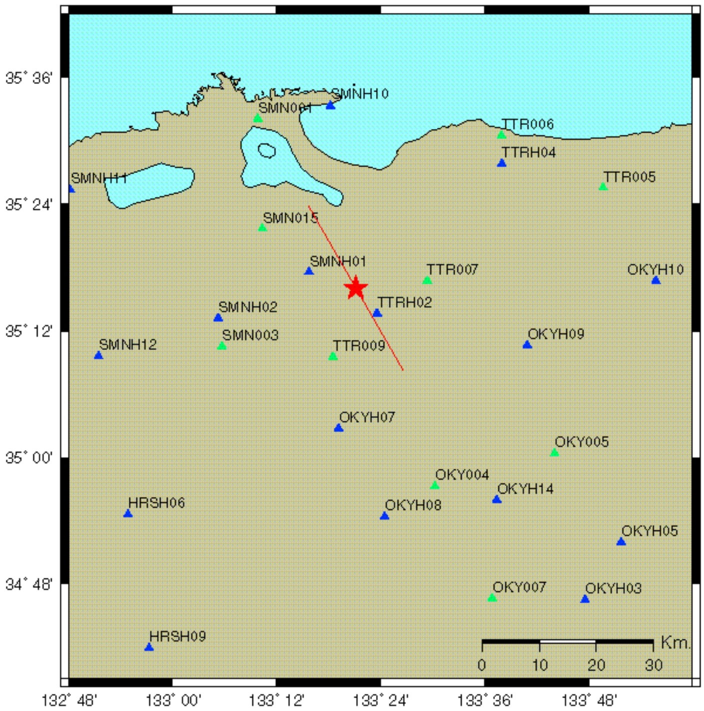

Figure 8.1. Map of the Tottori area. The straight line is the location of the fault model of the 2000 Tottori earthquake used for the simulation and the triangles are the stations records of Kiknet and Knet used for comparison.

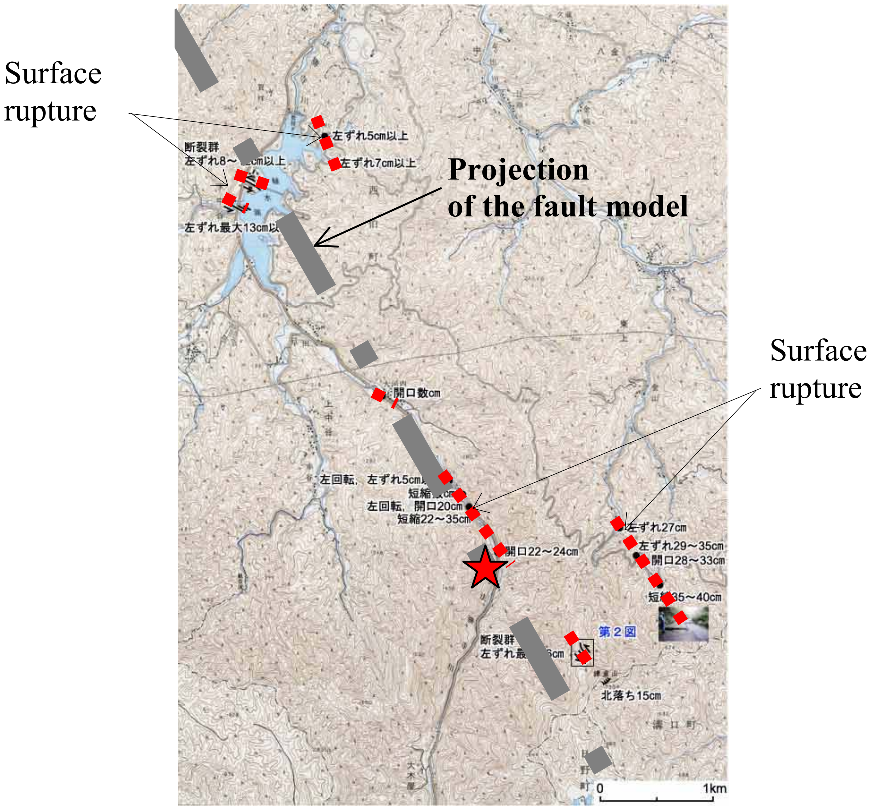

Figure 8.2. Surface rupture near the epicenter area of the 2000 Tottori earthquake. After the field observation developed by Fusejima et al. (2001).

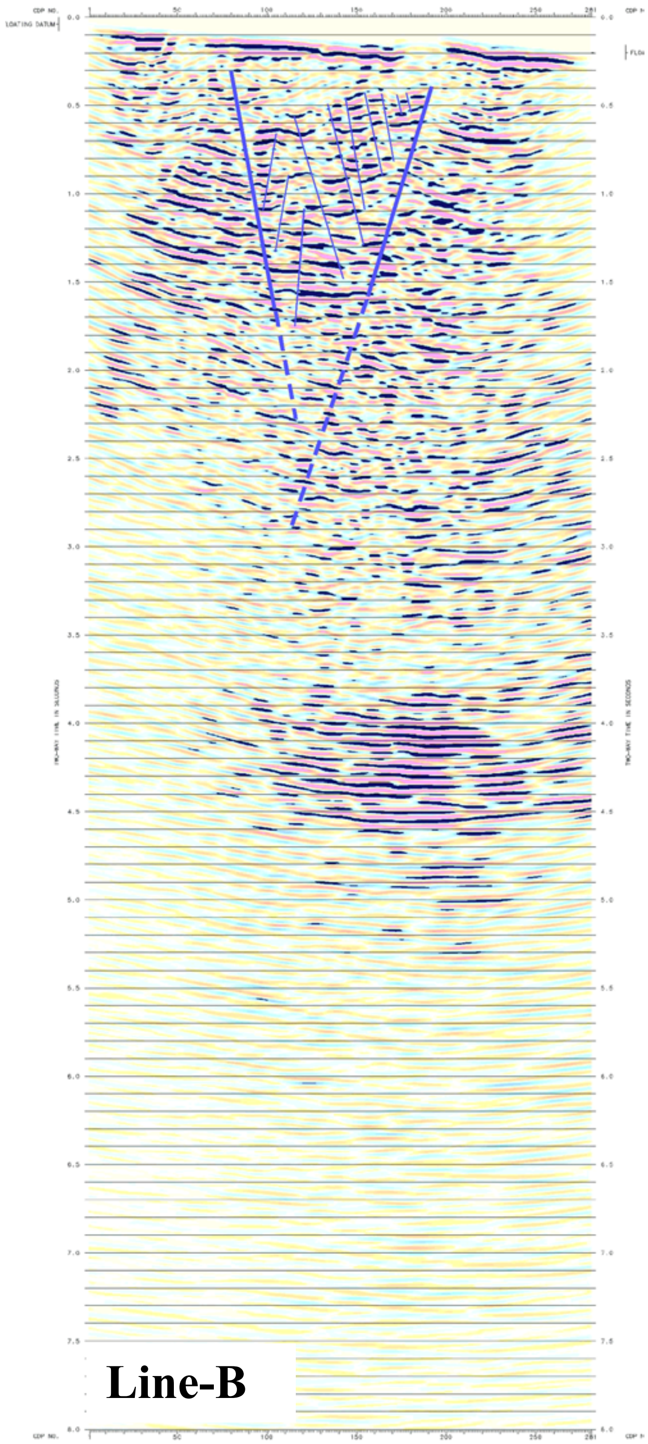

(a)

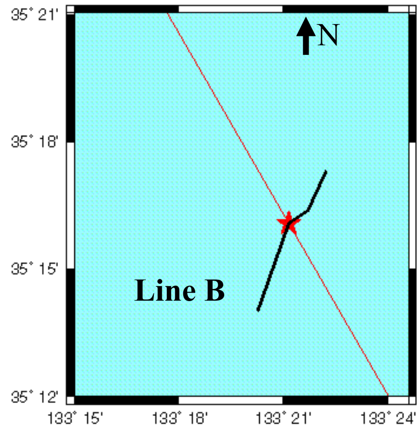

(b)

Figure 8.3. (a) Seismic profile until 5 to 6km depth corresponding to the Line B developed by Inoue et al. (2001). The straight lines show discontinuities like a flower structure in approximately 2 km depth. (b) Location of the Line B. The straight line is the projection of the fault model for the simulation of the 2000 Tottori earthquake. The start is the epicenter.

For the 3D shear dynamic rupture process simulation of the Tottori earthquakes we need to know: the geometry of the fault, and for the assumption of a slip weakening friction law, we need to define the stress drop, the strength excess and the critical slip along the fault. The direct estimation of these source parameters from observations are not feasible, the closest information about the source that we have is the results of the kinematic waveform inversion given by the slip distribution along the fault. In this context, we use the dynamic parameters calculated in the chapter 5 (item 5.2) in which the kinematic source model of Iwata et al. (2000) was used as a data. The dynamic stress drop distribution (Fig. 5.5a) and the strength excess (Fig 5.6) are used. For the critical slip (D_c) distribution, the values given by Fig. 5.7a are used, but with the assumption that a maximum D_c =2.0m is permitted (after many simulations for values greater than D_c =2.0m, we get very low frequency ground motion not consistent with the observation records). The velocity structure used for the simulation is shown in Table 5.1. In order to simulated the surface rupture, shown in Fig. 8.2, and according to the results presented in the chapter 7 in which the surface rupture comes from the flower structure developed from the top of the fault; it is assumed that the pre-existing fault, defined by the kinematic model (Iwata et al 2000), is embedded at a depth of 2 km from the free-surface as shown in Fig. 8.4. The model used for the simulation is a solid of 117km x 117km x 40km. For this it is need 4380480 cubic cells with 0.5 km long sides of each cubic cell. For the generation of the tensile cracks, it is assumed that the critical fracture energy in mode I, G_{Ic}, changes with depth according to the velocity structure given in Table 5.1. That is, for the first layer G_{Ic}=10x10^{5}J/m^2, second layer G_{Ic}=4x10^{5}J/m^2 and for the third layer G_{Ic}=3x10^{5}J/m^2. The coefficient k_r=1.5 is constant.

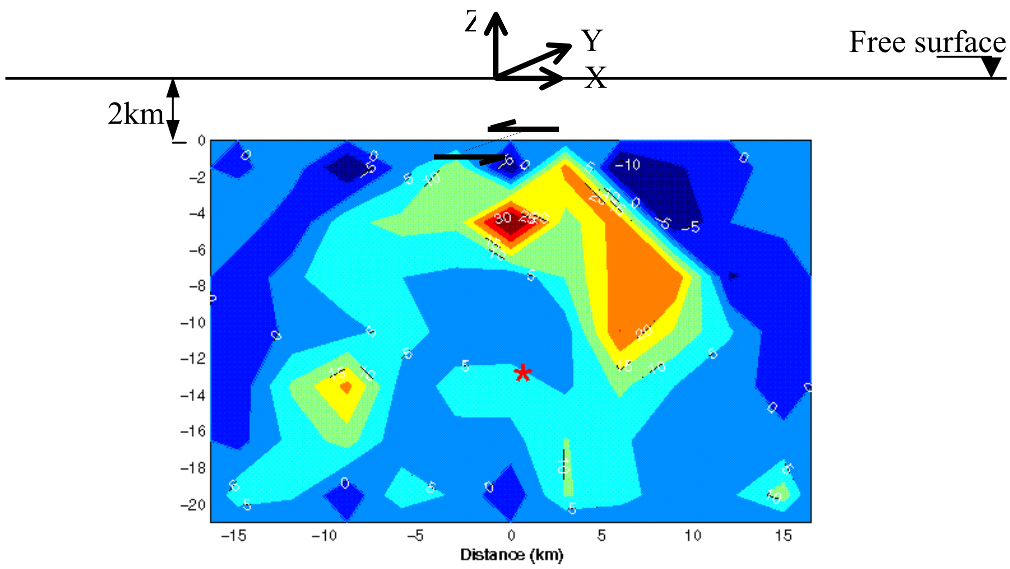

Figure 8.4. Fault model embedded at a depth of 2km from the free-surface used for the 3D dynamic simulation of the 2000 Tottori earthquake. The fault shows the distribution of the dynamic stress drop calculated in the chapter 5 (item 5.2) and show in Fig. 5.5a.

8.2 Simulation Results of the Distribution of Tensile Cracks and Surface Rupture

The final results of the generation of tensile cracks are shown in Figs. 8.5 to 8.8. Fig. 8.5 shows from the two sides of the fault two views in perspective of the final stage of the new cracks. Since the rupture is not a pure strike slip and the dynamic parameters distributions are very heterogeneous (Fig. 5.5 to 5.7), it may be seen that the new cracks grew from the two side of the fault following different patterns and forming new fractures as a complex flower structure. As observed in Figs 8.6a and 8.6c, in which bird eye's views and an outline view of the fault respectively are presented, the orientation of the new cracks across the pre-existing fault is not symmetric. From these figures and from the frontal view of Fig. 8.6b, the tensile cracks are generated mainly from the asperity zone (area of highest values of stress drop) and from the top of the fault.

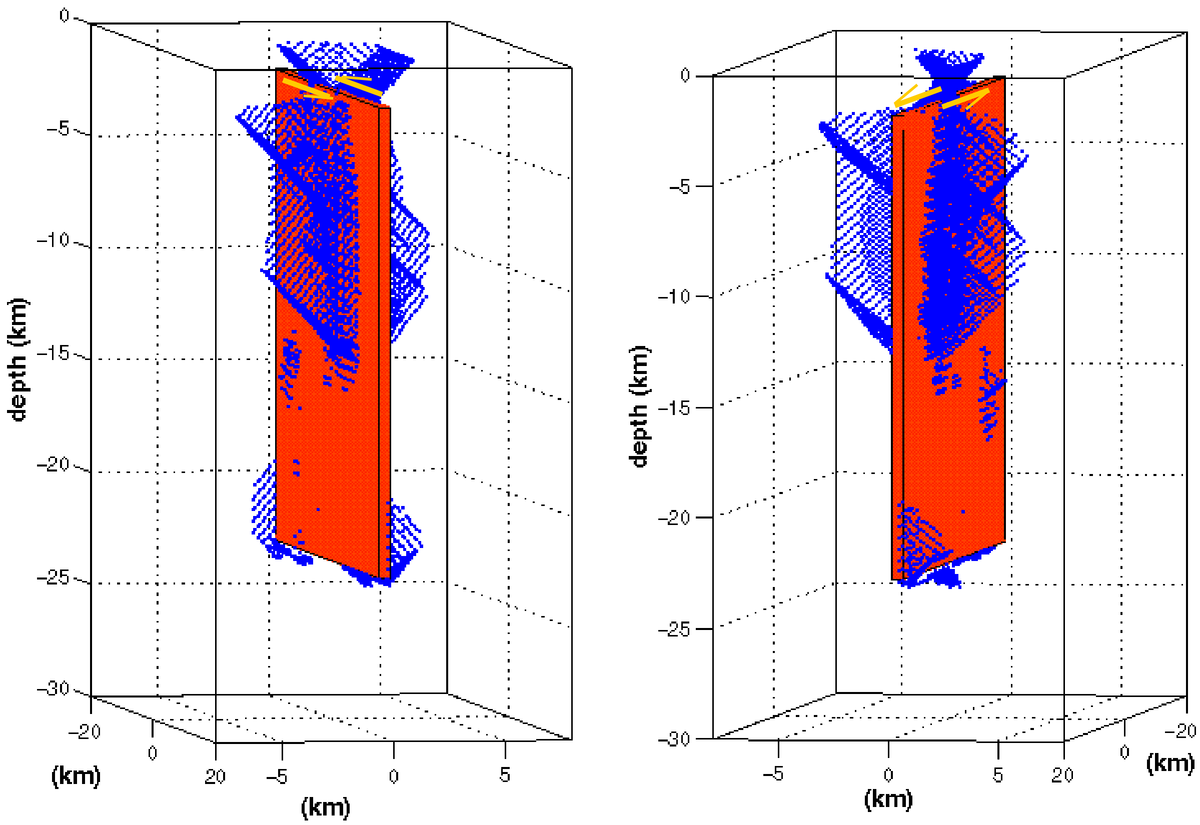

Figure 8.5. Two perspectives of the final stage of the cracks evolution for the 2000 Tottori earthquake dynamic simulation. The red color represents the shear crack on the pre-existing fault and the blue color represents the tensile cracks

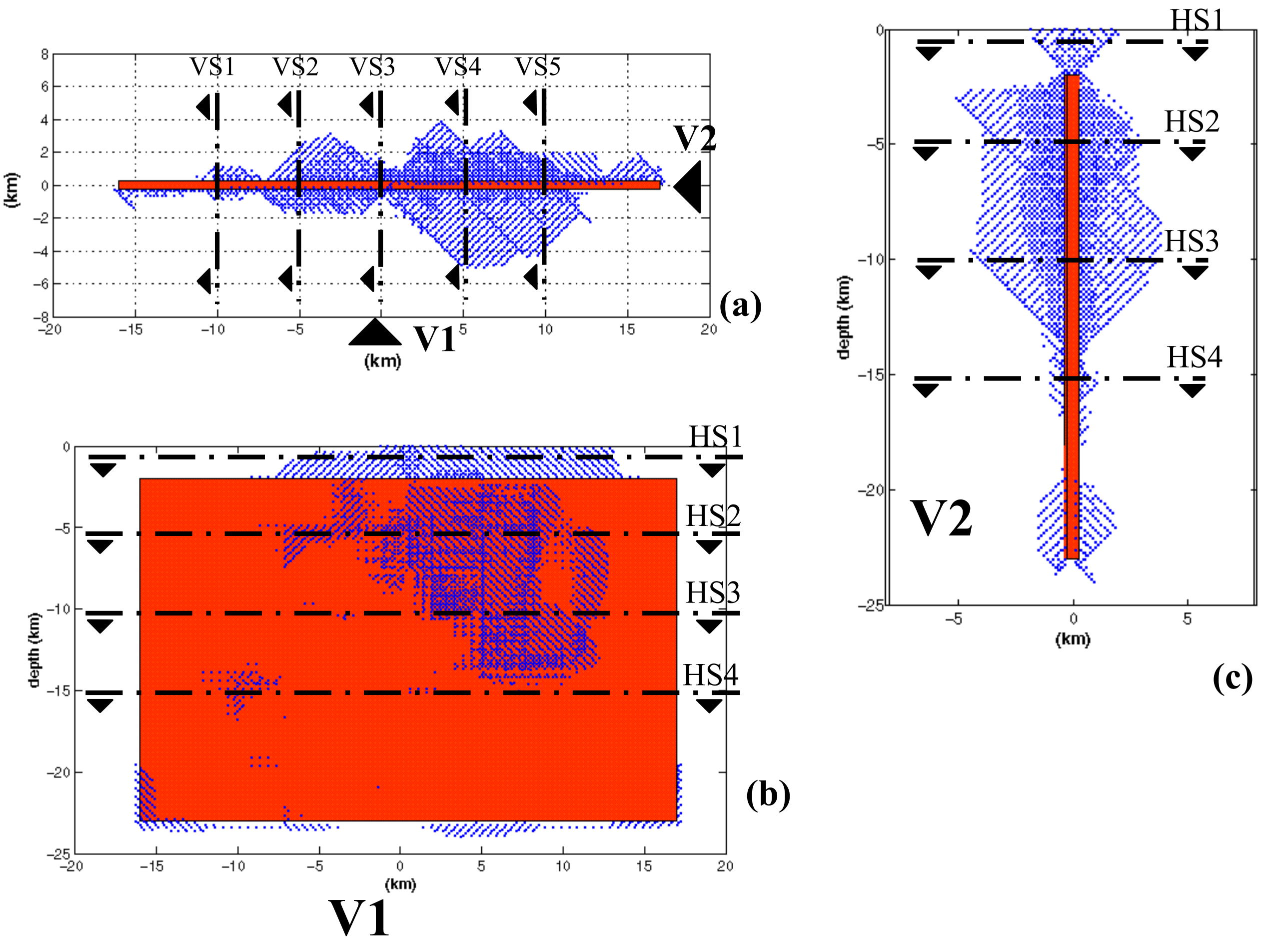

Figure 8.6. Views of the final stage of the cracks evolution for the 2000 Tottori earthquake dynamic simulation: (a) Bird's eye view; (b) frontal view (V1); (c) outline view (V2)

The complex flower structure developed from the pre-existing fault are clearly observed in the vertical cross section (VS1, VS2, VS3, VS4 and VS5) shown in Fig.8.7, the location of these sections is specified in Fig. 8.6a. Section VS1 shows a few cracks, this zone has lower values of stress drop. Sections VS2 and VS4, located symmetrically from the center of the fault, show similar characteristics, that is, from the right side of sectionVS2 and left side of VS4 one main crack is developed originated from around 7.5km depth growing toward the free-surface. From the left side of VS2 and right side of VS4, two main cracks are developed, one originate from around 5km depth and grows toward the depth and the other one originates from the top of the fault and grow towards the free-surface. This second one, in the section VS4, reaches the free-surface while in VS2 the crack stops very close to the free-surface. It could be observed also in both sections the development of one small crack originated from the bottom of the fault. The cracks originated in section VS4 extend larger distance than those originated in the section VS2. Section VS4 also shows de development of more cracks than in VS2. This difference between these two sections is mainly because the section VS4 is located in the main zone of the asperity. Section VS3, located in the middle of the fault, shows small cracks originated mainly along the asperity and top of the fault. Section VS5 shows two main cracks, one originated from around 14km depth (left side) and the other one (right side) from the top of the fault, both grows toward the free-surface. The crack developed from the top of the fault reaches the free-surface.

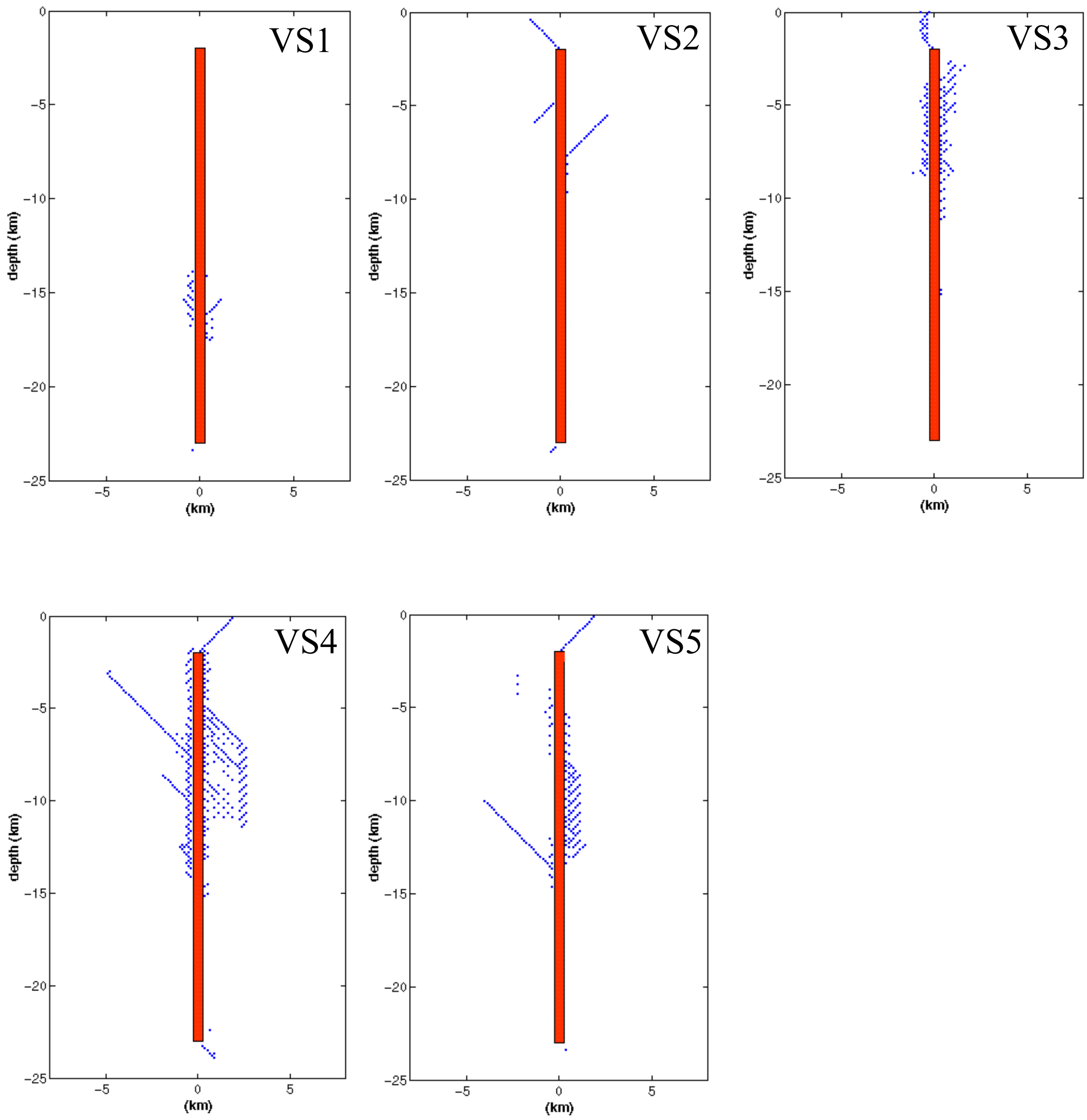

Figure 8.7. Vertical cross sections VS1, VS2, VS3, VS4 and VS5 of the final stage of the cracks evolution for the 2000 Tottori earthquake dynamic simulation. The location of these sections is specified in Fig. 8.6a

The surface rupture and horizontal cross section (HS1, HS2, HS3 and HS4) are shown in Fig. 8.8, the location of these sections is specified in Fig. 8.6b and 8.6c. The main characteristic of all these sections is that the new cracks extend from the asperity and in an asymmetric way from the two sides of the fault, that is, the cracks originate in the same point of the two side of the fault, but the extension is opposite.

The faulting generated a surface rupture on only one side of the fault of along 10.0km parallel to the trace of the main fault and 2.0km distance from the fault. These surface rupture crosses to the other side of the fault at the middle of the fault. The section HS1, located 0.7 km depth from the free-surface, shows cracks parallel to the fault on the two side of the fault. The surface rupture and the cracks from section HS1 correspond to the flower structure generated from the top of the fault. The section HS2 and HS3, located 5km and 10.0km depth respectively, crosses the main part of the asperity zone. The cracks are generated in an opposite pattern compared with the section HS1. Section HS4, located 15km depth and outside of the asperity, shows smalls and a few cracks.

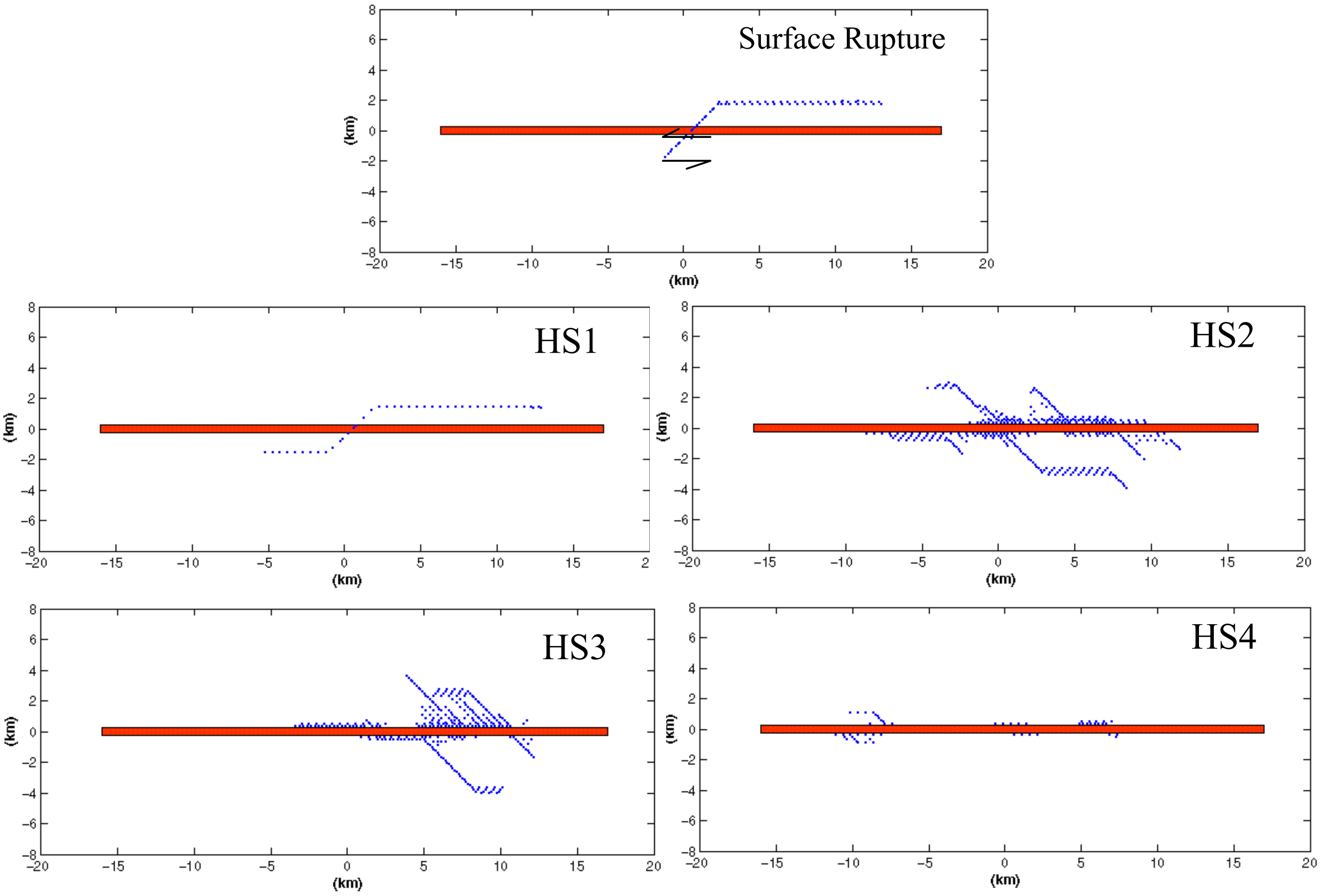

Figure 8.8. Surface Rupture and horizontal cross sections HS1, HS2, HS3 and HS4 of the final stage of the cracks evolution for the 2000 Tottori earthquake dynamic simulation. The location of these sections is specified in Fig. 8.6b and c

8.3 The Tensile Crack Simulation Associated with Observation and After Shock Distribution.

As mentioned in the introduction of this chapter, during the field observation developed by Fusejima et al. (2000) after the 2000 Tottori (Japan) earthquake, several small cracks were found on the free-surface parallel to the causative fault. Some of these cracks could correspond to the possible flower structures that could be originated during the rupture process of the Tottori earthquake. The surface rupture simulated in the previous section is similar to some of the trace of the cracks found in the field as observed in Fig. 8.9.

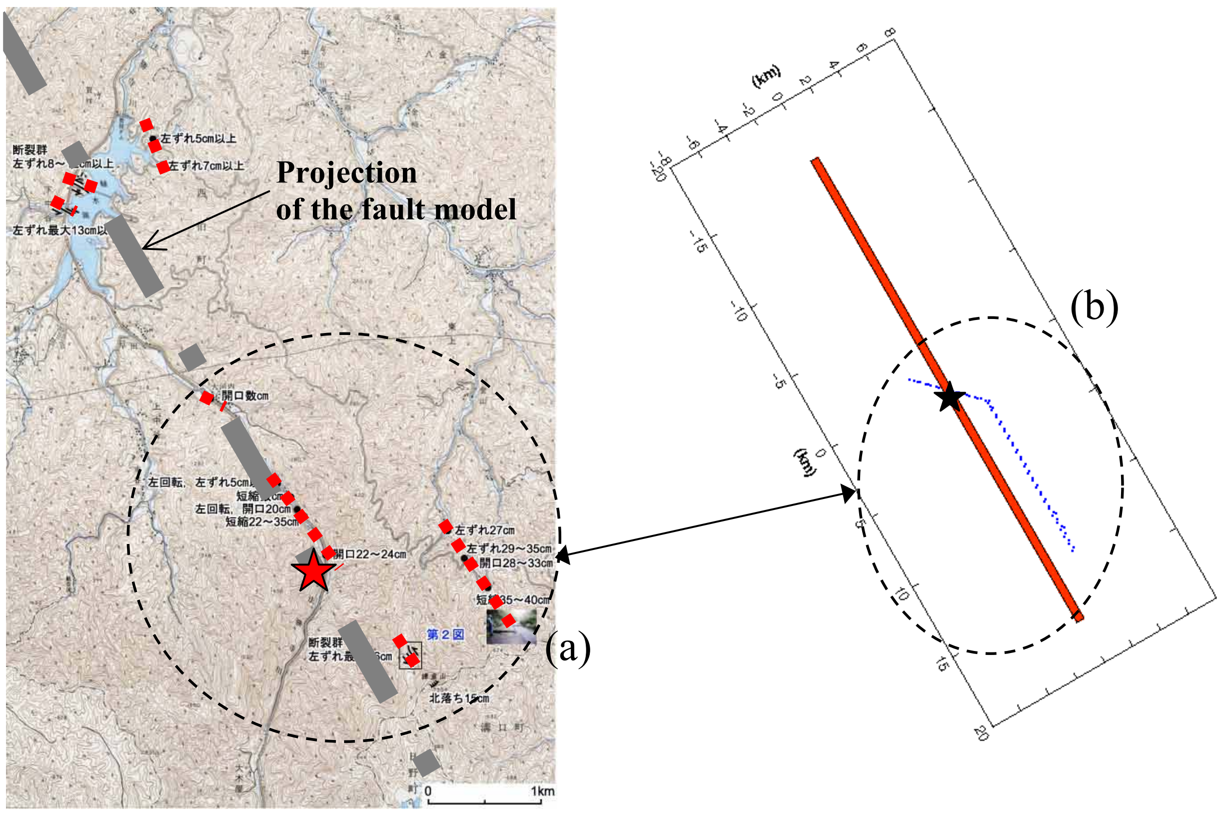

Figure 8.9. Surface rupture observed by Fusejima et al. (2000) in the field (a) associated with the surface rupture simulated (b)

The hypothesis of the development of a flower structure is supported by the study of seismic reflection survey around the 2000 Tottori (Japan) earthquake area developed by Inoue et al. (2001), as observed in Fig. 8.3. From the tomographic slices of P wave velocity at different depths (Fig. 8.10) developed by Aben et al. (2001), the first two images (0.0km to 2.0km) also suggest the existence of a flower structure near the free-surface.

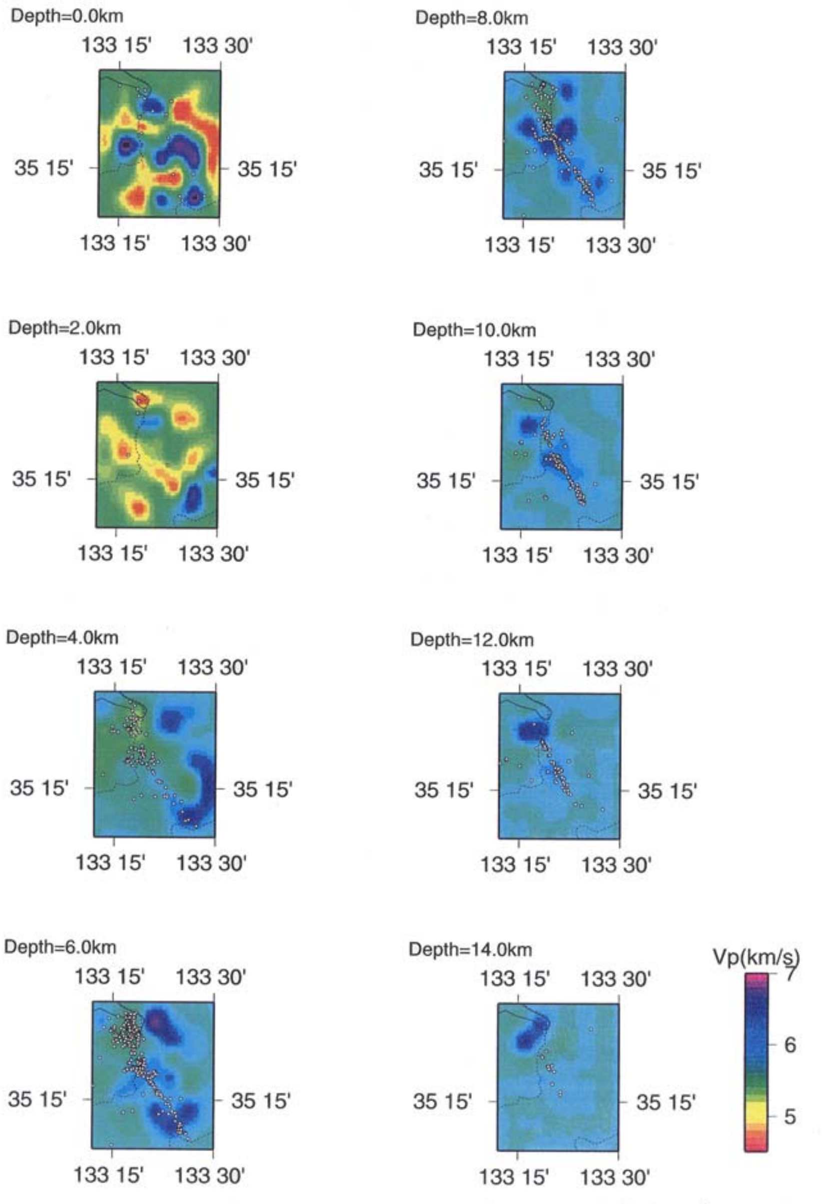

Figure 8.10. Tomographic slices developed by Aben et al. (2001) at different depth showing P wave velocity and aftershock distribution of the 2000 Tottori earthquake. The first two images (0.0km to 2.0km) suggest the existence of a flower structure near the free-surface because the strong discontinuity of lower values of P waves velocity in localized zone around the causative fault.

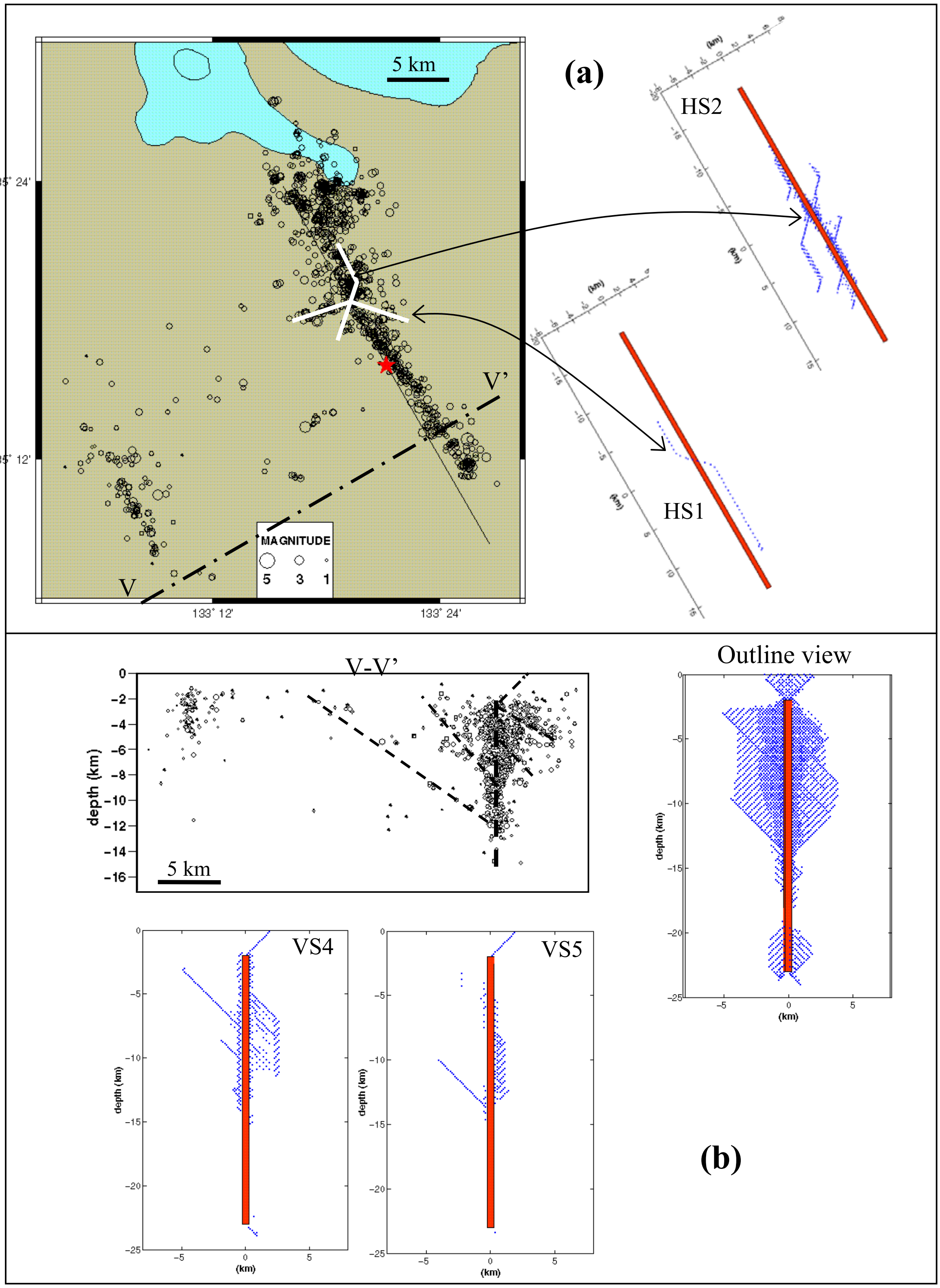

Figure 8.11. aftershock distribution associated with the simulated cracks: (a) Bird's eye view of aftershock associated with the horizontal section HS1 and HS2 of cracks (see Fig. 8.8). (b) Vertical distribution (section V-V') of aftershock associated with the outline view V2 (see Fig. 8.6c) and vertical cross sections VS4 and VS5 of cracks distribution (see Fig. 8.7)

The new surfaces of tensile cracks could be the zone of the shear slipping as a second step of the formation of cracks. This idea, as explained before in chapter 3 (item 3.1), comes since Scholz, (1968) and Lajtai, (1971), in which they conclude that the shear cracks develop as a plane of shear failure only after a long history of tensile microfracturing. Steps include the formation of individual tensile microcracks, propagation and linking of these cracks and finally larger scale shear failure. In this context, it suggests that some of the cracks opened during the Tottori earthquake simulation could be zone of aftershock. In Fig. 8.11 we associates some of the cracks with the after shocks distribution. In Fig. 8.11a, in which shows the bird's eye view of aftershock distribution, could be observed swarm of events that follow approximately the traces as specified by the white line. This part of aftershock could be related to the cracks of section HS1 and HS2, as show in Fig. 8.11a. The vertical view (section V-V) of the aftershock distribution (Fig. 8.11b) could be associated to the cross section VS4 and VS5 and the outline view V2 (see Fig. 8.6c) of cracks distribution as observed in Fig. 8.11b. If these cracks correspond to the zone of the aftershocks, the cracks simulated could have been extended and be larger during the real earthquake, as specified with the dashed line in the vertical view (section V-V) of aftershock distribution (Fig. 8.11b).

8.4. Simulation of Near Source Ground Motion from the Shear Rupture Process and Tensile Cracks Generation: Comparison with a Model that does not Generate Tensile Cracks

A model in which no tensile cracks are generated is also simulated. Fig. 8.12 shows snapshots every 2 seconds during 14 seconds of the shear slip distribution along the fault for the model in which tensile cracks were generated and for the model without cracks. The rupture process of the two models shows similar characteristics until around 8 seconds, after that the model wit cracks starts to develop higher values of slip. The final stage of the slip shows that the model with cracks slips almost twice the model without cracks. Similar characteristics could be observed in the snapshots of slip velocity shown in Fig. 8.13. From this figure, around 8.0 seconds, could be observed that the model with cracks generate additional slip velocity in the borders of the fault, it could be caused by the generation of cracks. The final slip distribution of the two models is also compared with the final slip distribution of the kinematc model (Fig. 8.14). The maximum value of the model without cracks is slightly higher than the kinematic model. But the model with cracks shows the highest values, as mentioned before, almost twice the model without cracks.

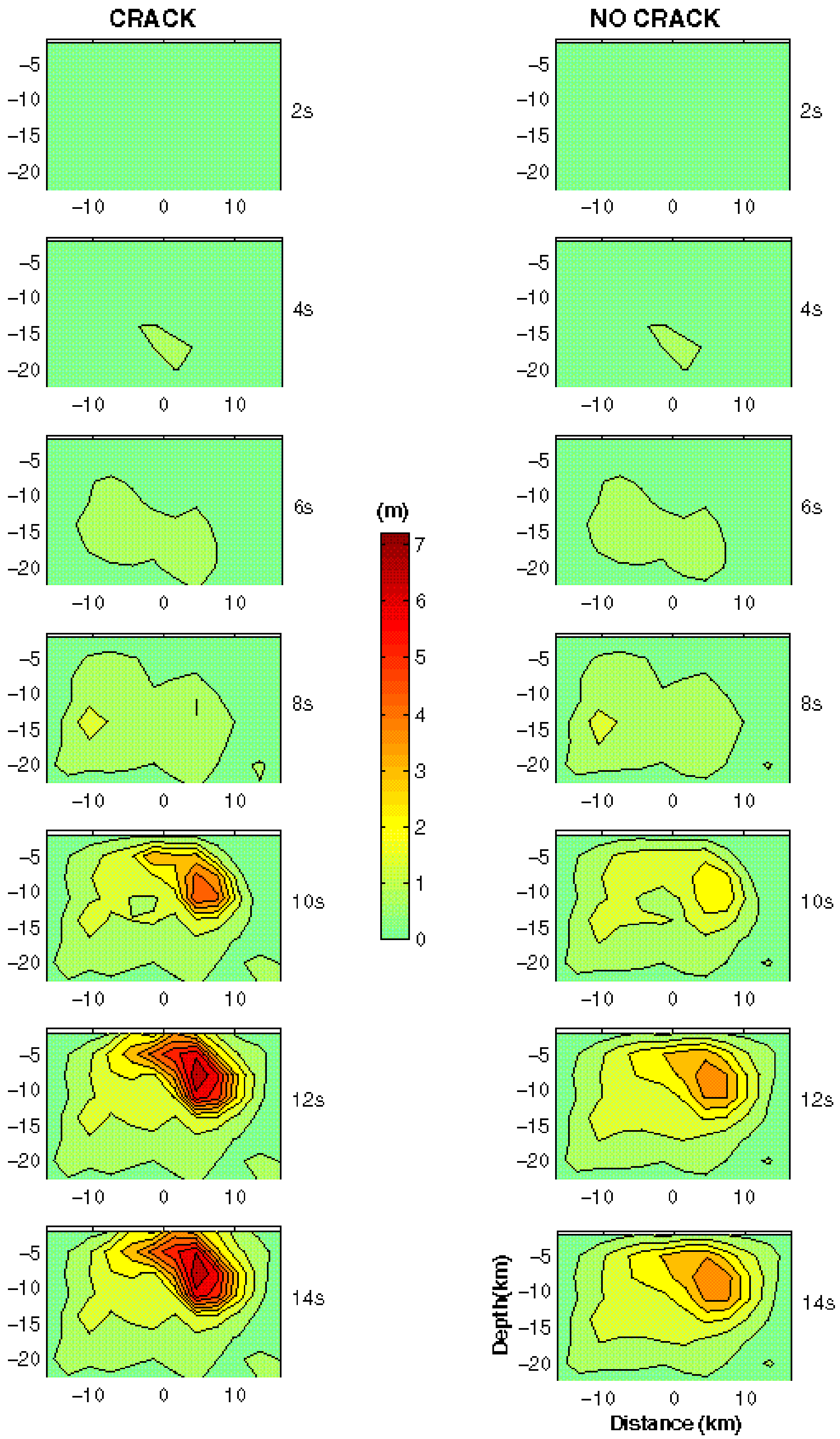

Figure 8.12. Snapshots every 2 seconds during 14 seconds of the shear slip distribution along the fault for the model in which tensile cracks were generated and for the model without cracks.

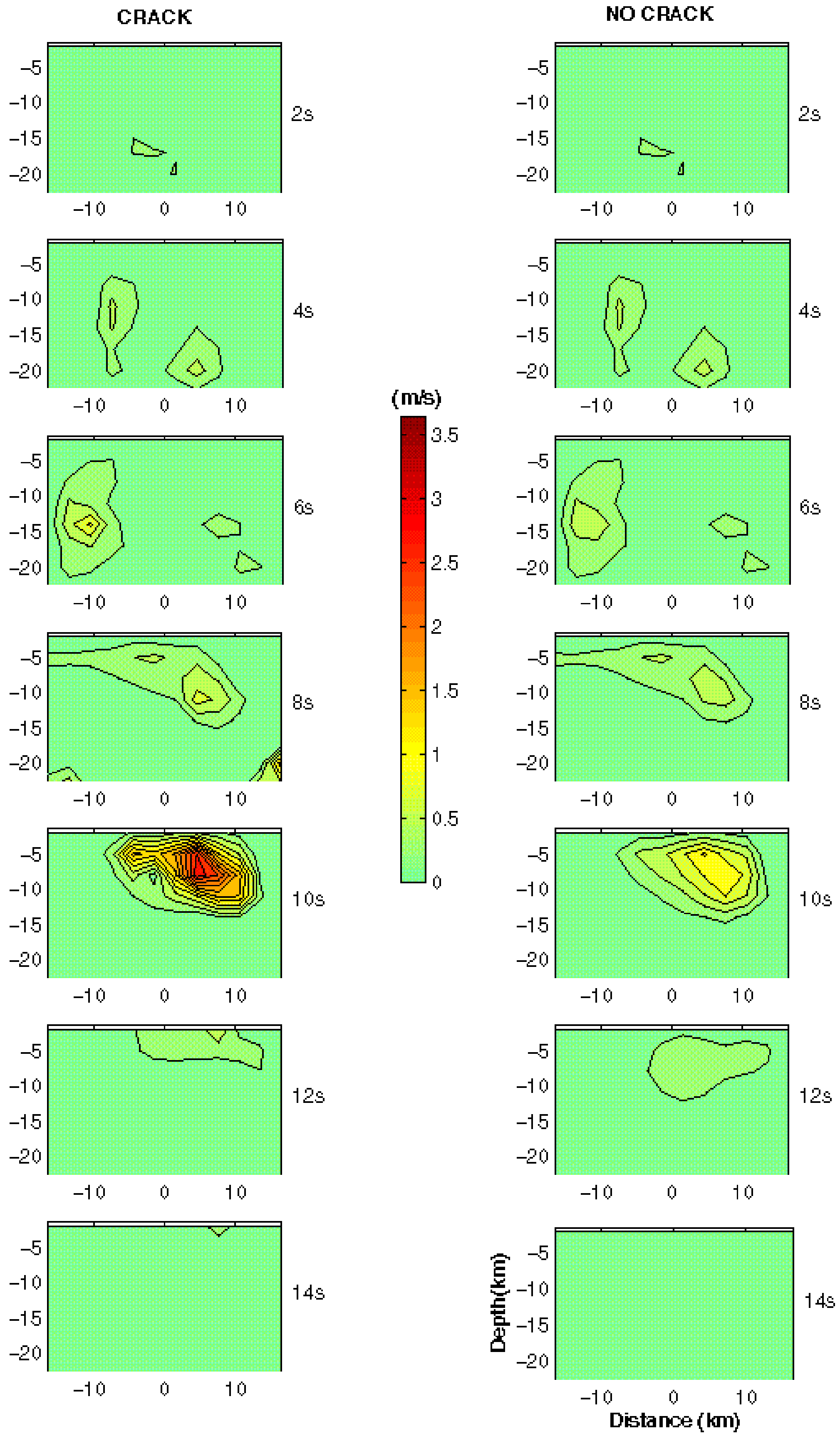

Figure 8.13. Snapshots every 2 seconds during 14 seconds of the shear slip velocity distribution along the fault for the model in which tensile cracks were generated and for the model without cracks.

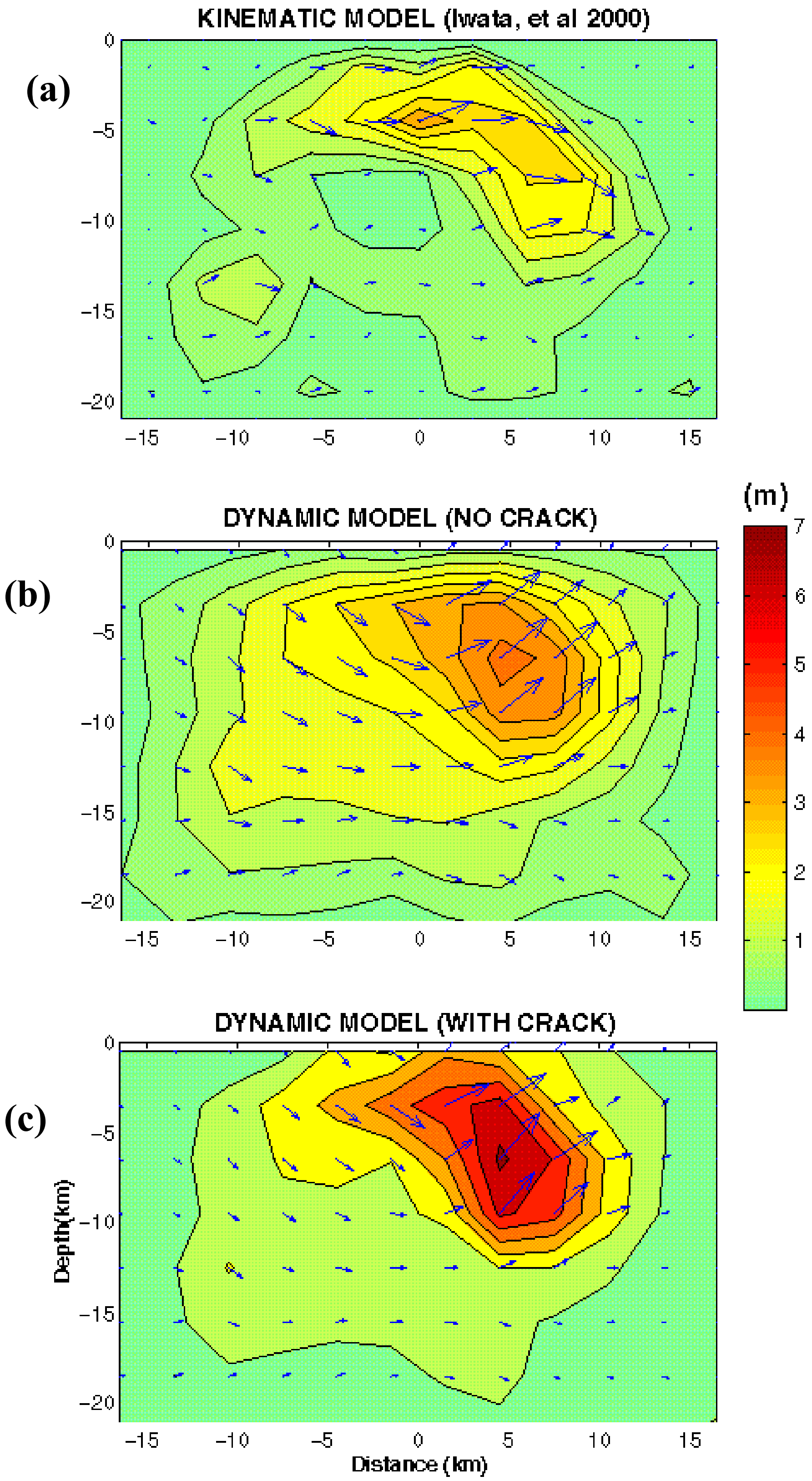

Figure 8.14. Final slip distribution of the fault model of the 2000 Tottori earthquake simulation: (a) Kinematic model calculated by Iwata et al (2000); (b) Dynamic model free of tensile cracks; (c) Dynamic model in which tensile cracks are generated.

The maximum displacement and velocity ground motion of the two models are shown in Fig. 8.15 and 8.16 respectively. The pattern of the ground motion of the model with cracks compared to the model without cracks suffers a drastic change in all the components. The maximum values of the displacements are around twice the model without cracks (Fig. 8.15). For the peak velocity values (Fig. 8.16), the maximum values of the model with cracks are locally concentrated on the cracks that reached the free-surface.

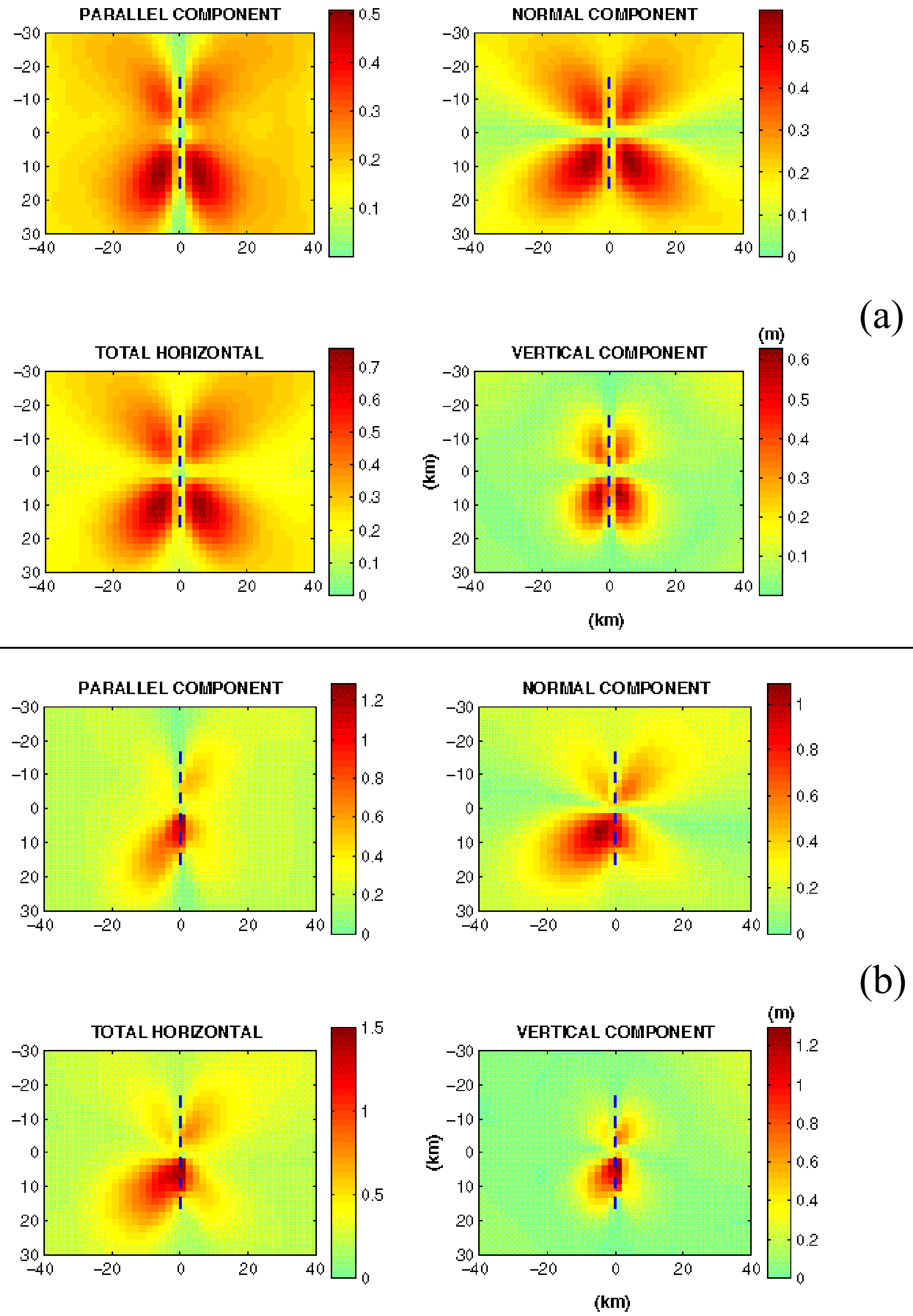

Figure 8.15. Maximum displacements ground motion on the surface (a) caused by the dynamic model free of cracks; (b) caused by the dynamic model in which tensile cracks are generated.

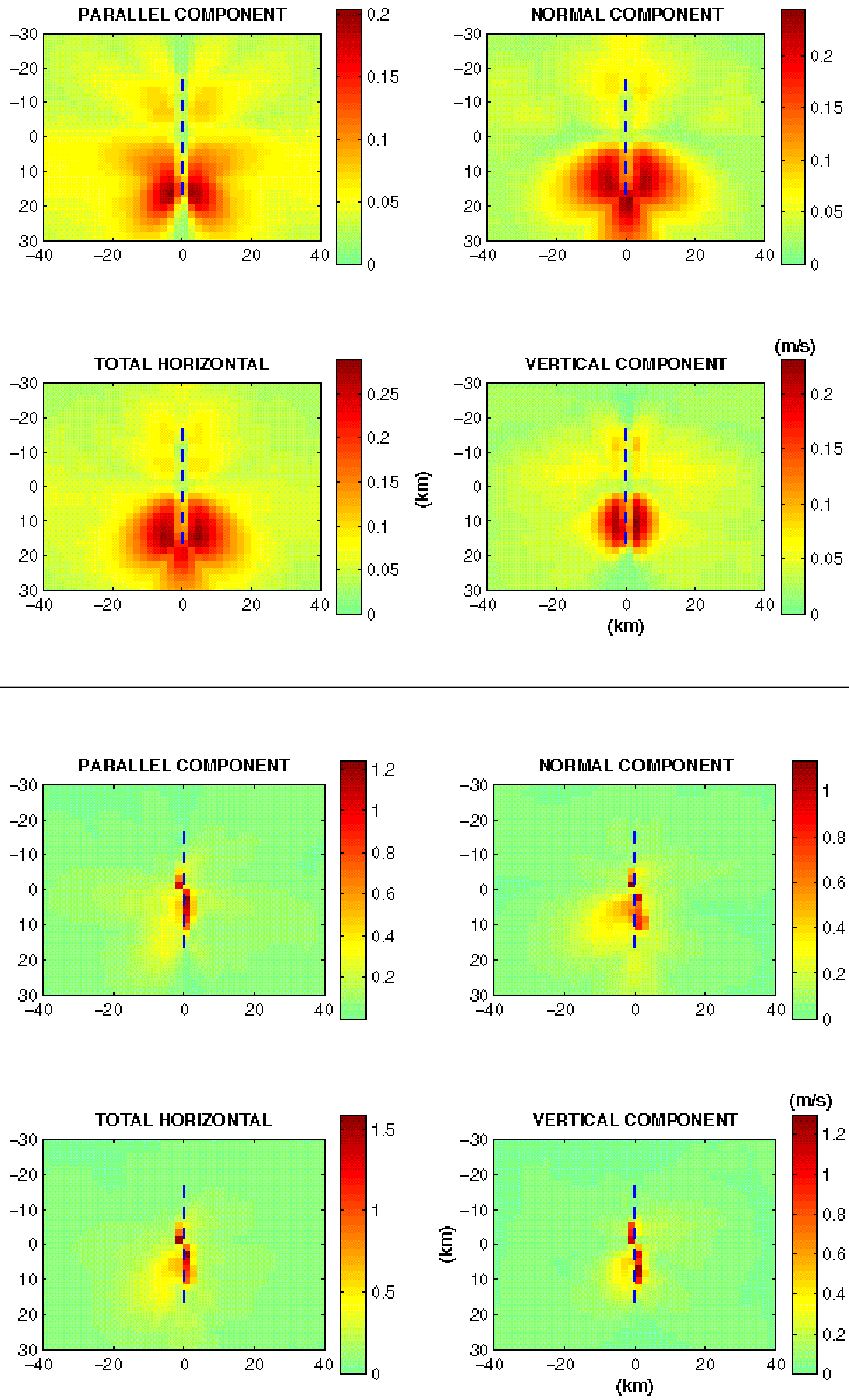

(a)

(b)

Figure 8.16. Peak velocity ground motion on the surface (a) caused by the dynamic model free of cracks; (b) caused by the dynamic model in which tensile cracks are generated.

In order to validate the dynamic simulation studied here, the waveform simulated using the model with cracks and without cracks is compared with the ground motions recorded by the Kiknet and Knet. Figs. 8.1shows the location of all the stations used for comparison. Fig. 8.17 and 8.18 show the comparison with the stations of Knet for the model without cracks and cracks respectively. Fig. 8.19 and 8.20 show the comparison with the station of Kiknet for the model without cracks and cracks respectively. In general, the simulations using the two models fit well the observations. The comparison with the station records are in the frequency range of 0.05 to 0.5 Hz.

Now lets compare the waveform between the two models. Fig. 8.21 and 8.22 show the waveform simulated using the two models for the corresponding location of Knet and Kik net stations respectively in a frequency range of 0.05 to 0.5 Hz. It could be observed that the model with cracks generates shorter wavelengths than the model with cracks in almost all the stations. This difference of wave between the two models could be observed more clearly in Fig, 8.23 and 8.24, in which the waves are not filtered. These results suggest that the model with cracks predicts ground motions with higher frequency content than the model without cracks. This difference between the two models is highest near the fault, as observed in the waveforms corresponding to the station TTRD02 of Kiknet (Fig. 8.24), in which the waveform of the model with cracks is very larger than the model without cracks.

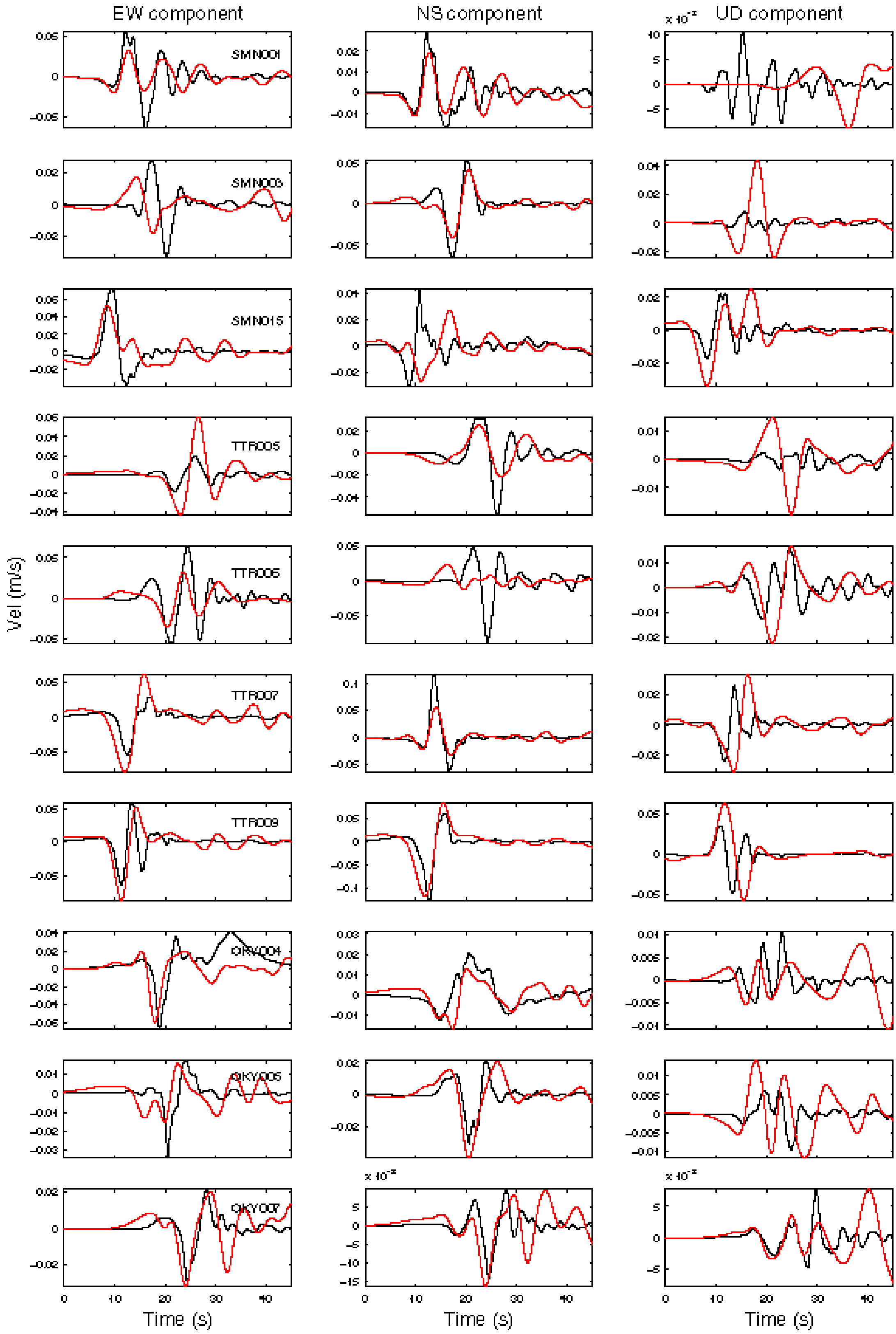

Figure 8.17 Comparison of the velocity ground motion simulation with stations records of Knet in frequency range of 0.05Hz to 0.5Hz. The simulation corresponds to the model free of tensile cracks. Red line is the simulation and black line is the recorded.

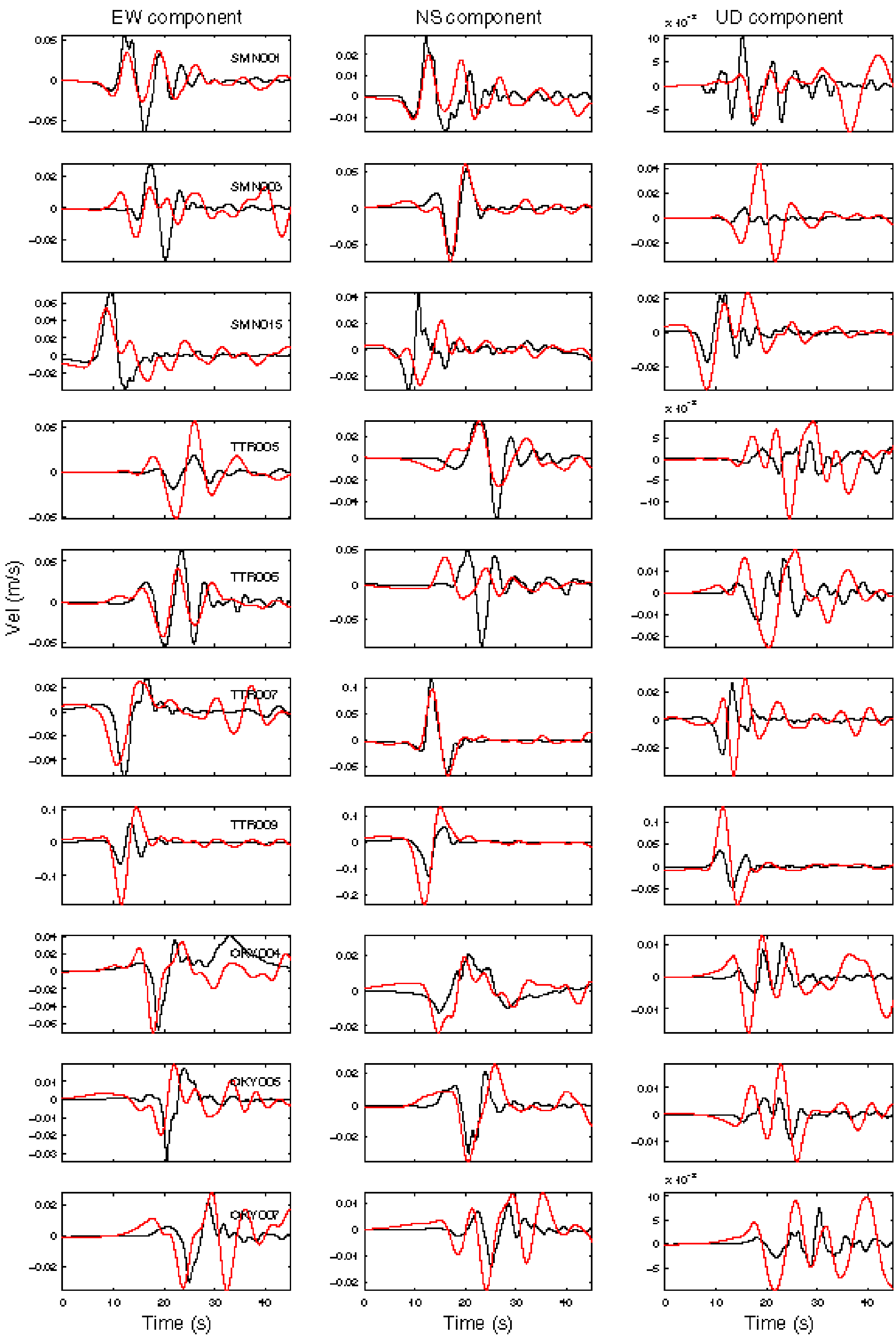

Figure 8.18 Comparison of the velocity ground motion simulation with stations records of Knet in frequency range of 0.05Hz to 0.5Hz. The simulation corresponds to the model in which tensile cracks are generated. Red line is the simulation and black line is the recorded.

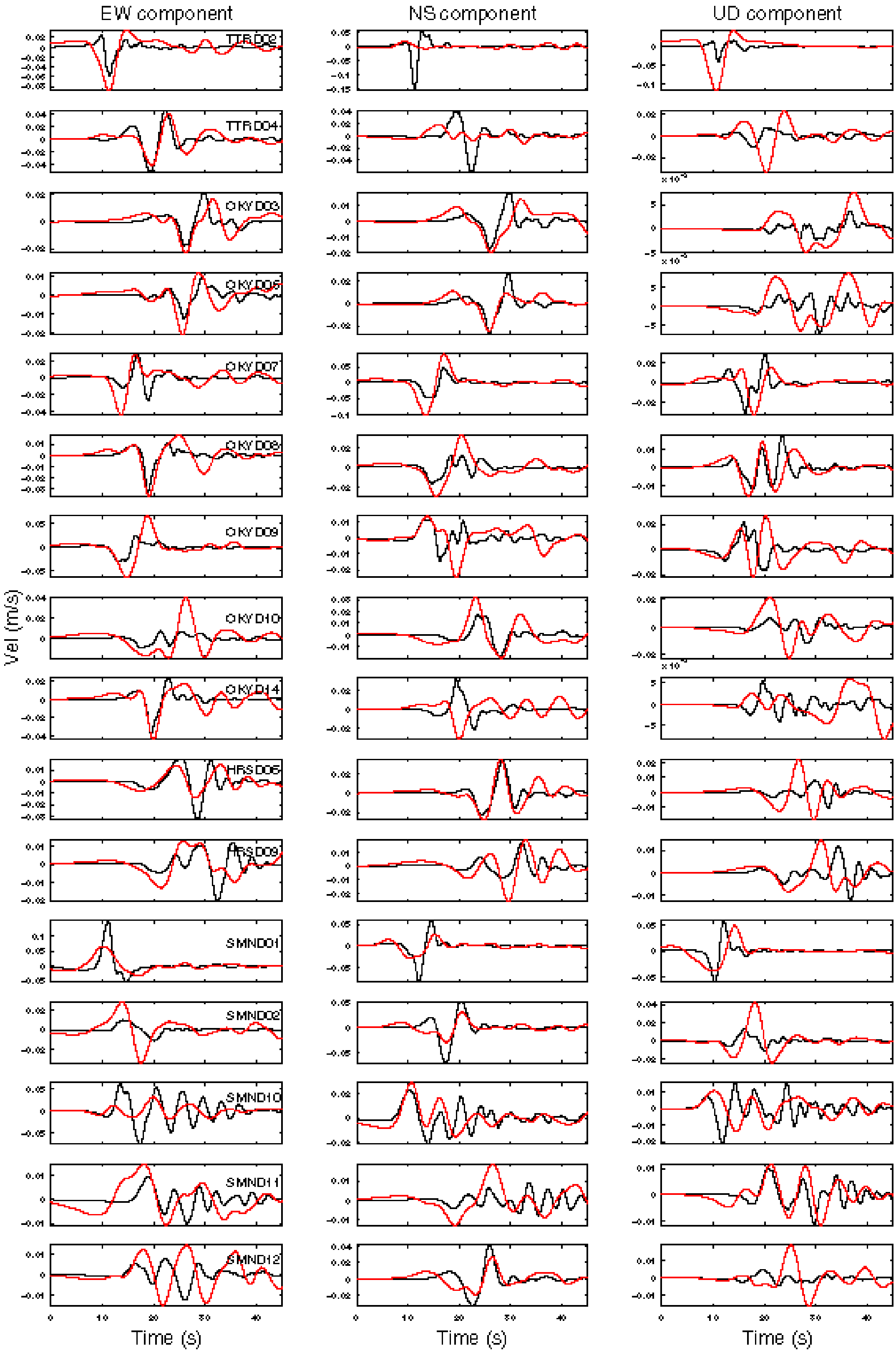

Figure 8.19 Comparison of the velocity ground motion simulation with stations records of Kiknet in frequency range of 0.05Hz to 0.5Hz. The simulation corresponds to the model free of tensile cracks. Red line is the simulation and black line is the recorded

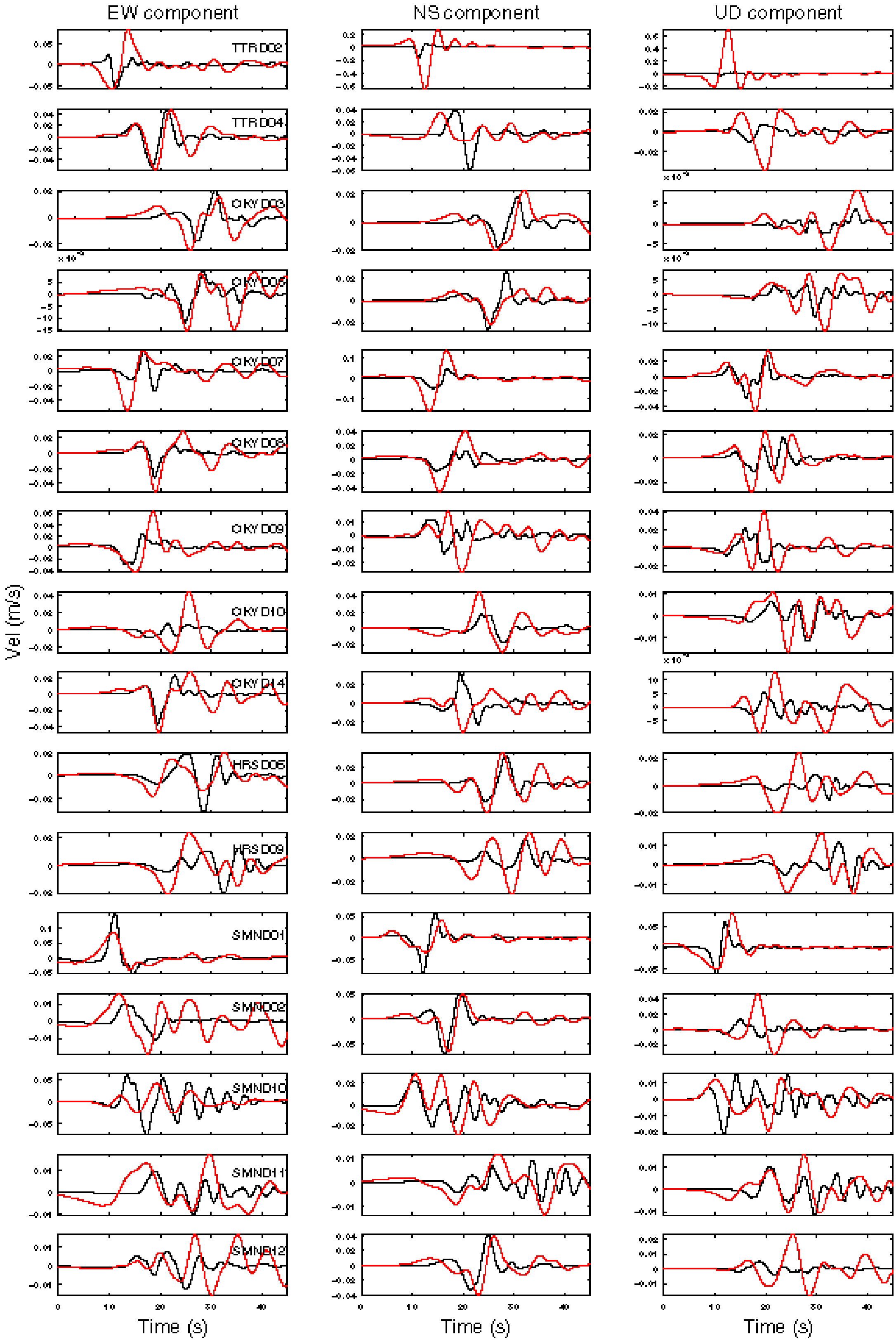

Figure 8.20 Comparison of the velocity ground motion simulation with stations records of Kiknet in frequency range of 0.05Hz to 0.5Hz. The simulation corresponds to the model in which tensile cracks are generated. Red line is the simulation and black line is the recorded.

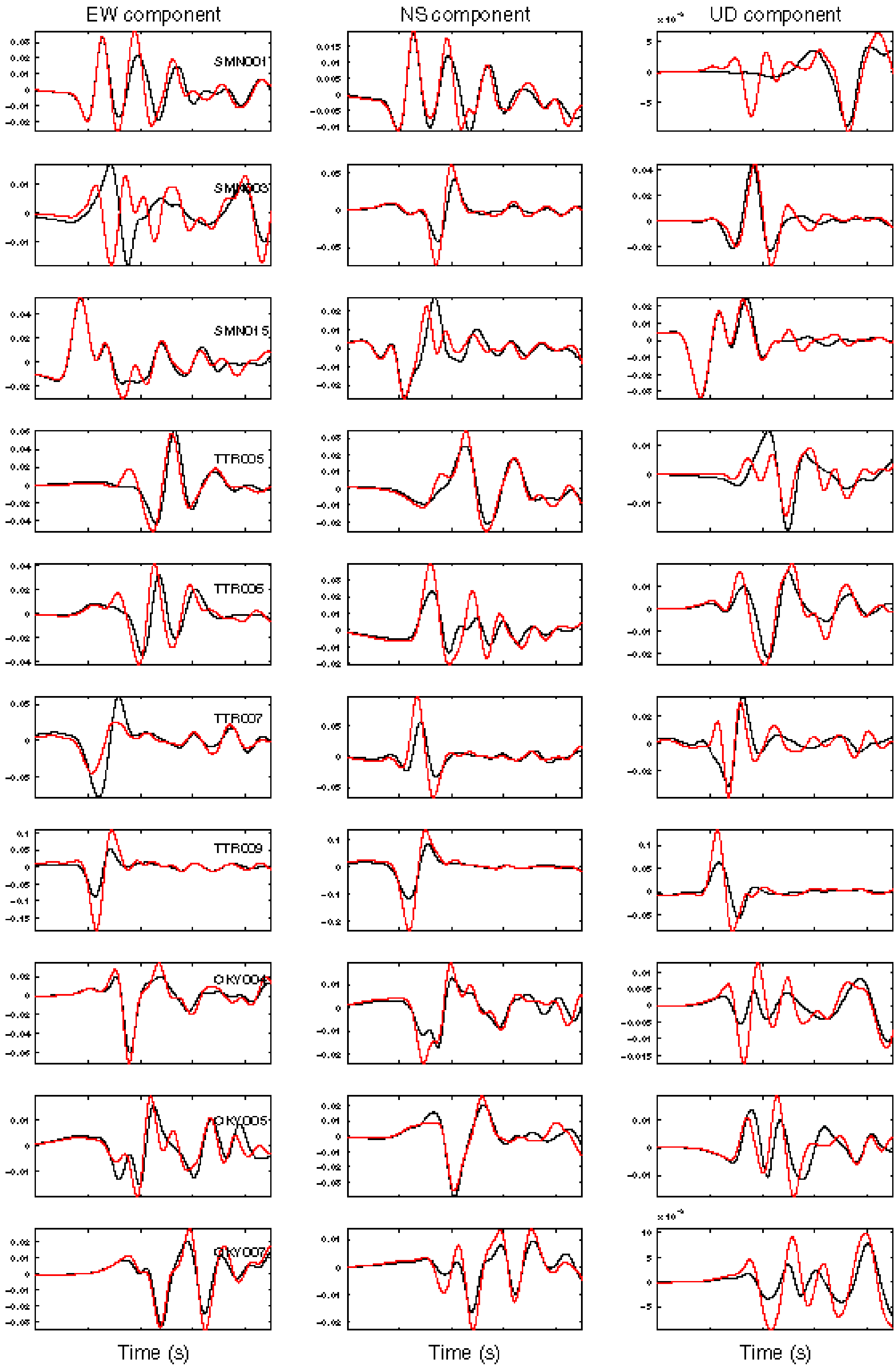

Figure 8.21 Comparison of the velocity ground motion simulation between the model in which tensile cracks are generated (red line) and the model free of tensile cracks (black line). The comparison is in the frequency range of 0.05Hz to 0.5Hz. The waveforms simulated correspond to the location of Knet stations.

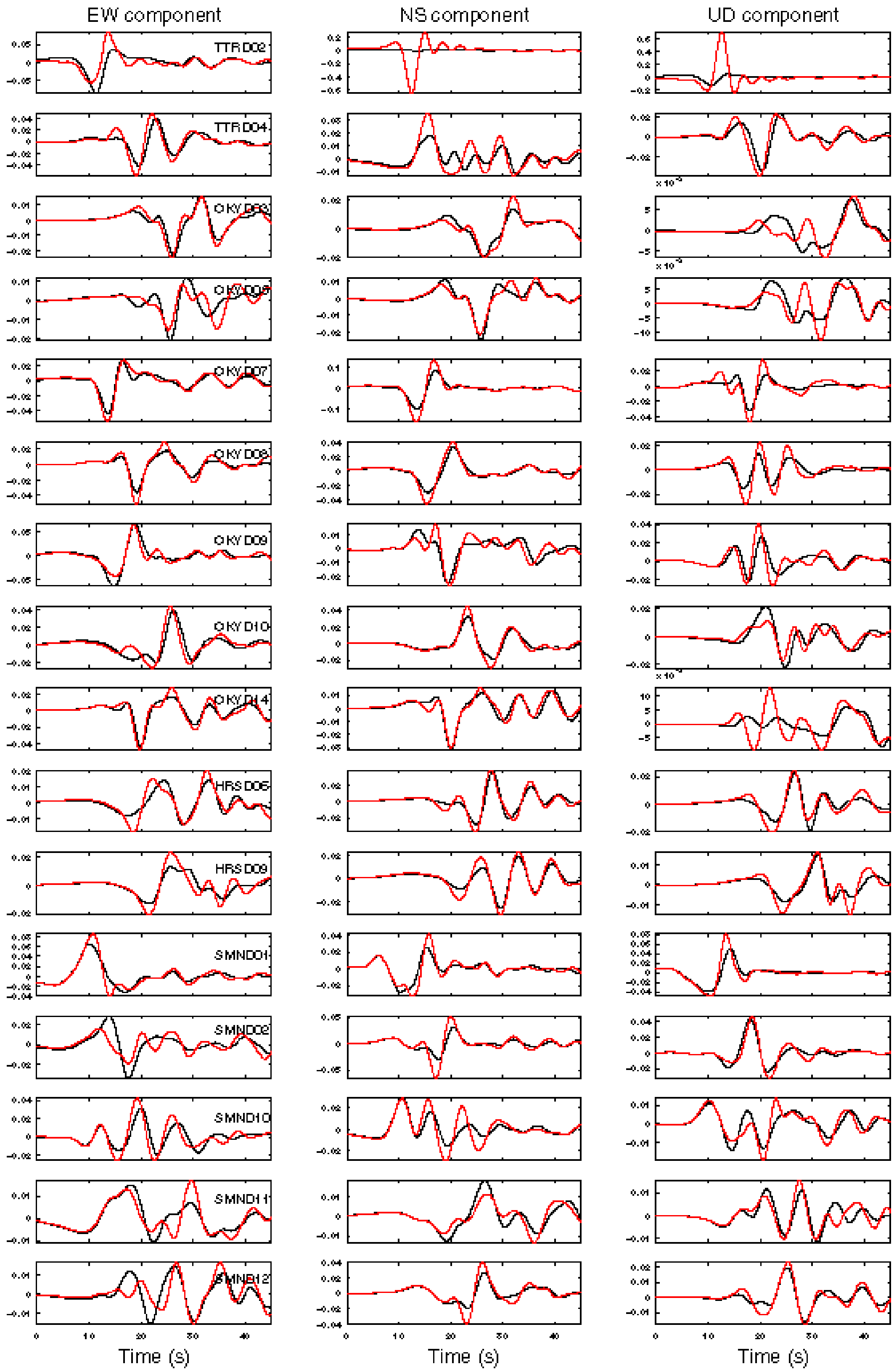

Figure 8.22 Comparison of the velocity ground motion simulation between the model in which tensile cracks are generated (red line) and the model free of tensile cracks (black line). The comparison is in the frequency range of 0.05Hz to 0.5Hz. The waveforms simulated correspond to the location of Kiknet stations.

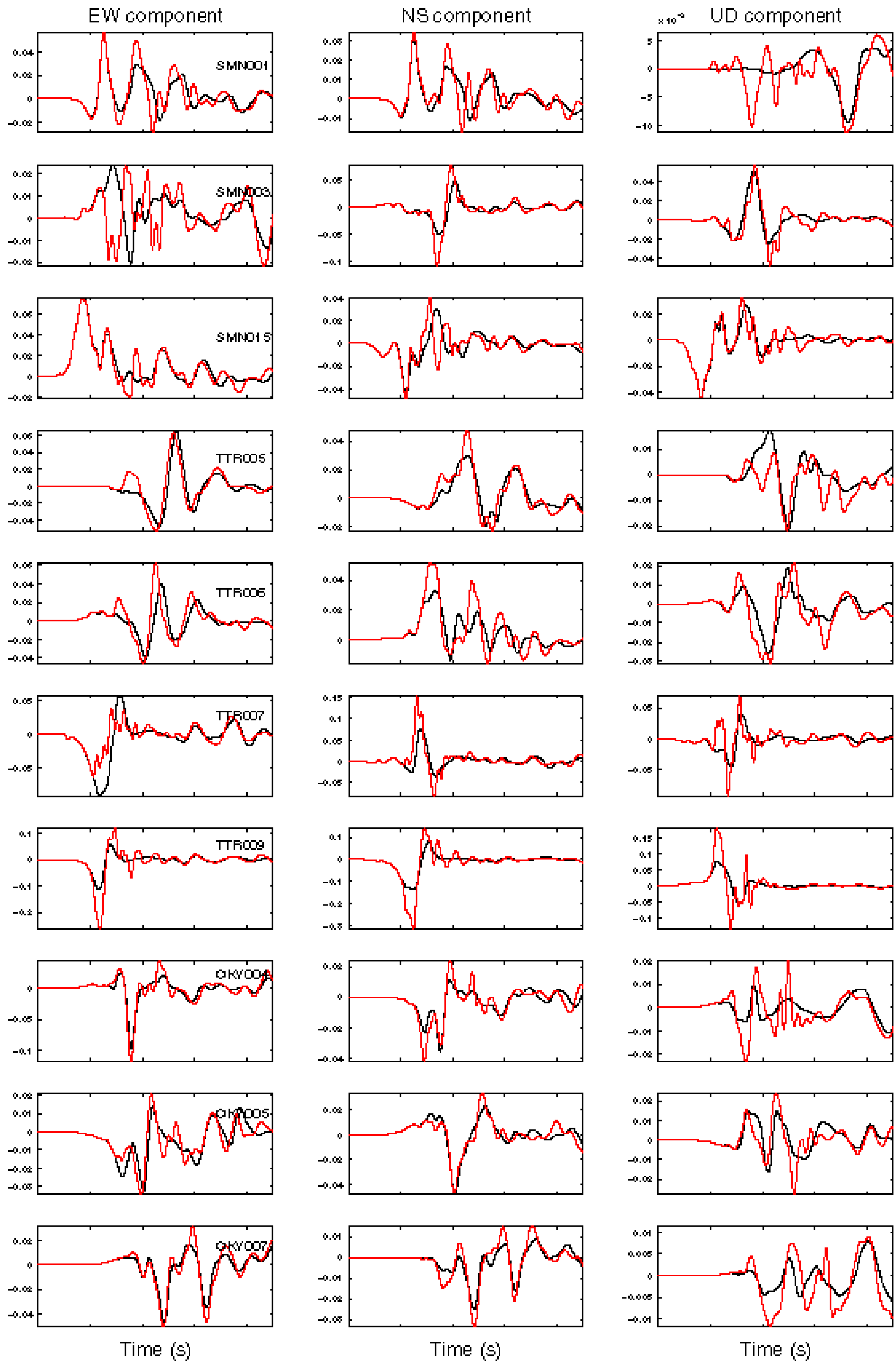

Figure 8.23 Comparison of the velocity ground motion simulation between the model in which tensile cracks are generated (red line) and the model free of tensile cracks (black line). The waveforms are not filtered. The waveforms simulated correspond to the location of Knet stations.

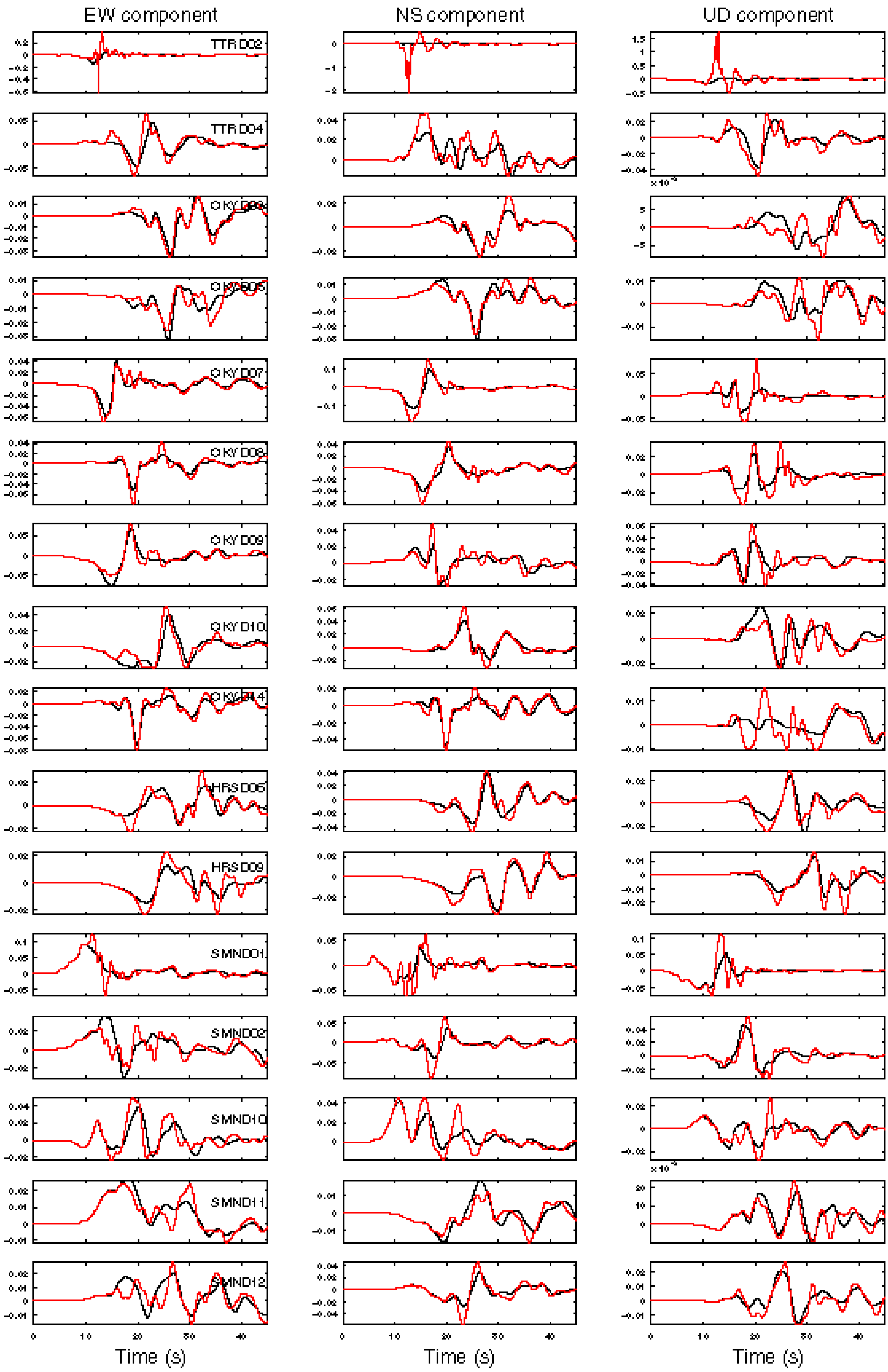

Figure 8.24 Comparison of the velocity ground motion simulation between the model in which tensile cracks are generated (red line) and the model free of tensile cracks (black line). The waveforms are not filtered. The waveforms simulated correspond to the location of Kiknet stations.

Chapter 9

Conclusion

The adequacy of the Discrete Element Method (DEM) to simulate a shear dynamic rupture process using 2D and 3D models has been firmly established. The problems analyzed to verify the adequacy of the DEM for the 2D and 3D model to simulate a dynamic rupture process were very well resolved by the DEM, the results are very consistent with the solutions presented in the specialized literature. On the other hand, the patterns of new tensile cracks originated during a dynamic shear rupture simulations is consistent with those observed in laboratory (e.g. Petit and Barquins, 1988) as well as in the field (e.g. Vermilye and Scholz, 1998), in which the tensile cracks often tend to develop kinking or wing cracks from the end of a shear sliding plane. In this context, the 2D and 3D DEM can be used very effectively to study the spontaneous shear rupture propagation in a fault model embedded in an elastic medium and the generation of new tensile cracks.

As far as the author know, the present paper contains the first numerical simulation in 3D of the generation of tensile cracks during the dynamic shear rupture process along a pre-existing fault in an earthquake. Earlier simulations in 2D have been presented by Yamashita (2000) using a dynamic model and Vermilye and Scholz (1998) and Reches and Lockner (1994) using a quasi-static analysis. Since the rupture process of an earthquake involves a fracture dynamics problem, the superposition of the three basic modes of rupture (Mode I, II and III) is required to describe the most general case of dynamic rupture propagation. The assumptions that the new cracks are generated only by tension (mode I) and that shear sliding (mode II and III) take place only along a pre-existing fault are very well accounted by the DEM.

9.1. Two Dimensional Model

For the application in 2D, the simulation of the spontaneous shear rupture propagation in a dipping fault that reaches the free-surface show that the estimation of the parameters strength excess and critical slip is important to the analysis of the near source ground motion. From the results we conclude that the rupture velocity strongly affects the near source ground motion, and the rupture velocity is highly dependent of the combination of the strength excess and critical slip. Furthermore, the results suggest that for some combination of these parameters the rupture propagates with a critical rupture velocity that can generate the strongest ground motion near the source, this critical rupture velocity seems to be around 95% of the S wave velocity. Therefore, the right combination of these two parameters is important to for example explain some characteristics of the fault rupture, ground motion and damage pattern caused by a real earthquake.

The simulation of tensile cracks during a spontaneous shear dynamic rupture in 2D shows that the tensile cracks expand with the shear rupture growth and propagate from the tip of the shear crack on the dilatational side of the fault. In addition, the expansion of the new cracks at the end of the pre-existing fault extends for larger distance forming complex branches of crack patterns, phenomenon observed for the first time in a numerical analysis.

9.2. Three Dimensional Model

For the application in 3D, it was show that the DEM could be also used for the estimation of the dynamic parameters, such as: the dynamic and static stress drop, strength excess and critical slip recovered from the kinematic source model. It was applied for the 2000 Tottori earthquake. The strength changes (stress drop and strength excess) calculated for this earthquake show important characteristics of the stress changes associated with the foreshocks and aftershocks distribution. It was found that most of the foreshocks and aftershocks are located in the zone of negative and zero stress drop, in the surrounding area of the main asperity. It suggests that the asperity was a barrier during the foreshocks, and after the main shock, the stress in the area surrounding the asperity increased and triggered most of the aftershocks. The interesting thing is that the seismic activity before the mainshock was confined to a finite zone localized in the central part of the fault. From the strength excess and stress drop distributions we found that this confined zone probably was bordered by barriers, these barriers being possibly responsible for arresting the rupture process of these previous events.

For the generation of tensile cracks during a spontaneous shear dynamic rupture in 3D, a theoretical vertical strike slip fault embedded at a depth of 3km from the free-surface was used. For a homogeneous model (with no asperity) the significant cracks extend from the borders of the fault forming a flower structure. For an asperity model the new tensile cracks are mainly generated from the borders of the asperity and from the border of the pre-existing fault. The variation of the asperity location with depth strongly affects the cracks generated from the top of the fault. As closer the asperity to the top of the fault as more the effects on the cracks. For the conditions set in the asperity model, the fault with an asperity located between 2.0km and 1.5km from the top of the fault is the minimum condition to the cracks reaches the free-surface. It was also found that the generation of tensile cracks strongly affects the rupture process of the fault and the near source ground motion. Compared to a model free of tensile cracks, the shear slip is almost duplicated and the rupture duration is extended for more time. And also the pattern of the ground motion suffers a drastic change, specially for the normal and vertical component.

Finally, our method using the DEM is applied to the 2000 Tottori earthquake. In order to simulate the generation of new cracks, the pre-existing fault defined by the kinematic source model of Iwata et-al (2000) was embedded at a depth of 2km from the free-surface. Since the rupture is not a pure strike slip and the dynamic parameters distributions are very heterogeneous, from the results it may be seen that the new cracks grew from the two side of the fault following different patterns and forming new fractures as a complex flower structure. The new cracks are generated mainly from the asperity zone (area of highest values of stress drop) and from the top of the fault. The faulting generated a surface rupture on only one side of the fault parallel to the trace of the main fault and 2.0km distance from the fault. The trace of this surface rupture corresponds to some of the several cracks found on the field observation developed by Fusejima et al. (2000). An also the simulation of the development of a flower structure is supported by the study of seismic reflection survey around the 2000 Tottori (Japan) earthquake area developed by Inoue et al. (2001) and Aben et al. (2001), in which from these studies the existence of a flower structure near the free-surface could be implied. Some of the new cracks is also associated with the aftershocks distribution, suggesting that some of the cracks opened during the shear rupture could be the zone of potential aftershocks. It is expected since we accept that the shear cracks develop as a plane of shear failure only after a long history of tensile cracks. Steps include the formation of individual tensile microcracks, propagation and linking of these cracks and finally larger scale shear failure or fault zone.

The effects of the generation of tensile cracks on the near source ground motion were also observed comparing with a model free of tensile cracks. The pattern of the ground motion suffers a drastic change in all the components. It was also observed that the model with cracks predicts ground motions with higher frequency content than the model free of cracks.

In order to validate the dynamic simulation of the Tottori earthquake studied here, the waveform simulated using the model with cracks and without cracks is compared with the ground motions recorded by the Kiknet and Knet. In general, the simulations fit well the observations in a frequency range of 0.05 to 0.5 Hz.

Finally we can conclude that the proposed technique for the numerical analysis of the full dynamic rupture process including the generation of tensile cracks during an earthquake leads to truly encouraging results. The model and the results presented in this thesis show that the DEM could be used successfully in predicting near source ground motion, fracture behaviour during an earthquake and the formation of new fault zones.

Appendix

A.1 Determination of the Equivalent Stiffness of the Normal and Diagonal Bars of the DEM

The determination of the equivalent axial stiffness of the elements in a cubic lattice array, as shown in Figure 2.1 (Equation.2.1 and 2.2), in terms of the elastic properties of an equivalent isotropic continuum is reviewed here. This equivalence was shown by Nayfeh and Hefzy (1978) and first employed in dynamic problems by Riera (1982)

The stress-strain equations for a general elastic body may be written in the compact form

$$\sigma_i = C_{ij}\varepsilon_j \qquad (i, j = 1...6) \tag{A1}$$

where σ_{ij} and ε_j are the independent six components of the stress and strain tensors, respectively, and C_{ij}, is the matrix of elastic constants, containing 21 independent constants on account of symmetry considerations.

For an isotropic material, the matrix C_{ij} could be a function of only two independent constants, so C_{ij} can be written as:

$$C_{ij} = \begin{bmatrix} C_{11} & C_{12} & C_{12} & 0 & 0 & 0 \\ C_{12} & C_{11} & C_{12} & 0 & 0 & 0 \\ C_{12} & C_{12} & C_{11} & 0 & 0 & 0 \\ 0 & 0 & 0 & C_{44} & 0 & 0 \\ 0 & 0 & 0 & 0 & C_{44} & 0 \\ 0 & 0 & 0 & 0 & 0 & C_{44} \end{bmatrix} \tag{A2}$$

in which C_{11}, C_{12} and C_{44} are functions of Young's modulus E and the Poisson's ratio ν.

Since the DEM implies a lattice-type structure consisting of one dimensional axial elements, the contribution of each member to the overall stiffness must be duly accounted for the sum of the average contribution of each element will lead to the final stiffness matrix. It is assumed that the elements are perfectly straight and present constant cross-sectional area.

The elastic constant C_{ij} can be transformed from one orthogonal cartesian coordinates system x_i to another $\bar{x}_i$ (i=1,2,3) through an expression:

$$\overline{Q}_{ij} = f(Q_{i,j}, \alpha_{kl}) \qquad \begin{cases} (k, l = 1..3a) \\ (i, j = 1..6) \end{cases} \tag{A3}$$

where α_n denotes the direction cosines of the transformation. Q_{ij} and $\overline{Q}_{ij}$ are the elastic constant of systems x and $\bar{x}$, respectively. The derivation of equation (A3) is presented in details in Nayfeh and Hefzy (1978).

Equation (A3) is used in order to get the coefficients of equation (A2) for the corresponding cubic model of Figure 2.1a. Since all elements have the single unidirectional property E, each set of parallel bars will define a continuum with a single effective unidirectional property, which we shall refer to as Q_{11}. In the context of effective modulus theories, Q_{11} will be an area-averaged modulus. Thus, the value of Q_{11} will depend not only upon the specific model under consideration but also upon the spacing of the bars.

In particular, the cubic array shown in Figure 2.1a has two different properties of Q_{11}, one corresponds to the elements normal to the face of the cube (Q_{11}^n), and the other corresponds to the diagonal elements (Q_{11}^d).

The unidirectional effective properties Q_{11}^n and Q_{11}^d can be determined by referring to the projected area normal to each element in order to obtain the effective area. For the normal elements we can obtain an effective area equal to $L^2/2$ while for the diagonal elements it results $L^2/\sqrt{3}$. Thus, the unidirectional property for each element is given by:

$$Q_{11}^n = \frac{2EA_n}{L^2} \tag{A4}$$

$$Q_{11}^{d} = \frac{\sqrt{3}EA_d}{L^2} \tag{A5}$$

in which L is the side length of the basic cube and EA_n and EA_d are Young's modulus E times the cross-sectional area A for the normal and diagonal elements, respectively.

From equations (A4) and (A5), $\overline{Q}_{ij}$ of equation (A3), that is, the stiffness matrix of a continuum equivalent to the cubic lattice model may be obtained. As shown in Figure 2.1a, seven elements converge to each node of the cubic model (3 normal and 4 diagonals bars), hence matrix $\overline{Q}_{ij}$ can be expressed as follows:

$$\overline{Q}_{ij} = \sum_{I=1}^{3} f(Q_{11}^{n}, \alpha_{Ikl}^{n}) + \sum_{J=1}^{4} f(Q_{11}^{d}, \alpha_{Jkl}^{d}) \quad (k, l = 1...3) \tag{A6}$$

in which α_{Ikl}^{n} and α_{Jkl}^{d} are the direction cosines of the systems $\bar{x}$, x_I^n and $\bar{x}$, x_J^d respectively.

Combining equations (A4), (A5) and (A6), the elastic constants of equation (A2) can be obtained:

$$\begin{aligned} C_{11} &= Q_{11}^{n}(1 + \frac{4}{9}\delta) \\ C_{12} &= Q_{11}^{n}(\frac{4}{9}\delta) \\ C_{44} &= Q_{11}^{n}(\frac{4}{9}\delta) \end{aligned} \tag{A7}$$

where

$$\delta = \frac{Q_{11}^{d}}{Q_{11}^{n}} = \frac{\sqrt{3}A_d}{2A_n} \tag{A8}$$

Therefore, the matrix C_{ij} of equation. (A2) is:

$$C_{ij} = \frac{2EA_n}{L^2}\begin{bmatrix} 1+\frac{4\delta}{9} & \frac{4\delta}{9} & \frac{4\delta}{9} & 0 & 0 & 0 \\ \frac{4\delta}{9} & 1+\frac{4\delta}{9} & \frac{4\delta}{9} & 0 & 0 & 0 \\ \frac{4\delta}{9} & \frac{4\delta}{9} & 1+\frac{4\delta}{9} & 0 & 0 & 0 \\ 0 & 0 & 0 & \frac{4\delta}{9} & 0 & 0 \\ 0 & 0 & 0 & 0 & \frac{4\delta}{9} & 0 \\ 0 & 0 & 0 & 0 & 0 & \frac{4\delta}{9} \end{bmatrix} \tag{A9}$$

The engineering elastic constants, Young's modulus E, Poisson's ratio ν and shear modulus μ may be expressed in terms of the constants C_{ij} using the general stress-strain relations for anisotropic materials (Nayfeh and Hefzy, 1978), as follows:

$$E = C_{11} - \frac{2C_{12}^2}{C_{11} + C_{12}} \tag{A10a}$$

$$\nu = \frac{C_{12}}{C_{11} + C_{12}} \tag{A10b}$$

$$\mu = \frac{1}{2}C_{44} \tag{A10c}$$

Substituting in equation (A9), we obtain:

$$E = \frac{2EA_n(9 + 12\delta)}{L^2(9 + 8\delta)} \tag{A11a}$$

$$\nu = \frac{4\delta}{9 + 8\delta} \tag{A11b}$$

$$\mu = \frac{EA_n 4\delta}{9L^2} \tag{A11c}$$

To get the equivalent values of EA_n and EA_d as functions of the elastic properties of the material (which could be, for instance, E and ν), we use equation (A11) and the relation given in equation (A8), as follows:

$$\delta = \frac{9\nu}{(4 - 8\nu)} \tag{A12a}$$

$$EA_n = \frac{L^2(9 + 8\delta)}{2(9 + 12\delta)} E \tag{A12b}$$

$$EA_d = \frac{\delta L^2(9 + 8\delta)}{\sqrt{3}(9 + 12\delta)} E \tag{A12c}$$

Finally, the equivalent stiffness of the normal and diagonal elements is obtained dividing equations (A12a,b) by the length of the respective element, being L_n=L (for normal elements) and $L_d = \frac{\sqrt{3}}{2} L$ (for diagonal elements):

$$\frac{EA_n}{L_n} = \frac{L(9 + 8\delta)}{2(9 + 12\delta)} E \tag{A13a}$$

$$\frac{EA_d}{L_d} = \frac{2\delta L(9 + 8\delta)}{3(9 + 12\delta)} E \tag{A13b}$$

The nodal masses, m_i, are calculated in terms of the volumes of influence of each node i, for the internal nodes it results:

$$m_i = \frac{\rho L^3}{2} \tag{A14}$$

while for surface nodes, linear corner and point corner nodes, the mass given by equation (A14) must be divided by 2, 4 and 8 respectively.

Reference

-Abe, S., Miyakoshi K. and Inoue D. (2001), Seismic Reflection Survey around the 2000 Tottori-Ken earthquake area, *2001 Japan Earth and Planetary Science Joint Meeting*. S3-P013, June 4-8, 2001, Tokyo, Japan.

-Aki, K. (1984), Asperities, barriers, characteristics earthquakes and strong motion prediction, *J. Geophys. Res*., 89, 5867-5872.

-Anders, M. H., and D. V. Wiltschko (1994), Microfracturing, paleostress and the growth of faults, *J. Struct. Geol.*, 16, 795-815.

-Andrews, D.J (1976). Rupture velocity of plane-strain shear cracks, *J. Geophys. Res.*, **81**, 5679-5687.

-Atkinson, B. K. (1987), Fracture Mechanics of Rock, *Academic Press INC*., London.

-Brune J.N (1970). Tectonic stress and the spectra of seismic shear waves from earthquakes. *J. Geophys. Res*. vol 75, pp. 4997-5009.

-Brune, J.N. (1996). Particle Motion in a Physical Model of Shallow angle Thrust Faulting. *Proc. Indian. Cad. Sci.*, 105, 197-206.

-Bouchon, M. (1997), The state of stress on some faults of the San Andreas system as inferred from near-field strong motion data, *J. Geophys. Res.*, 102, 11731-11744.

-Cochard A. and Madariaga R. (1994). Dynamic Faulting Under Rate-Dependent Friction, *Pageoph* vol 142, pp. 419-445.

-Coutant, O., J. Virieux, and A. Zollo (1995). Numerical source implementation in a 2D finite difference scheme for wave propagation. *Bull. Seism. Soc. Am.* Vol. 85, 1507-1512.

-Cox, S. J. D., and C. H. Scholz (1988), Rupture initiation in shear fracture of rocks: An experimental study, *J. Geophys. Res.*, 93, 3307-3320.

-Dalguer, L.A. (2000). Simulação de Movimentos Sísmicos Considerando o Mecanismo de Ruptura da Falha Causativa do Terremoto. *Doctoral dissertation*, Department of Civil Engineering, Federal University of Rio Grande do Sul, Porto Alegre R.S., Brazil. (In portuguese).

-Dalguer, L.A.; Riera, J.D. and Irikura, K. (1999). Simulation of seismic excitation using a stick-slip source mechanism. *Transaction, 15th International Conference on Structural Mechanics in Reactor Technology (SMiRT15)*, Seoul, Korea, August 1999, Vol 5.

-Dalguer L.A; Irikura K; Riera J. And Chiu H.C (2001a). Fault Dynamic Rupture Simulation of the Hypocenter area of theThrust Fault of the 1999 Chi-Chi (Taiwan) Earthquake. *Geophysical Research Letters*, April 1,vol. 28, no. 7, pages 1327-1330..

-Dalguer L.A; Irikura K; Riera J. And Chiu H.C (2001b). The Importance of the Dynamic Source Effects on Strong Ground Motion During the 1999 Chi-Chi, Taiwan, Earthquake: Brief Interpretation of the Damage Distribution on Buildings. *Bull. Seism. Soc. Am.* Vol. 91, 1112-1127.

- Dalguer, L.A; K. Irikura, W. Zangh and J. Riera (2001c), Distribution Dynamic Stress Changes during 2000 Tottori (Japan) Earthquake: Brief Interpretation of the Earthquake Sequences Foreshocks, Mainshock and Aftershocks. *In submission to Geophys. Res. Letters*.

-Das S. and Aki K. (1977). A numerical study of a two-dimensional spontaneous rupture propagation. Geophys. *J. Roy. Astron. Soc*. vol. 50, pp. 643-668.

-Day S.M. (1982a). Three-Dimensional Finite Difference Simulation of Fault Dynamics: Rectangular Fault with Fixed Rupture Velocity. *Bull. Seism. Soc. Am*. Vol. 72, 705-727.

-Day S.M. (1982b). Three-Dimensional Simulation of spontaneous rupture: the effect of nonuniform prestress. *Bull. Seism. Soc. Am*. Vol. 72, 1881-1902.

-Day, S. M., G. Yu, and D. J. Wald (1998), Dynamic stress change during earthquake rupture*, Bull. Seismol. Soc. Am*., 88, 512-522.

-Dieterich, J.H. (1979). Modeling of Rock Friction 1. Experimental Results and Constitutive Equation, *J. Geophys. Res*. 84, 2161-2168.

-Dodge, D. A. and G. C. Beroza (1996), Detailed observations of California foreshock sequences: Implications for the earthquake initiation process, *J. Geophys. Res*., 101, 22371-22392.

-Doz G.N and Riera, J.D. (1995) Towards the Numerical Simulation of seismic Excitation *Transaction, 13th International Conference on Structural Mechanics in Reactor Technology (SMiRT13),* Porto Alegre, Brazil, August 1995, Vol 3

-Ellsworth, W. L., and G. C. Beroza (1998), Observation of the seismic nucleation phase in the Ridgecrest, California, earthquake sequence, *Geophys. Res. Letters*, 25, 401-404.

-Frankel, A. (1993). Three-dimensional simulations of ground motion in the San Bernardino Valley, California, for hypothetical earthquakes on the San Andreas fault*. Bull. Seism. Soc. Am.* Vol. 83, 1020-1041.

-Frankel, A. and J. Vidale (1992). A three-dimensional simulation of seismic waves in the Santa Clara Valley, California, from a Loma Prieta aftershock. *Bull. Seism. Soc. Am*. Vol. 82, 2045-2074.

-Fukuyama E. and Madariaga R. (1998). Rupture dynamic of a planar fault in a 3D elastic medium: rate- and slip-weakening friction*. Bull. Seism. Soc. Am*. Vol. 88, pp. 1-17.

-Fusejima, Y., T. Yoshioka, K. Mizuno, M. Shishikura, R. Imura, T. Komatsubara and T. Sasaki, (2001), Surface rupture associated with the 2000 Tottori-ken Seibu earthquake, *Annual Report on Active Fault and Paleoearthquake Researches, No.1,* Geological Survey of Japan, National Institute of Advanced Industrial Science and Technology.

-Graves, R.W. (1996). Simulating seismic wave propagation in 3D elastic media using staggered-grid finite differences, *Bull. Seism. Soc. Am*,Vol. 86, No. 4, 1091-1106.

-Graves, R.W. (1998). Three-dimensional finite-difference modeling of the San Andreas fault: source parameterization and ground motion levels*, Bull. Seism. Soc. Am*, Vol. 88, 891-897.

-Griffith, A. A. (1920), The phenomena of rupture and flow in solids, *Phil. Trans. Roy. So*c., Ser. A, 221, 163-198.

-Harris, R. A. (1998), Introduction to special section: Stress triggers, stress shadows, and implications for seismic hazard*, J. Geophys. Res*., 103, 24347-24358.

-Harris, R. A., and S. M. Day (1999). Dynamic 3D simulations of earthquakes on en echelon faults, *Geophys. Res. Letters*, 26, 2089-2092.

-Hayashi Y. (1982). Sobre um Modelo de Discretização de Estruturas Tridimensionais Aplicado em Dinámica não Linear. *Tese M. Sc., CCPGEC*, Universidade Federal do rio Grande do Sul, Porto Alegre, Dezembro 1982.(In portuguese).

-Ida, Y. (1972). Cohesive force across the tip of a longitudinal-shear crack and Griffith's specific surface energy*, J. Geophys. Res*., 77, 3796-3805.

-Inoue, T. and Miyatake, T. (1998). 3D simulation of near-field strong ground motion based on dynamic modeling, *Bull. Seism. Soc. Am*, Vol. 88, No. 6, 1445-1456.

-Inoue D., K. Miyakoshi, K. Ueta and S. Abe (2001). Geological survey of active faults around the 2000 Tottori-Seibu earthquake, *Genshiryoku-eye (Nuclear Viewpoints).* Vol. 47 Nro 11, 66-71 (In japanese)

-Iwata, T., H. Sekiguchi, Y. Matsumoto, H. Miyake, and K. Irikura (2000), Source Precess of the 2000 Western Tottori Prefecture earthquake and near-source strong ground motion, 2000, *Fall meeting of the Seismological Society of Japan*.

-Joint Group for Dense Aftershock Observation of the 2000 Tottori-ken Seibu Earthquake (2001), Aftershock distribution and focal mechanisms of the 2000 Tottori-ken Seibu Earthquake obtained by dense aftershock observation, *submitted to Newsletter, Seismol. Soc. Jpn*. (in Japanese).

-Jones, L. M. (1984), Foreshocks (1966-1980) in the San Andreas System, California, *Bull. Seismol. Soc. Am*., 74, 1361-1380.

-Jones, L. M., B. Wang, S. Xu, and T. J. Fitch (1982), The foreshock sequence of the February 4, 1975, Haicheng earthquake (M = 7.3), *J. Geophys. Res*., 87, 4575-4585.

-Kanamori, H., and G. S. (1978), Stewart, Seismological aspects of the Guatemala earthquake of February 4, 1976, *J. Geophys. Res*., 83, 3427-3434.

-Kostrov, B.V. (1966). Unsteady propagation of longitudinal shear cracks, *Journal of applied Mathematics and Mechanics*, vol. 30, pp. 1241-1248.

-Lay T. and T.C. Wallace (1995), Modern Global Seismology, *Academic Press*, San Diego, California.

-Lajtai, E. Z., (1971), A theoretical and experimental evaluation of the Griffith theory of brittle fracture, *Tectonophys,* 11, 129-156.

-Madariaga R. (1976). Dynamics of an expanding circular fault. *Bull. Seism. Soc. Am*. Vol. 66, pp. 639-666.

-Madariaga R., Olsen K., and Archuleta R. (1998). Modeling Dynamic Rupture in a 3D Earthquake Fault Model, *Bull. Seism. Soc. Am*. Vol. 88, 1182-1197.

-Mikumo T. and Miyatake T. (1978). Dynamical Rupture Process on a Three-Dimensional Fault with Non-Uniform Frictions and Near-Field Seismic Waves, *Geophysical Journal of the Royal Astronomical Society*, vol. 54, pp. 417-438.

-Mikumo, T. and T. Miyatake (1993). Dynamic rupture processes on dipping fault, and estimates of stress drop and strength excess from the results of waveform inversion, *Geophys. J. Int*., **112**, 481-496.

-Mikumo, T., and T. Miyatake (1995), Heterogeneous distribution of dynamic Stress drop and relative fault strength recovered from the results of waveform inversion: the 1984 Morgan Hill, California, earthquake, *Bull. Seismol. Soc. Am*., 85, 178-193.

-Mikumo, T., S. K. Singh, and M. A. Santoyo (1999), A possible stress interaction between large thrust and normal faulting earthquakes in the Mexican subduction zone, *Bull. Seismol. Soc. Am*., 89, 1418-1427.

-Miyatake, T. (1992), Dynamic rupture process of Inland earthquakes in Japan weak and strong asperity, *Geophys. Res. Letters,* 19, 1041-1044.

-Moore, D. E., and D. A. Lockner (1995), The role of microfracturing in shear-fracture propagation in granite*, J. Struct. Geol*., 17, 95-114.

-Mora P. and Place D. (1994) Simulation of the Frictional stick-Slip Instability *PAGEOPH*, vol. 143, pp. 61-87.

-Morgan J.K. (1999). Numerical simulation of granular shear zones using the distinct element method 2. Effects of particle size distribution and interparticle friction on mechanical mehavior. *J. Geophys. Res*. Vol. 104, pp.2721-2732.

-Morgan J.K. and Boettcher M.S. (1999). Numerical simulation of granular shear zones using the distinct element method 1. Shear zone kinematics and the micromechanics of localization. *J. Geophys. Res*. Vol. 104, pp.2703-2719.

-Nayfeh, A.H. and Hefsy, M.S (1978). Continuum Modeling of Three-Dimensional truss-like Space Structures. *AIAA Journal*, vol. 16(8), pp. 779-787.

-Nielsen S.B. (1998). Free surface effects on the propagation of dynamic rupture, Geophys. Res. Lett., **25**, 125-128.

-Oglesby, D.D., R.J. Archuleta and S.B. Nielsen (1998). Earthquakes on Dipping Faults: The Effects of Broken Symmetry, *Science*, 280, 1055-1059.

-Oglesby, D.D., R.J. Archuleta and S.B. Nielsen (2000). The three-dimensional dynamics of dipping faults, *Bull. Seism. Soc. Am*. **90**, 616-628.

-Ohmi, S. and K. Obara (2001), Deep low frequency earthquakes preceded the 2000 Tottori-ken Seibu earthquake, Abs., 2001 *Jpn. Earth. Sci. Joint Meeting*, S3-004. (In japanese with English abstract)

-Ohnaka, M., Y. Kuwahara and K. Yamamoto (1987). Constitutive Relations between Dynamic Physical Parameters Near a Tip of the Propagating Slip Zone During Stick-Slip Shear Failure, *Tectonophysics*, 144, 109-125.

-Olsen, K.B., R.J. Archuleta, and J.R. Matarese (1995). Magnitude 7.75 earthquake on the San Andreas fault: three-dimensional ground motion in los Angeles. *Science*, vol. 270, 1628-1632.

-Olsen, K. B., Madariaga R., and Archuleta R. (1997). Three Dimensional Dynamic Simulation of the 1992 Landers Earthquake. *Science.* vol. 278, pp. 834-838.

-Petit, J. P., and M. Barquins (1988) Can natural faults propagate under mode II conditions?, *Tectonics,* 7, 1243-1256

-Pitarka A. (1999). 3D Elastic Finite-Difference Modeling of Seismic Motion Using Staggered Grid with Nonuniform Spacing. *Bull. Seism. Soc. Am.* Vol. 89, pp. 54-68.

-Pitarka, A. and K. Irikura (1996). Modeling 3-D surface topography by finite-difference method: the Kobe JMA station site case study. *Geophys. Res. Lett*., vol. 23, 2723-2732.

-Pitarka, A., K. Irikura, T. Iwata, and H. Sekiguchi (1998). Three-dimensional simulation of the near-fault ground motion for the 1995 Hyogo-ken Nanbu (Kobe), Japan, earthquake. *Bull. Seism. Soc. Am.* Vol. 88, 428-440.

-Quin, H. (1990), Dynamic stress drop and rupture dynamic of the October 15, 1979 Imperial Valley, California, earthquake, *Tectonophysics,* 175, 93-117.

-Reches, Z. and D. A. Lockner (1994), Nucleation and growth of faults in brittle rocks, *J. Geophys. Res*., 99, 18159-18173.

- Riera, J.D. (1982) Basic Concepts and Load Characteristics in Impact Problems, in Concrete Structures under Impact and Impulsive Loading", Introductory Report, *RILEM, CEB, IABSE, IASS -Interassociation Symposium*, Berlin, June 1982, 7-29.

-Riera, J.D. and M. Rocha (1991). A Note on the Velocity of Crack Propagation in Tensile Fracture, *Revista Brasileira de Ciencias Mecanicas*, RBCM, XII, N3, 217-240.

-Rimal M.H. (1992) Dynamic Fracture Analyses by the Extended Distinct Element Method. *Doctoral Dissertation*. Department of Civil Engineering, Univeristy of Tokyo, Japan.

-Ruina, A. (1983). Slip Instability and State Variable Friction Laws, *J. Geophys. Res*., 88, 10359-10370.

-Shi, B.; Anooshehpoor, A.; Brune J.N and Zeng, Y. (1998). Dynamics Thrust Faulting: 2D Lattice Model. *BSSA,* vol.88, pp. 1484-1494.

-Shibutani, T., S. Nakao, R. Nishida, F. Takeuchi, K. Watanabe and Y. Umeda (2001), Swarm-like seismic activity in 1989, 1990 and 1997 preceding the 2000 Tottori-ken Seibu Earthquake, *submitted to Earth Planets Space*.

-Scholz, C. H. (1968), Mechanism of creep in brittle rock, *J. Geophys. Res.*, 73, 3295-3302.

-Scholz, C. H. (1990). The Mechanics of Earthquakes and Faulting, *Cambridge Univ. Press*, New York.

-Vermilye, J. M., and C. H. Scholz (1998), The process zone: A microstructural view of fault growth, *J. Geophys. Res*., 103, 12223-12237.

-Virieux J. and Madariaga R. (1982). Dynamic Faulting Studied by a finite Difference Method. *Bull. Seism. Soc. Am*. Vol. 72, 345-369.

-Wolf, J.P. (1988). Soil-Structure Interaction Analysis in Time Domain. *Prentice Hall*, Englewood Cliffs, New Jersey.

-Yamashita, T. (2000), Generation of microcracks by dynamic shear rupture and its effects on rupture growth and elastic wave radiation, *Geophys. J. Int*., 143, 395-406

-Yomogida, K. and J.T. Etgen (1993). 3-D wave propagation in the Los Angeles Basin for the Whittier-Narrows earthquake. *Bull. Seism. Soc. Am*. Vol. 83, 1325-1344

-Zhang W., T. Iwata, K. Irikura and M. Bouchon (2001), The characteristics of the dynamic source parameters of the 2000 Tottori-Ken Seibu earthquake, *The Sismological Society of Japan 2001, FALL MEETING,* P130 (abstract), Kagoshima, Japan, October 24-26, 2001.